RVC-2101

Long-Range Precision Aerial Delivery System

This report represents the work of

one or more WPI undergraduate students

submitted to the faculty as evidence of completion of a

degree requirement.

WPI routinely publishes these reports on the web without

editorial or peer review

by

Christopher Ferrari

Christopher Ferrari

Kiernan Joyce

Kiernan Joyce

Mackenzie Warren

Mackenzie Warren

Rebecca Debski

Rebecca Debski

Scott D'Attilio

Scott D'Attilio

Terrance Cooper

Terrance Cooper

Thierry de Crispigny

Thierry de Crespigny

William Schwend

William Schwend

Approved by:

_____

Raghvendra V. Cowlagi, Advisor

Associate Professor, Aerospace Engineering Department, WPI.

Abstract

The goal of this project is to design and analyze autonomous aerial delivery vehicle concepts with terrestrial launch and/or aerial deployment capabilities as well as increased range and accuracy compared to the state of the art. Since World War II, the United States Army has used aerial delivery methods to transport necessary supplies such as medical kits, food, fuel, and ammunition to soldiers in remote battlefronts. Current precision aerial delivery systems (PADS) are dominated by thrustless parafoils deployed from a manned transport aircraft. However, the horizontal range of these PADS are limited, due to which the manned transport aircraft is required to fly close to the delivery destination. This situation is undesirable due to the risks posed to the transport aircraft pilots. The outcomes of this project will enable the development of a long-range PADS that can avoid putting the transport aircraft pilots at risk. The design requirements considered in this project are of a PADS that can launch from the ground, carry 100-200 kg of cargo to destinations 200-500 km away, and then return to either the launch location or a secondary location at a comparable distance. The final location of the supply drop must be less than 100m from the desired location. After launch, the system must be capable of autonomous guidance to the destination.

In this project report, the state-of-the-art is first reviewed. Next, to narrow down potential design options, a design space exploration is conducted using both low and medium fidelity computational models and simulations developed using MATLAB and XFLR5. Based on the outcomes of this initial analysis, three designs are selected for further research and development: a fixed-wing aircraft, a hang-glider, and a parawing. Through several sizing iterations and calculations, computer-aided design (CAD) assemblies are created using SOLIDWORKS for all three designs. The CAD models include ribbing in both the wing and fuselage as well as mounting points, vertical and horizontal stabilizers, and control surfaces. This allows for building a 1-10 scale model of the hang-glider, and high-fidelity simulation and analysis of the parawing and fixed-wing designs.

Computational fluid dynamics simulations are developed using Fluent to analyze the aerodynamic properties of the parawing and fixed-wing designs. The purpose of these simulations is to determine the stability and control derivatives as well as lift and drag coefficients at different angles of attack. Ansys simulations are developed to measure stress and displacement of the wing and wing mounting under the conditions of lift, drag, thrust, and gravity, and to analyze the structural integrity of the same two designs. Additional analysis involves measuring stresses on the aircraft bodies for various trim states and legs of flight via a symmetrical half plane model. To simulate the flight of the fixed-wing and parawing designs, trajectories are generated for different phases of flight (i.e., climb, cruise, etc). These trajectories are used to find trim conditions that lead to linearized flight dynamical models. Linear quadratic regulator (LQR) autopilot controllers are designed to control airspeed, altitude, climb angle, and heading angle, thereby

enabling trajectory tracking. The closed-loop responses of the aircraft under autopilot control are tested using MATLAB and Simulink. Finally, the hang-glider CAD model is physically assembled using a foam-carbon composite in an effort to minimize both mass and cost. This is a 1-10 scale model that preserves payload weight fractions and total lifting force of the aircraft. The hang-glider is controlled via onboard electronics and radio control. Small scale testing will be completed to analyze performance characteristics for various phases of flight. With the completion of the previously outlined simulation, small scale testing and analysis, this project will demonstrate and rank three separate concepts for long-range autonomous aerial delivery.

This study indicates that a parawing design is the better choice for scenarios where the goal is to minimize monetary cost and a fixed wing design is the better choice when the goal is to minimize time. Parawings weigh less and are easier to manufacture, and as a result they consume less fuel than a fixed wing but take a significantly longer time to reach their destination during flight. A fixed wing aircraft is faster, but weighs more, thus using more fuel. Additionally, fixed-wing aircraft are also more costly to manufacture.

Fair use disclaimer:

This document may contain copyrighted material, such as photographs and diagrams, the use of which may not always have been specifically authorized by the copyright owner. The use of copyrighted material in this document is in accordance with the "fair use doctrine", as incorporated in Title 17 USC §107 of the United States Copyright Act of 1976. This document is distributed without profit for educational purposes to those who have expressed interest in receiving the included information.

Acknowledgements

First, we would like to give a special thank you to Professor Raghvendra V. Cowlagi and Dr. Gregory Noetscher for their support and guidance. We also want to thank Worcester Polytechnic Institute and US Army Combat Capabilities Development Command Soldier Center (DEVCOM SC) for their sponsorship. Finally, WRS and MEW would like to thank Dr. Keith Bergeron of the US Army Core of Engineers and Dr. Mehdi Ghoreyshi of the US Air Force Academy for supplying the parawing geometry.

Table of Contents

Table of Figures

Table of Tables

Table of Authorship

Section	Project Work	Report Writing
1. Project Overview	All	WRS
1.1. Project Objectives	All	WRS
1.2.1. Historical Development of Airdrop Systems	RCD, WRS	WRS
1.2.2. Joint Precision Airdrop Systems (JPADS)	WRS	WRS
1.2.3. Unpowered RAM Parafoils	KCJ, RCD	RCD
1.2.4. Other Potential Systems	All	CDF, SCD, WRS
1.2.5. Power Systems for UAVs	MEW, RCD	CDF, MEW, RCD, TLC
1.2.6. Control of Powered Parafoils/ Paragliders	TLC, WRS	TLC
1.3. Design Requirements Constraints, and Other Considerations	All	WRS
1.4. Project Management	All	SCD, WRS
1.4.1 Tasks and Timetable	All	MEW
1.5 Relevant Engineering Standards	All	WRS
1.6 Methods	All	All
1.7 Broader Impacts	All	SCD
2 System design	CDF, MEW, SCD, TLC, TLD	TLD
2.1 Fixed-Wing Aircraft Design	CDF, MEW, SCD, TLC, TLD, WRS	TLD, WRS
2.1.1 Fixed Wing Geometry	MEW, WRS	WRS
2.1.2 Fixed-Wing Structural Design	CDF, SCD, TLC, TLD	TLC

2.2 Parawing Aircraft Design	CDF, MEW, WRS, TLD	WRS
2.2.1 Parawing Geometry	MEW, WRS	WRS
2.3 Hang Gilder Aircraft Design	CDF, MEW, WRS, TLD	WRS
2.3.1 Hang Glider Geometry	MEW, WRS	WRS
3.1 Low Fidelity Design Elimination	All	CDF, KCJ, RCD
3.1.1. Flight Scenario Selection	KCJ, RCD, WRS	KCJ, TLC
3.1.2. Design Ranking Weighted Equation	CDF, TLD	TLD
3.1.3. Design Space Exploration	KCJ, RCD, WRS	CDF, RCD, TLC
3.1.4. Obtaining Data for Design Space	MEW, TLD	TLD
3.1.5. Design Ranking Results	KCJ, RCD, WRS	KCJ, RCD
3.2 Fixed Wing Design	MEW, WRS	WRS
3.2.1 Initial Fixed Wing Sizing	MEW, WRS	WRS
3.2.2 Fuselage Design	CDF, TLC	CDF, TLC
3.2.3 Fixed Wing and Tail Plane Design	TLD	TLD
3.2.4 Fixed Wing Assembly	TLD	TLD
3.2.5 Fixed Wing Geometry Verification	MEW, WRS	MEW, WRS
3.2.6 Fixed Wing Structural Redesign	SCD, TLC	TLC
3.2.7 Engine Selection for Fixed Wing	MEW, WRS	MEW, WRS
3.3 Parawing Design	MEW, WRS	WRS
3.3.1 Parawing Sizing	MEW, WRS	MEW, WRS
3.3.2 Parawing Fuselage Design	CDF, TLC	CDF, TLC
3.3.3 Parawing Redesign	WRS. MEW	MEW, WRS
3.4 Hang Glider Design	MEW, WRS	WRS
3.4.1 Hang Glider Sizing	MEW, WRS	MEW, WRS

3.5 Fixed Wing Stability and Control Derivatives	MEW, WRS	MEW, WRS
3.5.1 ANSYS Fluent	MEW, WRS	MEW, WRS
3.5.2 Numbers from Similar Aircraft	MEW, WRS	MEW, WRS
3.5.3 Equations	MEW, WRS	MEW, WRS
3.5.4 Longitudinal Non-Dimensional Derivatives	MEW, WRS	MEW, WRS
3.6 Parawing Stability and Control Derivatives	MEW, WRS	MEW, WRS
3.6.1 ANSYS Fluent Analysis for the Parawing	MEW, WRS	MEW, WRS
3.6.2 Values from [52]	MEW, WRS	MEW, WRS
3.7 Trajectory Generation	KCJ, RCD	KCJ, RCD
3.7.1 6-DOF Model	KCJ, RCD	RCD
3.7.2 Control Equations	KCJ, RCD	KCJ
3.7.3 Trajectory Phase Transitions	KCJ, RCD	KCJ, RCD
3.8 High Fidelity Controllers	KCJ, RCD	KCJ
3.9 Structural Simulation	SCD, TLC	SCD, TLC
3.9.1 Fixed-Wing Structural Simulation	SCD, TLC	SCD, TLC
3.9.2 Parawing Structural Simulations	SCD, TLC	SCD, TLC
3.10 Subscale Hang Glider Build	CDF, TLD	CDF, TLD
3.10.1 Build Process	CDF, TLD	CDF, TLD
3.10.2 Selected Electronics	CDF	CDF
4.1.1 Fixed Wing Stability and Control Derivatives	MEW, WRS	MEW, WRS
4.1.2 Parawing Stability and Control Derivatives	MEW, WRS	MEW, WRS
4.1.3 Fixed Wing Controlled Simulations	KCJ, RCD	RCD
4.1.4 Parawing Wing Controlled Simulations	KCJ, RCD	RCD
4.1.5 Structural Simulation Results	SCD, TLC	SCD, TLC

4.2 Experimental Results	CDF, TLD	CDF, TLD
5 Conclusions	All	KCJ, RCD, MEW
5.1.1 Future Aerodynamic Analysis	N/A	WRS
5.1.2 Future Flight Simulation and Control	N/A	RCD
5.1.3 Future Structural Analysis	N/A	TLC
5.1.4 Future Subscale Evaluation	N/A	CDF

Nomenclature

AR	Aspect Ratio	T	Thrust
b	Span	$Temp$	Temperature
c	Chord Length	TR	Taper Ratio
$\bar{c}$	Mean Aerodynamic Chord	u	U-Direction Component of Velocity
C_x	Nondimensional Coefficient of x	v	V-Direction Component of Velocity
d	Distance	V	Velocity
D	Drag	$\bar{V}$	Volume Ratio
e	Oswald Efficiency	w	W-Direction Component of Velocity
g	Gravitation Constant for Earth	W	Weight
h	Nondimensional X-Direction Position along Wing	X_x	X-Direction Dimensional Coefficient
H	Altitude	y	Nondimensional Y-Direction Position along Wing
i	Incidence Angle	Y_x	Y-Direction Dimensional Coefficient
J_x	Second Moment of Inertia about X twice	z_{vt}	
J_y	Second Moment of Inertia about Y twice	Z_x	Z-Direction Dimensional Coefficient
J_z	Second Moment of Inertia about Z twice	γ	Climb Angle
J_{zx}	Second Moment of Inertia about Z then X	Γ	Dihedral Angle

k_x	Fractional Multiplier due to x	δa	Aileron Deflection Curve Slope
$k_{\varepsilon,\alpha}$	Down-wash Derivative	δe	Elevator Deflection Curve Slope
l	Length from Center of Mass	δr	Rudder Deflection Curve Slope
$\bar{l}$	Length from Wing Aerodynamic Center	δs	Symmetric Deflection of Parawing tip Curve Slope
L	Lift	δ_x	Curve Slope with Respect to X
$\bar{L}$	Length from Leading Edge	$\Delta(x)$	Change in X
l_x	Rolling Moment Dimensional Coefficient	ε	Downwash Angle
m	Mass	η	Efficiency
M_x	Pitching Moment Dimensional Coefficient	θ	Pitch Angle
N_x	Yawing Moment Dimensional Coefficient	λ	Sweep Angle
p	Position	μ	Dynamic Viscosity
P	Power	ρ	Density
q	Dynamic Pressure	ϕ	Roll Angle
R	Radius of Turn	ψ	Yaw Angle
S	Planform Area	$*$	Cruise Condition
t	Time		

Subscripts

ac	Aerodynamic Center	r, eff	Rudder Generated Side Force
$airfoil$	Values Based on 2-D Airfoil	t	Fuel Burn
a, eff	Aileron Generated Rolling Moment	T	Thrust
a, yaw	Aileron Generated Adverse Yaw	TO	Take-Off
c	Cruise	u	U-Direction Component of Velocity
cm	Center of Mass	v	V-Direction Component of Velocity
D	Drag	vt	Vertical tail

D_0	Parasitic Drag	$vtail$	V-Tail
$final$	Final	w	W-Direction Component of Velocity
$fuel$	Fuel	W	Wing
$guess$	Guess	wb	Wing and Body
ht	Horizontal Tail	x	X-Direction
htv	Vertical distance to Horizontal Tail/V-tail Aerodynamic Center	y	Side Force
l	Roll Moment	z	Z-Direction
L	Lift	α	Angle of Attack Curve Slope
L_0	Zero Angle of Attack Lift	$\dot{\alpha}$	Rate of Change of Angle of Attack Curve Slope
LE	Leading Edge	β	Side-Slip Angle
m	Pitching Moment	δ	Wing Tip Deflection of Parawing Curve Slope
n	Yaw Moment	δa	Aileron Deflection Curve Slope
p	Roll Rate	δe	Elevator Deflection Curve Slope
$proj$	Projected onto the x-y Plane	δp	Propulsion Increase Curve Slope
q	Pitch Rate	δr	Rudder Deflection Curve Slope
r	Yaw Rate	δs	Symmetric Deflection of Parawing tip Curve Slope
req	Required	0	Initial
$root$	Surface Closest to Aircraft Body	1	Cruise Condition

1 Project Overview

Since World War Two (WWII) the United States Army has used aerial delivery of cargo to deliver necessary supplies to its troops while they are in remote battlefronts. These supplies often include medical supplies, food, fuel, and ammunition. As technology has advanced this delivery method has shifted to autonomous vehicles such as the Joint Precision Airdrop System (JPADS). These systems rely on the interoperability of the US Air Force and the US Army as the army relies on aircraft flown by the US Air Force to drop the system to the troops below.

The goal of this project is to design aerial delivery vehicles that can increase the range of the existing systems by one order of magnitude as well as be launched from the ground. The outcome of this project can enable supplies to be delivered from safe locations without putting aircrafts into danger. It can also lower the cost of delivering supplies as more expensive aircraft are no longer needed to execute the supply missions. This falls in line with the expectations of the projects sponsor, the U.S. Army DEVCOM SC.

1.1 Project Objectives

The objective of the project is to design aerial vehicles to deliver 100-200 kg of cargo to destinations 200-500 km away and return. These vehicles need to be able to be ground launched and ideally would be capable of aerial launch. They will be completely autonomous and compatible with current airborne guidance units (AGU). The supplies they carry should be able to be delivered with a circular error probable (CEP) of 100 m. In repeated trials of any guided aerial system, the CEP is the radius of a circular region centered at the desired landing location that is expected to contain 50% of the trial landings.

1.2 Literature Review

1.2.1 Historical Development of Airdrop Systems

Precision Air Drop Systems (PADS) are continuously being redesigned and developed for both commercial and military uses. These Unmanned Aerial Vehicles (UAV) allow the military to ensure that soldiers on the ground have all the necessary supplies and are a crucial component of the supply chain. [1]. PADS have many stakeholders due to the high cost of development as well as the wide variety of potential recipients. In most situations the primary stakeholder is the soldier in need of supplies while performing military operations [1]. The soldier can also be replaced by a civilian in need of humanitarian aid in non-military operations. Other stakeholders include the military, who often provide the funding for PADS research and the government contractors who develop the technology [1]. The large number of stakeholders in PADS programs ensures that research is continually progressing.

1.2.2 Joint Precision Airdrop Systems (JPADS)

The Joint Precision Air Drop System (JPADS) is widely used by the US Air Force, Army, and Marines. It is designed to resupply soldiers when other means of resupply, such as direct delivery by cargo aircraft or ground vehicles, are unrealistic [1]. JPADS are deployed at high altitude and utilize a rapid air movement (RAM) parafoil to glide to the resupply zone. It also contains an Airborne Guidance Unit (AGU) which can operate the steering lines of the parafoil to guide the cargo to within 100 m of the resupply site [1].

The current unpowered JPADS are subject to several drawbacks. Due to limitations with RAM parafoils, the JPADS range is low, with a glide ratio of at most 3.5 and with a deployment altitude of approximately 7.5 km the parafoils only travel about 26 km [2]. Parafoils are susceptible to wind disturbances, due to which they may be easily diverted off the desired course and have limited control authority for corrective actions. Terrain can also prove to be an issue for the JPADS. Because they are only able to glide, they are not able to avoid any large terrain features such as mountains that may be in their way by gaining altitude and flying over the obstacle. The only solution parafoils would have to these situations would be to steer around the obstacle which depending on size may not be possible. These drawbacks make the system unusable in environments that have frequent high winds, large terrain obstacles, or crowded urban areas [1].

One approach to overcome some of these drawbacks as well as increase the accuracy of the system is to combine the current JPADS with a collection of quadrotors [3]. The typical payload of the JPADS is replaced by a dispenser containing quadrotors, each with their own payload. The JPADS then flies a normal mission and when near the resupply zone dispenses the quadrotors to each deliver small components of the supplies [3]. This does not solve all the issues faced by JPADS, however, as the result is still limited by the range of JPADS and subject to the low cargo capacity of the quadrotor UAVs; each UAV could only carry 7 kg of cargo [3].

Another approach to combat some of the drawbacks of the current JPADS is to use controllable cruciform parachutes. The main issue cruciform parachutes attempt to overcome is the cost associated with parafoil based JPADS. Both the parafoil and associated guidance unit are very expensive systems [4]. The cruciform parachute, however, is much less expensive to make. The cruciform parachute does not overcome the other issues associated with the JPADS, however. They tend to have much worse glide ratios, in the range of 0.5-0.7, and rely on very accurate weather forecasts similar to the parafoil systems [4]. Not only do cruciform parachutes have lower glide ratios, but they also tend to have poor accuracy, with a CEP of 128 m [4].

The use of satellite-derived wind profiles is another realm in which research is being performed to improve the effectiveness of JPADS. The region of flight in which wind is the biggest factor in JPADS accuracy is at the highest altitudes. The small regions at the beginning of high-altitude drops can account for more than 85% of the wind-based drift of the system [5]. This is the region where ground-based weather systems have the most difficulty accurately predicting the weather but also where satellites are most accurate [5]. By utilizing satellite-based systems risk is reduced on aircrew as they no longer must make multiple fly overs of the drop location to evaluate wind before dropping the JPADS [5]. The final advantage of satellite–based systems is that they do not depend on GPS in the same way previous systems do allowing JPADS to still be deployed when interference or jamming interrupts GPS signals [5]. While satellite wind systems do not increase the maneuverability of JPADS they do provide better estimations for drop location and allow for the JPADS to make smaller correction more often to stay on the planned trajectory [5].

1.2.3 Unpowered RAM Parafoils

In the current state of aerial delivery development, a PADS typically consists of a steerable, large-size, RAM parafoil controlled by electrically powered actuators that modify the shape of the parachute canopy. The actuators, computers, required sensors, and all other complementary components are usually located in an AGU either strapped between the parafoil and the payload or strapped directly to the payload [6]. An example of a parafoil schematic can be seen in Figure 1 below.

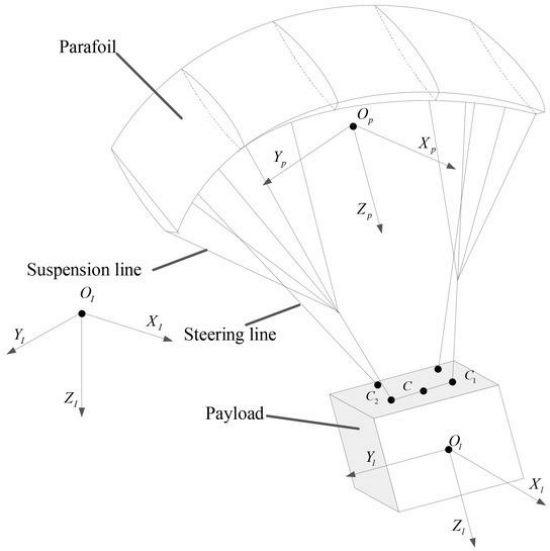

Figure 1 Illustration of a Parafoil System [7]

The standard PADS mission consists of first releasing the RAM parachute (with attached payload) out of an air carrier, deploying the canopy, and establishing a steady state glide. These first few steps result

in deployment altitude loss on the order of roughly 200-750m depending on the specifics of the PADS [6]. After achieving a steady glide, the actuators are used to maneuver the parafoil to the desired landing location, where it makes a final approach maneuver, or terminal guidance, to land at the intended point of impact. The standard deployment technique is referred to as high-altitude (deployment)/high-opening (HAHO). For this technique, the main canopy opens soon (within seconds) after the aerodynamic decelerator system (ADS) exits the aircraft. The alternative is the high-altitude/low-opening (HALO) technique, when a main canopy opens very close to the ground. The HALO technique was developed to mitigate the effects of unknown winds. Athough, is not as reliable as the standard HAHO technique that keeps the parafoil away from the drop zone which is usually required from an operational standpoint [6].

Since their introduction in the late 1960s, cargo aerial delivery systems based on controlled gliding parachutes have proven to have significant advantages compared to traditional round canopy parachutes [6]. A typical parafoil canopy is made up of five flat panels across the top, with two smaller side panels, or fins, that help to provide directional stability [8]. Currently, most parafoils make use of RAM canopies because they are capable of covering the range required for deliveries of recoverable payloads to the intended drop point by using guidance, navigation, and control (GNC) algorithms linked to the trailing edges. Additionally, they can achieve a glide ratio of roughly 3:1 [6].

In terms of modeling, there are many different degree-of-freedom (DOF) approximations and simplifications that can be made. Generally, low fidelity models such as the kinematic model, reduced order model, or linearized model are used in the design of GNC algorithms with sufficient knowledge of the aerodynamic coefficients, geometries, and general measurement parameters to accurately model the system. Higher fidelity models are typically only used when evaluating performance through simulation or alternatively during real flight tests [8]. Simple models range from particle assumptions to the 3-DOF and 4-DOF models. The 3-DOF model comprises of horizontal lateral and longitudinal motion as well as heading, while the 4-DOF model also incorporates roll [8].

A 6-DOF model is typically used in predictive control. In the 6-DOF model, the parafoil and payload are regarded as one rigid body. However, the model does not include the forces and moments resulting from the mass to volume ratio of the canopy [8]. Some models make the simplification that the parafoil and canopy are one cohesive body with the same forces and moments acting upon them, while other, more precise models recognize that they are two separate entities attached by flexible suspension lines (actuators) capable of changing their geometry and the aerodynamics during flight [8].

Regarding their limitations, parafoils are vulnerable to wind due to their lack of rigidity, meaning that their sensitivity to changes in the atmosphere significantly affects their trajectory if not properly controlled. Although the parafoil and payload may be rigid and aerodynamic, the canopy/parachute is flexible and can easily change its shape. In some more extreme cases, wind can force a system out of its stable state, sometimes causing the canopy to either collapse inward or deform resulting in the parafoil spiraling toward the ground [8]. However, with accurate wind predictions and sensor reading, GNC algorithms can mitigate the effects and error caused by the wind.

Autonomously guided systems using RAM parafoil canopies have proven to dramatically improve payload delivery precision as well as accuracy in comparison to the previously used unguided ballistic parachutes [9]. Typically, these parafoil systems are released from an aircraft at high altitudes, and the guidance algorithm is responsible for planning an appropriate path to reach the target landing area. The algorithm should make use of current state of the parafoil (position, velocity, orientation, etc.) and atmospheric wind conditions and output a "plan" to achieve steady flight to the target. The autonomous guidance usually consists of three separate phases: homing, energy management, and terminal guidance [10]. Homing steers the parafoil directly toward the target location using the actuators and a control mechanism (the trailing edge flaps for example). The energy management phase consists of the parafoil losing altitude above the target until a specific (parameterized) altitude is reached. Once this altitude is reached, terminal guidance begins. Terminal guidance steers the parafoil to its final landing point on the ground. This is the most crucial phase to achieve an accurate landing [10].

Working with the guidance algorithm, the navigation algorithm is responsible for continuously updating state and wind estimates as well as current vehicle heading and heading rate information [10]. The navigation algorithm uses onboard sensors and previously calculated predictions to achieve an accurate representation of the current motion of the parafoil and its surroundings [10].

As for the control of the parafoil, changing the position or length of flexible actuator lines (located throughout the canopy) results in a deflection of the canopy's trailing edges, which, in turn, steers the parafoil in the desired direction [9]. Current autonomous parafoil systems are controlled via asymmetric brake deflection on the right and left sides of the canopy. For all constant-radius segments of the vehicle path planned by the guidance algorithm, the asymmetric spoiler deflection is held constant and can be considered an open loop until the required change in vehicle heading angle is achieved [9]. This provides an effective means for lateral–directional control. In contrast, symmetric brake deflection causes a reduction in forward flight speed resulting in small changes to the system's system glide slope until stall [9].

Similar to conventional rigid body aircraft spoilers, some parafoil systems possess several spanwise slits in the upper surface of the parafoil canopy known as “bleed-air spoilers”. When opened, these slits create a virtual spoiler by creating a disturbance in the airflow over the canopy, which releases pressurized air that is stored in the canopy cells [9]. Correspondingly, this action results in a change of the aerodynamic forces acting on the parafoil, payload, and canopy. Varying the location of these slits along the upper surface of the canopy has the potential to significantly change the lateral and longitudinal dynamics of the system for a wide variety of purposes [9].

Additionally, adding longitudinal glide slope control is an effective means for reducing impact point errors and can further improve landing accuracy [9]. There are multiple different methods of effective glide slope control including in-flight adjustment of the canopy incidence angle, symmetric brake deflection for airspeed control, and actuation of upper-surface bleed air spoilers [10].

Although parafoil GNC algorithms significantly improve the accuracy of payload drops, there are several factors that complicate the control schemes compared to those of rigid body aerial delivery options. One complication is that parafoils have very large turning radii and little to no control over vertical descent rate because they are unpowered [10]. There are also a limited number of control channels because there are a limited number of panels on the canopy that the actuator lines can control. Typically, a parafoil canopy is composed of 8 panels, and the actuators typically only control the trailing edges and occasionally a few surface panels [8]. The GNC is even further complicated when considering the effects of variable atmospheric conditions such as thermals or wind speed and direction. If a system is using wind prediction rather than sensing and wind measurements, any deviations from the assumed wind can drastically hinder the effectiveness of the guidance algorithm [9].

1.2.4 Other Potential Systems

Currently there are many unmanned aerial vehicle (UAV) delivery systems being investigated for use. One such system focuses on the use of single surface gliding cargo airdrop systems. These systems, originally designed by the National Aeronautics and Space Administration (NASA) for spacecraft recovery, are composed of flexible materials designed to be deployed and used like a parachute [11]. When compared to traditional RAM parachutes, single surface designs are less complex, use fewer materials, and are easier to manufacture because they only have one surface [11]**.** These single surface designs also tend to be lighter and pack smaller than a similar RAM parachute. However, there are drawbacks. Single surface designs typically have glide ratios that are lower than that of their RAM counterparts, are more difficult to control and require a complex procedure for deployment [11]**.** When testing two single surface designs, the Twin Keel design and Hybrid Single Surface design, DEVCOM SC was unable to develop a deployment method

that ensured the parachute did not fail upon opening [11]. This difficulty led to very little research being performed on single surface glide systems.

Ballistic drop parachutes are commonly used to deliver large amounts of military supplies. These parachutes are typically round and used for unguided aerial delivery. The round shape makes them difficult to control thus they tend to be very dependent on atmospheric conditions for accuracy. They also tend to have very low glide ratios, typically between 0.8 and 1.0 [12].

Another system that can be potentially used for cargo delivery are quadrotor UAVs. These UAVs are often small, highly maneuverable, and can be operated either remotely or autonomously. They do however face several challenges. The small quadrotor UAVs often have very short flight times, typically around 30 minutes [13]. The second is they are severely restricted in the amount of cargo they can carry, typically between 2.2-6.8 kg [13]. Some larger quadrotor UAVs do exist, however. The EHANG 184 is a large quadrotor UAV capable of carrying 100 kg of cargo [14]**.** Along with this higher carrying capacity comes a smaller flight time and shorter range. The EHANG can fly for at most 25 minutes only traveling about 40 km in that time [14]. These restrictions hamper the effectiveness of quadrotors on long range missions of more than 100 km when carrying medium to high payloads of more than 100 kg.

Fixed wing vertical takeoff and landing (VTOL) UAVs are another system being investigated. VTOL systems tend to be significantly faster than parachute-based systems, due to their fixed wing nature not restricting them to lower flight speeds [15]. They face many of the same drawbacks of the quadrotors, however. They are limited to around 45 min of cruise time and have almost no payload lifting capabilities [15]. While some research is being done into adding payload capabilities to these UAVs, it is in the form of lightweight Intelligence, Surveillance, and Reconnaissance (ISR) [15]. Currently, this style of UAV is not feasible for long range, medium to high payload resupply missions.

In this project, we evaluate three other types of aerial delivery systems: a fixed-wing aircraft, hang glider, and a parawing aircraft. Fixed-wing aircrafts can achieve longer flight duration due to a high lift-to-drag ratio [16]. When viewed in comparison to quadrotors, fixed wing UAVs are able to carry heavier payloads. Due to the wing structure, this system can perform under strong wind conditions as well as having the ability to achieve higher speeds. Some of the issues within this system come from the need for more advanced control systems to pilot and operate the fixed wing system. Also, when going to land, because the UAV travels at higher speeds, if there's any mistakes upon landing it can lead to serious damage done to the UAV.

Hang gliders, due to their rigid tubular structures, have shown the ability to maintain a more stable flight when faced with wind turbulence [17]. Also due to the structure of this system, it is able to achieve a

high glide ratio as well as the system being highly maneuverable. One of the drawbacks regarding hang gliders is its' the turn radius. Since hang gliders have a high turn radius it prevents the system from operating successfully within smaller, tighter environments which hinders its' versatility.

A parawing is a general term for a self-inflating, delta wing geometry [18]. They have leading edge supports and cross braces around which a flexible material creates the delta wing geometry along with two "lobes." These lobes are commonly either circular or parabolic in cross-section; and a larger peak lobe height is correlated with an increase is zero-lift angle [18].

Figure 2 Rogallo Parawing tested for spacecraft landing Source: NASA

Parawing geometries in small UAVs can be "morphed," changing the wing geometry, typically for storage purposes. Because of its stowable size and low packing times, air deployment from other aircraft is easier [19]. The parawing can attain speeds of up to 125 meters per second and has natural resistance to atmospheric turbulence. It is also stall resistant, with some designs having stall angles over 40 degrees [20]. This is an improvement upon two weaknesses in a parafoil design [19], [20]. Parawings can be configured in many ways, without having a large effect on the aerodynamic capability of the UAV [19]. Little experimentation has been done on large scale parawing systems, with the upper end of weight limitations being around 200kg [19]. Some disadvantages to parawing systems are the weight limitation, complexity, and scalability [20]. Therefore, parawings have historically had great applications in small UAVs, typically doing reconnaissance [19], [20].

1.2.5 Propulsion and Power in Aerial Delivery Systems

UAVs with propulsion systems are ideally used for military reconnaissance, as they typically fly slower than fixed wing aircraft due to their semi-rigid structure and can carry payload sizes necessary for both situations. Specifically, powered parafoils have similar flight characteristics and system dynamics to

unpowered RAM parafoil systems. This thrust typically comes from a back mounted propeller on the payload. When the motor is shut off, they can be modeled the same as these unpowered systems. However, when the motor is turned on, thrust is produced, allowing the vehicle to maintain altitude or climb. These systems are modeled after flexible wing aircrafts due to the addition of thrust. One of the main ways of creating lift in powered flight is through the implementation of airfoil shaped parafoil canopies [21]. However, more rigid structures can also be used in the application of powered aerial delivery systems. This section investigates what power systems could be implemented in a parafoil design, as well as other possibilities for propulsion systems taken from fixed wing examples.

The advantages of powered parafoils include higher velocity that is almost double that of unpowered parafoils [15]. Powered systems also do not rely on specific wind direction or weather as heavily as unpowered systems. Some disadvantages include the noise of the motor and propeller, which may cause these vehicles to be more detectable if flying at low altitudes, as well as the slow-moving radar signature compared to fixed wing aircrafts, which may cause these vehicles to be more detectable by radar at high altitudes [22].

There has been conflicting research on the efficiency of electric engines, especially for powered parafoils. Most motors used in parafoils or parawings today generally have internal combustion engines, though electric motors have also proven to be simple, reliable, and are much quieter, without exhaust gas emissions [22], especially when used in a hybrid system with others, acting as both a motor and a generator [23]. The specific structure and design of a UAV's electric propulsion system can greatly affect the payload capacity, flight time, and the overall endurance of the UAV. However, the propulsion systems for electric engines do not perform as well as internal combustion engines at lower altitudes [23].

In terms of methods of thrust generation in these different flight scenarios, some methods of propulsion were eliminated before simulation through research. Given the design parameters for this project, electric propulsion was able to be eliminated based solely on the fact that batteries have one of the worst mass and volume energy densities of all methods of power generation. This is exhibited in **Error! Reference source not found.**, where batteries and other forms of electric energy storage are located at the bottom left, meaning their mass energy density is inefficient. More ideal forms of energy storage and power generation would fall towards the top right of this plot. Thus, internal combustion engines, using fuel such as jet fuel will provide much more weight to energy ratios. Additionally, internal combustion engines perform exceptionally well at low altitudes, which makes them ideal for parafoil or parawing systems [23].

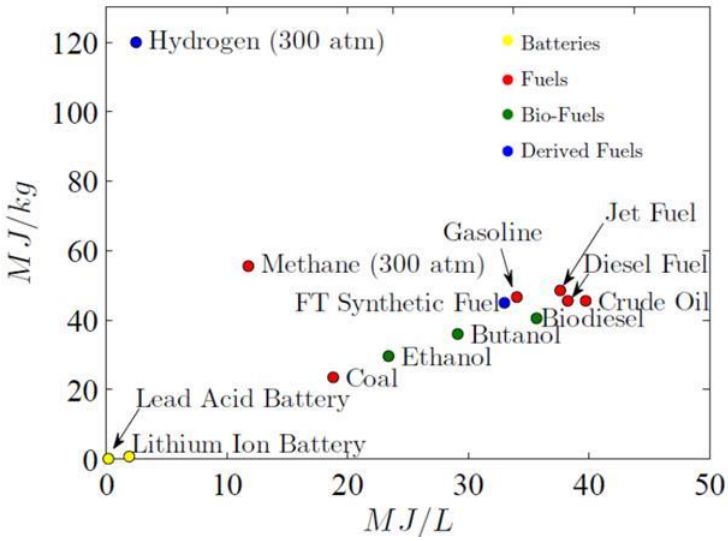

Figure 3 Energy Density per volume and per unit mass for various batteries and fuels [24]

Fuel cells for propulsion are of particular interest for long-range UAV missions because of the performance advantages that arise from constructing efficient power plants. Theoretically, power plants can produce high specific energy, low thermal signature, low noise, and improved environmental compatibility in comparison to other fuel sources, so modeling a fuel cell based on a powerplant should produce the same benefits [25]. In 2003, AeroVironment, Inc., manufactured and flew the first fuel-cell-powered aircraft. It made use of a polymer electrolyte membrane (PEM) fuel cell system, which consumes hydrogen from a sodium borohydride reaction vessel [25]. A variety of hydrogen storage systems have been tested for UAV flight use including gaseous pressure vessels, chemical hydrates, and low-pressure cryogenic liquid hydrogen tanks. One notable outlier to the hydrogen storage trend is the propane-fueled solid-oxide fuel cell (SOFC) UAV that was constructed in 2006 by Advanced Materials, Inc. [25]. Additionally, since the 2003 AeroVironment success, there have been several notable UAV demonstrations. In November of 2007, the Ion Tiger team (comprised of The US Naval Research Center, Protonex Technology Corporation, the University of Hawaii, HyperComp Engineering, and Arcturus) successfully flew their fuel-cell powered UAV for 26 hours 1 minute while carrying a 2.26796 kg (5lb) payload [26].

Solar cells are one of the most widely used sources of alternative energy to date. On a UAV, solar energy can be used to charge the battery while the vehicle is gliding, which is done intermittently between sections of powered flight. This allows the system time to convert solar energy into electric power, creating a more efficient process than regular motors [27]. UAVs have set general aviation records for longest continuous flight, set by the Qinetiq Zephyr for flying without rest for over two weeks, as well as greatest sustained altitude, set by the NASA Helios, which reached an altitude of 29260.8 m (96,000 ft). These

records were attained because the system stores solar power collected throughout the flight, which helps to prolong flight time and maintain altitude [28].

Although solar cells seem like an efficient and successful power source, there are a few possible issues that arise when designing a parafoil system. To power a UAV with solar cells or solar panels, the UAV must have some specific physical characteristics. First, solar cells need to be able to absorb direct sunlight, so they would most likely need to be placed on top of the parafoil or parawing. This is not feasible because solar cells are too heavy to place on top of a parafoil or parawing and have it continue to maintain altitude. Because parafoils do not have rigid wings, there is no space to hold the solar cells. Therefore, a UAV with this type of power would need a large enough wing surface area to hold the cells, which would most likely be available on only a fixed wing system, or a smaller UAV without a parafoil attached. Additionally, solar cells have been successful on UAVs that are significantly smaller than the design for this project [29]. They also depend heavily on external weather conditions, causing more limited usage [30].

Another power option that has been useful for long range missions is the hybrid electric propulsion system. This could include a combination of any number of systems, such as fuel cells, batteries, and solar cells, where they are integrated into a single power system. Hybrid systems using solar cells in some combination tend to have generally low payload capacities and need large lift to drag ratios to perform at the same level as other hybrid systems [30]. For hybrid systems using both fuel and electric power, the benefit is that they can use the fuel to directly power the motor, while keeping the battery charged using the electric power. This can increase the overall range of the UAV and allows it to fly the same distance as other hybrid engine UAVs, but with less fuel on board [31].

1.2.6 Control of Powered Parafoils/Paragliders

The powered parafoil consists of the same basic setup as an unpowered RAM parafoil with the addition of thrust generation. Thrust generation in a parafoil system allows for constant altitude flight and climb allowing for flights that last as long as the fuel tank. This, in addition to low-cost, high payload weight threshold, and ground launch capabilities makes powered parafoils a promising choice for long-range supply missions where conventional means are not an option [32].

One of the disadvantages to powered parafoils compared to other supply methods are high wind susceptibility and low-speed flights. Powered parafoils can operate at 10-20 m/s depending on wind, which results in high mission times of around 4-5 hours for 200-km ranges [26]. Winds also have a substantial effect on the stability of the parafoil, leading many guidance and control schemes to attempt to reject these disturbances as much as possible using active disturbance rejection control [32], [33].

Several control theories have been tested where powered parafoils are concerned including the traditional feedback Proportional Integral Derivative (PID) controller [34]. However, since powered parafoils operate at airspeeds on the same magnitude of as the variable winds that that perturb the lower level of the atmosphere, simple feedback control is not enough [34], [35]. One solution to this that can be seen through research is Active Disturbance Rejection Control (ADRC) paired with wind feedforward compensation. This methodology considers the variable wind by using it as an input into the control algorithm [34]. When applied to a PID controller this method allows for better trajectory tracking, and minimizes the error caused by the variable wind [34].

Historically, applications of these systems have been relegated to recreational use, largely due to the difficult guidance and control schemes that come with them. For proof of concept, the longest manned flight of a powered parafoil was by Lauri Kadakas, in which he flew 1132.7 km in over 15 hours, with a grounded take-off weight of around 200 kg [36].

1.3 Design Requirements, Constraints, and Other Considerations

In this project we consider the design of a system required to be able to fly a minimum of 200 km with a payload of at least 100 kg. Ground launch capability is required. Compatibility with existing AGUs is desired to achieve a CEP of 100 m. While these are the base requirements there are additional desired characteristics for the system. These include a range of 1000 km (500 km to target and 500 km back), carry a 250 kg payload, be able to be air launched, perform in a wider variety of environments than the current JPADS system, such as environments with mountainous terrain or urban environments, and improve packing time over the current JPADS system.

Other considerations the team made focused around the economic impact and impact on the recipient of the payload. The system needed to be as cost effective as possible. This meant that the system should be cheap to manufacture, reusable, and utilize as little fuel as possible. The system also needed to deliver the payload in a timely manner. When delivering supplies to soldiers on the ground or survivors of natural disasters time is critical, so the faster supplies could be delivered the better the system.

1.4 Project Management

Initially, the team was divided into three main sub-teams: aerodynamics, propulsion, and simulation. The aerodynamics sub-team consisted of MEW and TLD. This team was responsible for gathering the aerodynamic coefficients for the various lifting systems utilized in the determination of the final two systems the team will be more extensively researching and developing.

The propulsion team consisted of CDF, SCD, and TLC. This team was responsible for finding the engine parameters that were used to determine the final two systems for the team. This team also developed

code in conjunction with the aerodynamic sub-team to evaluate potential engines for use. The two teams also utilized XFLR5 to develop the coefficients used in the final ranking of the potential systems.

Sub-team three was the simulation team and consisted of KCJ, RCD, and WRS. This team developed code to simulate the flight of the various systems. Taking the data provided by the first two sub-teams the simulation team created a 3-DOF model and simulated it over a range of scenarios which considered different launch and cruise conditions. The two best ground launch scenarios were then taken, and a second code was written which utilized a weighted ranking equation written by TLD and CDF. The code simulated those two scenarios for a wide range of fuel volumes, planform areas, specific fuel consumptions, mass of payload to total mass fraction, and power. The ranking code was also used in determining the final to systems that would be evaluated more thoroughly in later terms.

Halfway through the project year, the team was re-divided into four sub-teams: build, aerodynamics, structures and thermal, and simulation. The build sub-team consisted of TLD and CDF. The build sub-team responsibilities included making working CAD models for the other teams to analyze in simulation programs, as well as designing and building a scale prototype.

The aerodynamics sub-team consisted of MEW and WRS This sub-team was responsible for gathering aerodynamic coefficients using Fluent simulations on the working model. These coefficients were then handed off to the simulation team for higher fidelity models.

The structures and thermal sub-team consisted of SCD and TLC. Responsibilities of this sub-team included running Ansys FEA (Finite element analysis) simulations on the working CAD model to determine static equilibrium. Results from the structures team were reflected in changes to the working CAD model.

The simulation sub-team consisted of KCJ and RCD. The main goals of this sub-team did not change significantly after the reorganization. The focus was placed on higher fidelity models based on the values from the analysis sub-teams, as well as simulating different maneuvers.

The team met many times throughout the week. Meetings with the advisor Professor Cowlagi were scheduled on Tuesdays at 0900-0930 as well as with Professor Cowlagi and the sponsor Dr. Noetscher on Fridays from 1400-1500. During these meeting the team presented slides created by each sub-team with a different team member leading each meeting. The team also met on Mondays, Thursdays, and Fridays from 0900-1000. In addition to meetings the team utilized both Slack and Microsoft Teams to manage tasks, organize documentation, and communicate between meetings.

1.4.1 Tasks and Timetable

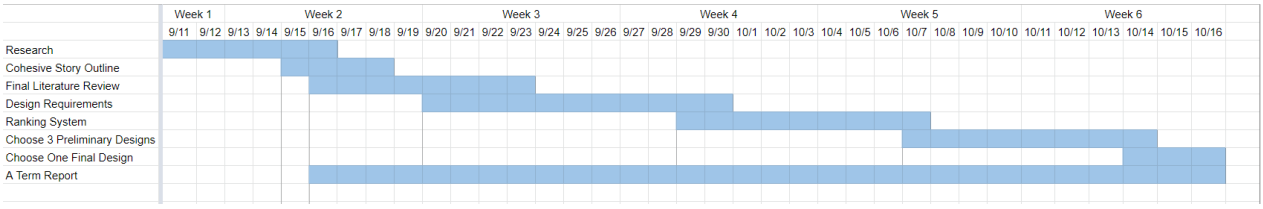

Figure 4 A-term Gantt Chart

Compared to the initial plan shown above, the team was able to stay on schedule through most of the term. However, it did not take as much time to create the ranking code as anticipated, so that task was completed early. The initial plan to choose three preliminary designs, then one final design this term changed as well. It was later decided that this term, the team would narrow its focus to the two best ranked systems after running the ranking code. These two systems would be carried into B term, where they would be developed further into medium fidelity models to better compare them. Both designs were chosen on October 16 after successfully running the ranking code.

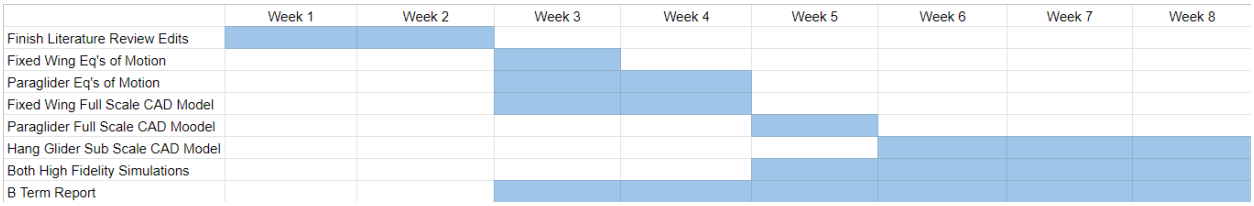

Figure 5 B-Term Gantt Chart

The high-fidelity simulations were not developed. After this Gantt chart was created, the simulation sub team reevaluated our goals and our focus shifted. Instead of developing high fidelity simulations, we increased the fidelity of our previous simulation while also creating a trajectory that our simulations where controllers would try and guide the aircraft to that trajectory once created. The CAD models were delayed in their completion due to structural setbacks but were still completed.

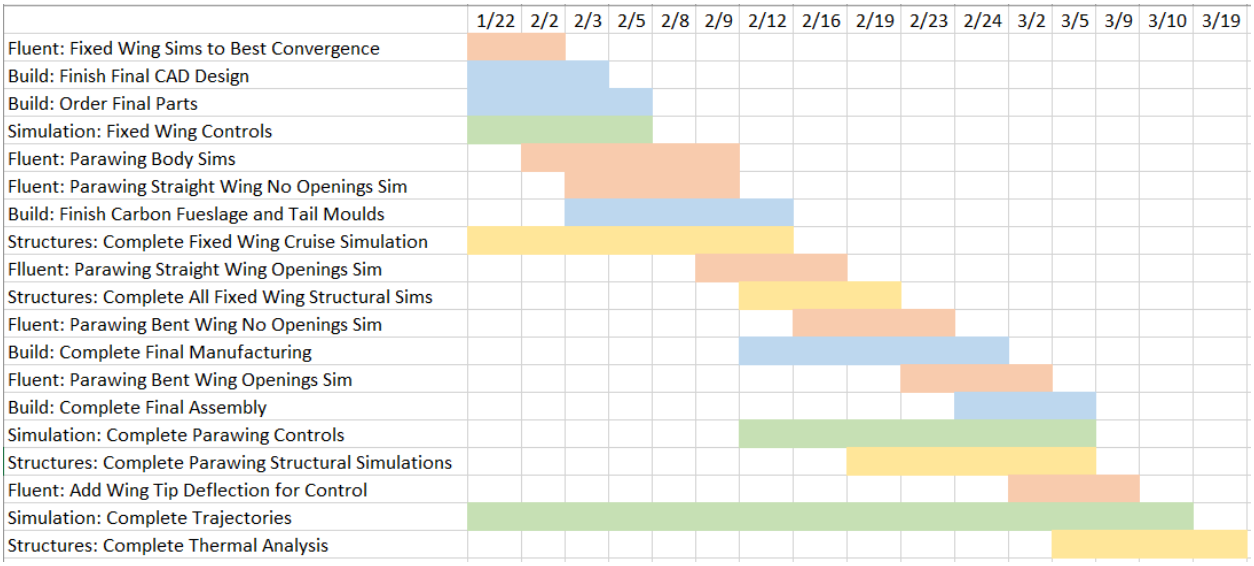

Figure 6 C-Term Gantt Chart

The Fluent simulations schedule outlined in orange in Figure 6 was not followed exactly as there were issues that arose which caused the last few simulations to be delayed by about a week. Due to the setbacks in the Fluent Simulations, the parawing controllers were not completed until D term. An additional wind model was created during the time that the parawing controllers were intended to be completed in an effort to make the testing of the controllers more accurate as well. The structures team was overall unable to complete all the tasks listed on the Gantt chart due to multiple delays. The early fixed wing simulation required more troubleshooting and bug fixing than was first thought, as the structures steam was new to ANSYS. After the first structures results for the fixed wing, there was another delay while waiting for the CAD model to be updated to reflect the results. Because of these setbacks, the structure team was unable to fully complete parawing and thermal simulations.

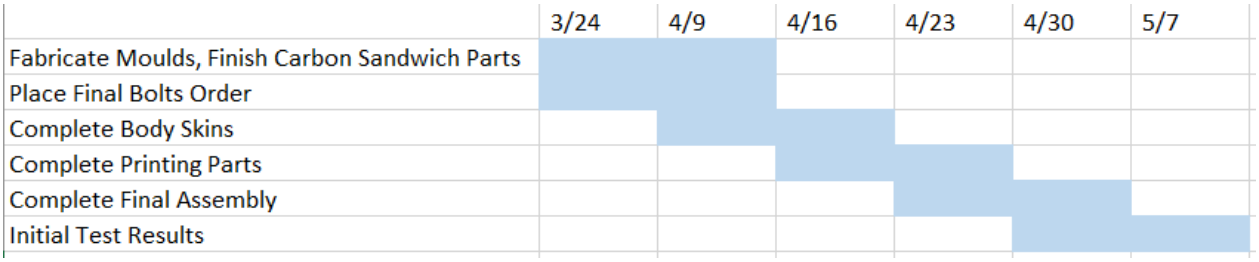

Figure 7 D-Term Build and Test Schedule

The Build team schedule outlined in blue as seen in Figure 7 was not followed due to unforeseen issues that occurred throughout the entirety of the build process. Due to issues that arose within the CAD model throughout the beginning half of C term resulted in the beginning of the manufacturing process being delayed until the end of C term. Throughout the manufacturing process the team ran in to several different

issues such as lack of needed materials and different structural failures. Due to all of these setbacks, the team was unable to fully complete the entirety of the build process.

1.5 Relevant Engineering Standards

Several common engineering standards were used throughout the course of this project. One of these standards was the NACA standard airfoils database. NACA airfoils were used for the wing, horizontal tail, and vertical tail of the fixed wing aircraft. Other standards that were used include ANSI C18.3M standard for portable lithium batteries and NEMA ICS 16-2001 standard for servomotors and stepper motors. These were both utilized during the parts selection phase of the small-scale build. Finally, the packing standards for military parachutes were considered when making final conclusions about the viability of different systems as well as MIL-STD-704 for interfacing with aircraft power.

1.6 Methods

Table 1 lists the methods used in the completion of this project, as well as a brief summary of what each method was used for.

Table 1 Methods Used in the Completion of this Project

Method	Uses
MATLAB/Simulink	This program was used for the design space exploration, macroscopic trajectory analysis, and the high fidelity controller creation
SOLIDWORKS	Model Design and Adaptation for simulations and build plans. Additionally, used for mass properties and determining inertia matrix for control and dynamics simulations.
XFLR5	This program was used in the initial evaluation of different systems. Additionally, it was utilized in the initial design process of the fixed wing, parawing, and hang glider systems.
Ansys Workbench	This program was used to import design geometry from SOLIDWORKS, apply/edit material properties, and then import these materials and geometry into simulation programs.
Ansys Fluent	Ansys Fluent was used to gather aerodynamic characteristics of the fixed wing aircraft designed by the team. It was also used to gather lift data for the parawing the team used.

Ansys Mechanical	Ansys Mechanical was utilized to run static structural simulations of the main wing under cruise conditions. Applying force vectors, gravitational forces, and material assignments, in order to run a numerical simulation of deformation and stress.
Carbon Layup	Carbon Layup was used in order to develop carbon fiber molds of the wing, tail and fuselage components in order to develop the overall model. Creating carbon fiber sandwiches were developed using epoxy and foam core cut outs of the different parts needed.
Additive Manufacturing	Additive manufacturing was used to create the fuselage rib spares and the wing end stops. The mold used as shape the shell of the fuselage was also created through the additive manufacturing.

1.7 Broader Impacts

The impacts of long-distance precision air drop systems are widespread and far reaching. In terms of available delivery vehicles on a small scale, there are many valuable ways that this technology is utilized today. For example, in 2012, after hurricane Sandy, Haiti utilized UAVs for many kinds of mapping including topographical and 3-D maps for destroyed buildings, taking count of public service buildings (e.g. hospitals), and monitoring displaced citizens [37]. These mapping missions in addition to direct delivery of supplies help limit disaster risk and increase overall efficiency of ground action by emergency personnel [37]. Aside from mapping and relief delivery, there are other uses that have yet to be implemented in current humanitarian aid. NASA's Finding Individuals for Disaster and Emergency Response radar detector (FINDER) could be used to locate individuals trapped under rubble by using sensors to detect heart rates, breathing patterns, and mobile phone signatures [38]. Larger scale deliveries of medical supplies to remote locations can increase the quality of life for many people who may not have access otherwise [38].

Challenges to consider range from potential environmental concern, criminal use, privacy and data collection. For gas powered vehicles, carbon emissions are always something to consider as an impact. In addition to this, limiting exposure of the aircraft to potentially dangerous landing areas where forest fires could break out (e.g. brush) will be an important safety concern if flammable or high temperature parts are included. If electrical components and engines are being used, issues of recycling and disposal arise. Potential criminal use of this technology includes smuggling. These challenges are exacerbated by a lack of small UAV regulation in countries where humanitarian aid is needed most [37].

Economically, if long-distance precision air drop with ground launch capabilities starts gaining traction in the private sector, it could lead to many new markets and jobs. These vehicles could find a potential niche in freight deliveries to remote or otherwise hard to reach locations. This could lead to economic stimulation of potentially marginalized areas. On a large scale, more regulation is needed to fly shipping operations due to airspace restrictions [39]. Currently the biggest prospective economic markets for these systems are in precision agriculture and public health and safety [39]. “Precision agriculture” refers to the accurate sensing of certain crop markers like growth rates, hydration, and blight outbreaks [39]. The precise measurement of these markers allows farmers to selectively spray crops, increasing efficiency and decreasing environmental impact [39]. The Association for Unmanned Vehicle Systems International estimates that within the first 3 years of integration, the economic impact could total $13.6 billion, with 70,000 new jobs [39].

2 System Design

All three designs were based on a simulated payload volume of 129.54x76.2x53.4cm. This volume was estimated from the dimensions of ammunition crates, MREs, and water. The calculation of this volume is based on an even layer even stacking assumption and total mass of 250kg. First the maximum amount carriable was calculated by dividing the total mass by the respective weight of each payload object and rounding the resultant number down. Then the resultant number was divided into even layers and the total area for each was calculated. To note the MREs are rotated in order to fit into the volume.

Table 2 Source Data for Payload Volume Calculation

Item	Dimensions(Lx WxH)	Weight	Density
Standard Ammo Can	.432m x .1778m x .3810m	5.56: 13.6078kg	464.99 kg/m^3
Standard 5 Gallon Container	.3429m x .1524m x .4826m	Water: 18.9kg Diesel: 15.8757kg	Water: 749.41kg/m^3 Diesel: 629.49 kg/m^3
Standard Box of MREs	.4064m x .2921m x .245m	9.07175kg	311.91 kg/m^3

2.1 Fixed-Wing Aircraft Design

Using the iterative process described later in Section 3.2, a fixed-wing aircraft was designed. The overall design was selected due to its similarity to other successful aircraft with similar mission sets, such as the Cessna 182. While these other aircraft are not autonomous and are meant to carry people from one location to another, they have similar total payload capacities and similar ranges as the desired specifications for our aircraft. Therefore, these aircraft provided a baseline design for this project. The fuselage and the entire fixed wing design can be seen in Figure 8.

The fuselage design, detailed in Figure 8, involved minimizing volume to allow room for strictly the payload and engine compartment. A cylindrical spar running lengthwise down the top of the interior of the fuselage and extending out the rear is also included to provide the mechanism to support tail surface mounting. A nosecone was also added in the form of a semi-sphere however in practice this would be replaced by the propeller and the parts to connect it to the motor.

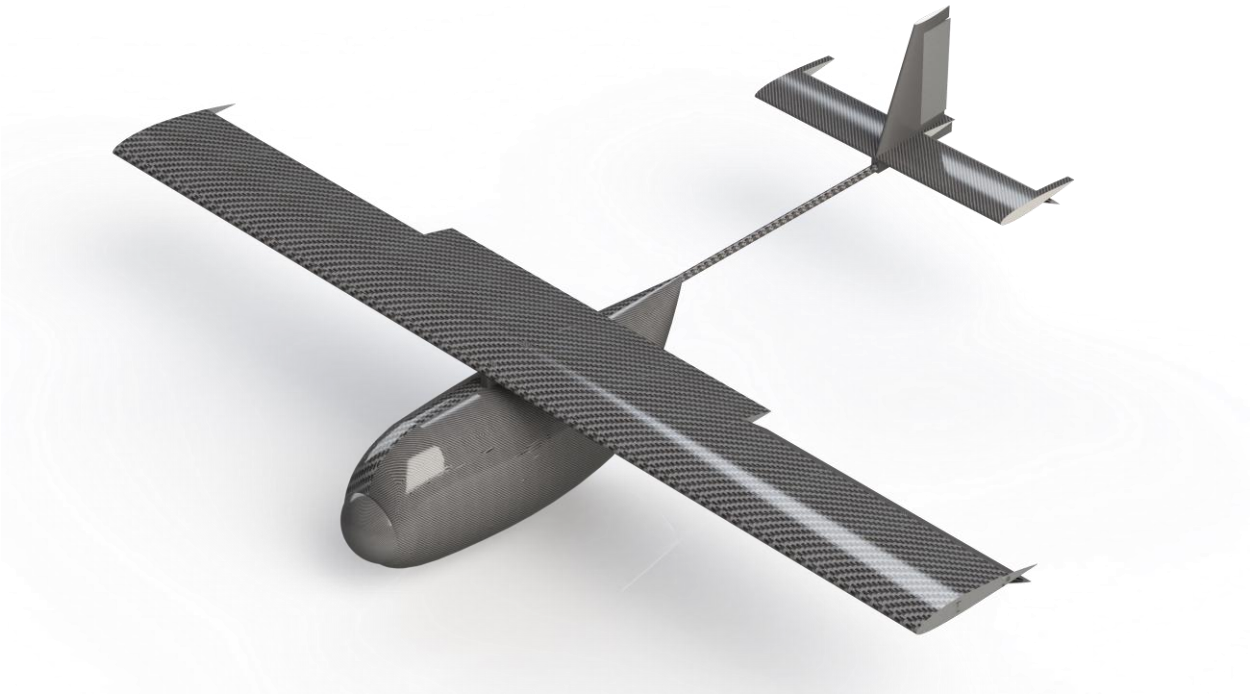

Figure 8 Fixed-Wing Final Design

2.1.1 Fixed Wing Geometry

The geometry of our aircraft was dictated by size requirements for the payload as well as proven design characteristics from other aircraft. The dimensions listed in Table 3 below were either chosen or derived with these two factors in mind.

Table 3 Fixed-Wing Dimensions

Variable	Value	Variable	Value
m_0	1000 kg	W_0	9810 N
S_w	15 m^2	S_{ht}	3.28 m^2
S_{vt}	0.9 m^2	b_w	10 m
$\bar{c}_w$	1.5 m	$\bar{c}_{ht}$	1.04 m
$\bar{c}_{vt}$		h_{vt}	1.246 m
h_{ac}	0.25	h_{cm}	0.14

AR_w	6.67	AR_{ht}	3
AR_{vt}	3.45	l_{LE}	5 m
$\bar{l}_{ht}$	4.885	l_{vt}	5.0225 m
TR_w	1	$\bar{l}_{htv}$	0
TR_{vt}	0.5	TR_{ht}	1
λ_w	0 deg	Γ_w	0 deg
i_{ht}	0 deg	ε_0	0
e	0.8489	y_{ac}	0
z_{vt}	0.5538	$\bar{V}_{ht}$	0.7121
$k_{\varepsilon,\alpha}$	0.3243		

Most of these values were chosen during the design process in order to meet the lift requirements for the aircraft and were based on similar sized aircraft. However, some of the values were calculated using the equations below. The equations were taken from lecture notes provided by Professor Cowlagi [40].

$$AR_{vt} = \frac{2h_{vt}^2}{S_{vt}} \quad (1)$$

$$e = 1.78(1 - 0.045AR_w^{0.68}) - 0.64 \quad (2)$$

$$\bar{l}_{ht} = l_{LE} - 0.25\bar{c}_w + 0.25\bar{c}_{ht} \quad (3)$$

$$V_H = \frac{\bar{l}_{ht}S_{ht}}{\bar{c}_w S_w} \quad (4)$$

$$z_{vt} = \frac{1}{3}h_{vt}\frac{(1 + 2TR_{vt})}{(1 + TR_{vt})} \quad (5)$$

$$k_{\varepsilon,\alpha} = 4.44\sqrt{1-M^2}\left[\left(\frac{1}{AR_w} - \frac{1}{1+AR_w{}^{1.7}}\right)\left(\frac{10-3TR}{7}\right)\left(\frac{1-\frac{\bar{l}_{htv}}{b}}{\left(2\bar{l}_{ht}\right)^{0.33}}\right)\sqrt{\cos(\lambda_w)}\right]^{1.19} \qquad 6$$

2.1.2 Fixed Wing Structural Design

A 2x2 PREPREG carbon fiber was the material of choice for the fixed wing design as it is a lightweight material with high in-fiber strength. The orthotropic properties of this material adds another dimension of complexity to this design. The fibers are aligned such that the maximum principal stress is compressive with respect to the fibers.

Much of the structural integrity for the fixed wing design was focused on the main wing under cruise conditions. A design based on two main I-beam spars and 4 secondary spars, paired with 11 ribs evenly spaced span-wise presented a structural design capable of less than 4% wing deflection under cruise conditions. The design pictured in was the final design used to produce results when simulated in Ansys. was the final design used to produce results when simulated in Ansys.

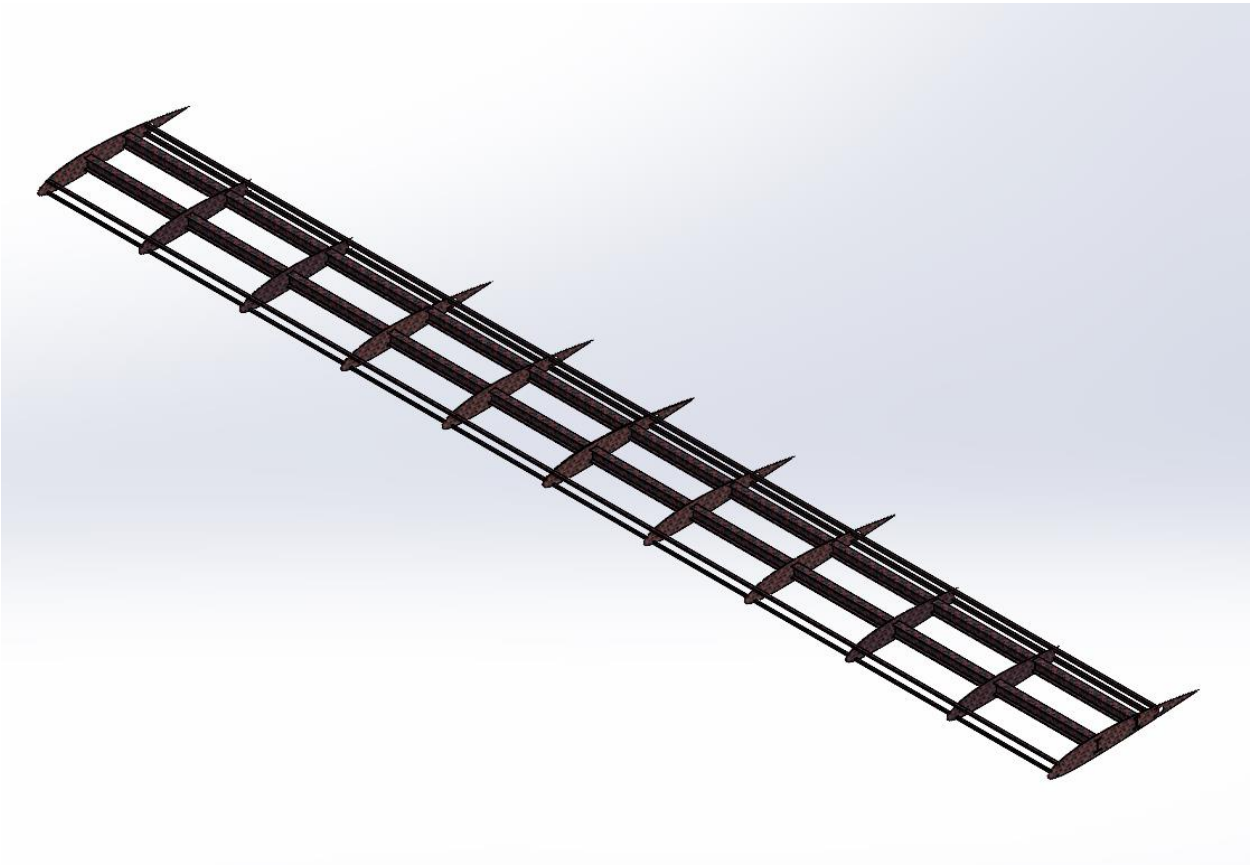

Figure 9 Fixed-Wing Main Wing Structural Design

2.2 Parawing Aircraft Design

Using the iterative process described in Section 3.3, a parawing aircraft was designed. The overall design was selected based on the Windtech Cargo paraglider system [41]. While this system is typically used to carry a single passenger, it is a system that has been used with thrust previously. This made it ideal as the basis for our design which made it larger and autonomous.

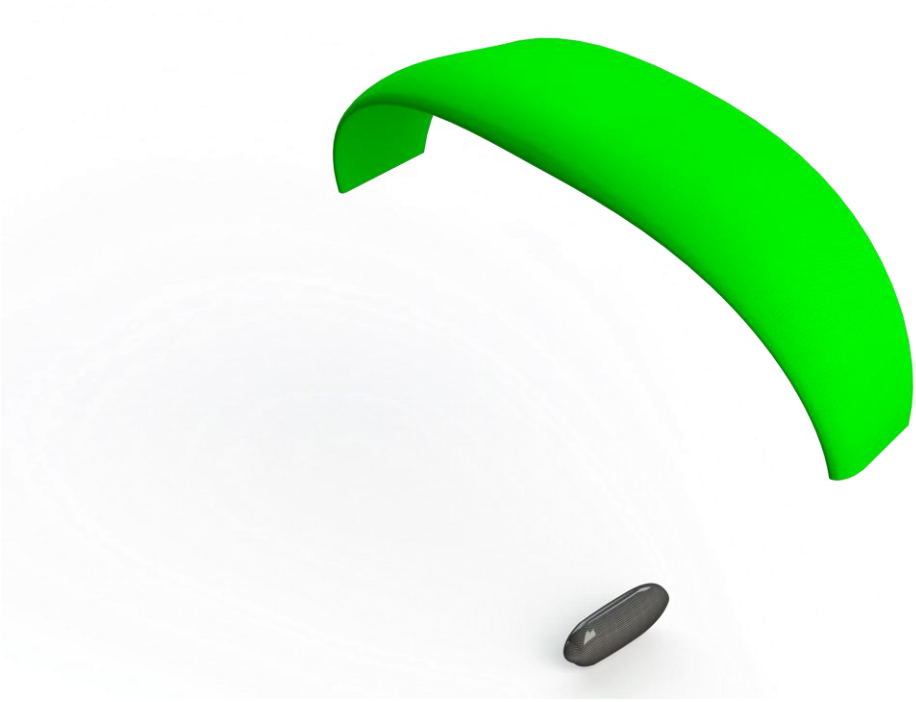

Figure 10 Final Parawing Aircraft Design

2.2.1 Parawing Geometry

The geometry of our parawing was dictated by size requirements for the payload as well as proven design characteristics from the Windtech Cargo. The dimensions listed in Table 4 below were either chosen or derived with these two factors in mind.

Table 4 Parawing Dimensions

Variable	Value	Variable	Value
m_0	400 kg	W_0	3924 N
S_w	60.753 m^2	$S_{w_{proj}}$	51.089 m^2
b_w	17.188 m^2	$b_{w_{proj}}$	13.746 m

$\bar{c}_w$	3.635 m	$c_{w_{root}}$	4.2 m
h_{ac}	0.25	h_{cm}	0.15
AR_w	4.863	e	0.9052
TR_w	0.5252	λ_w	0 deg

Most of these values were chosen during the design process in order to meet the lift and moment requirements for our parawing aircraft and were based on an XFLR5 model of the Windtech Cargo. However, the value of e was calculated using equation 2 above.

2.3 Hang Glider Aircraft Design

In addition to the two full scale designs created above a small-scale hang glider design was created for flight purposes. The hang glider aircraft was based upon the North Wing Pacer 13 GT hang glider and ultralight trike [42]. A V-tail was also added to the design of the hang glider aircraft to allow for easier directional control. The scale of the aircraft was chosen based on the design of previous small-scale MQP aircraft as the flight tests were planned to take place at the same location as the previous MQP [43], [44] .

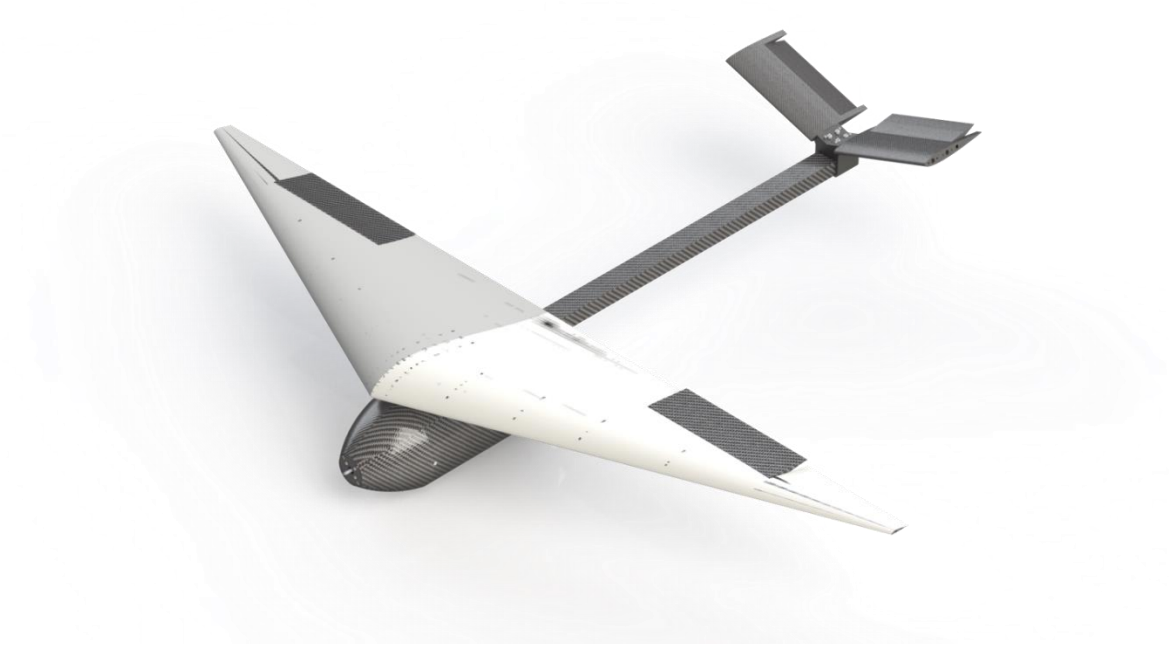

Figure 11 Final Small-Scale Hang Glider Aircraft Design

2.3.1 Hang Glider Geometry

The geometry of our hang glider was dictated by size requirements for the small-scale payload as well as proven design characteristics from the North Wing Pacer 13 GT. The dimensions listed in Table 5 below were either chosen or derived with these two factors in mind.

Table 5 Hang Glider Dimensions

Variable	Value	Variable	Value
m_0	3 kg	W_0	29.43 N
S_w	0.305 m^2	S_{vtail}	3.28 m^2
b_w	1.5 m	$\bar{c}_w$	0.249 m
$\bar{c}_{vtail}$	0.137 m	h_{ac}	0.25
h_{cm}	0.49	AR_w	7.37
AR_{vtail}	3	l_{LE}	1 m
$\bar{l}_{vtail}$	0.972	TR_w	0.1
TR_{vtail}	1	λ_w	18.418 deg
Γ_w	0 deg	Γ_{vtail}	19 deg
i_{vtail}	0 deg	ε_0	0
e	0.8285	$\bar{l}_{htv}$	0.0335
z_{vt}	0.5538	$\bar{V}_{vtail}$	0.63
$k_{\varepsilon,\alpha}$	0.1891		

Most of these values were chosen during the design process in order to meet the lift and moment requirements for our hang glider aircraft and were based on an XFLR5 model of the North Wing Pacer 13 GT. However, the values of e and $k_{\varepsilon,\alpha}$ were calculated using equations 2 and 6 above.

3 Design Process and Analysis

We used low-fidelity simulations in MATLAB to narrow down the selection of types of aircraft. From there, we selected various parameters for each type of aircraft to create a design. Finally, we simulated two aircrafts numerically with control and validated them and built the third aircraft.

3.1 Low Fidelity Design Elimination

We created a design space exploration to select which aircraft designs to pursue further. This design space was decomposed into two different processes. First, we chose to vary a total of five parameters to determine how the time, fuel, and range change with this variation. These parameters were: specific fuel consumption, fuel volume, power, planform area, and the ratio of payload mass to total mass. The effects of these parameters were analyzed based on a ranking system implemented in a low-fidelity particle model simulation that added weighted penalties to each variable of interest (i.e., time, fuel consumption, range). Second, we analyzed designs of different pre-existing aircrafts and applied the same ranking system to these designs in order to yield a smaller number of possible contenders when deciding which designs to pursue throughout this project.

The low-fidelity simulation for design space exploration began by listing flight scenarios to test different designs. The efficiency of a flight scenario was determined by how much distance the scenario could cover given set characteristics (including fuel weight). Three flight scenarios were chosen and used to determine the ranking of different designs.

3.1.1 Flight Scenario Selection

The first phase of the design space exploration was simulating different flight paths to find which ones were the most efficient. To this end, we developed a MATLAB-based simulation of an aircraft particle dynamical model (low-fidelity model).

We created ten different flight scenarios based on our discussions with our project sponsor and the overall project goals. These scenarios arose from combinations of two different launch conditions and two different flight paths. The launch types were ground launch and aerial launch. The two flight paths were steady level flight at a certain altitude and varying-altitude flight between two different altitudes. The ten flight scenarios all included an unpowered glide phase at the end. A ground take-off phase was characterized by having full power to climb until reaching a desired altitude. An aerial delivery phase was characterized by being dropped from an altitude, losing some altitude to simulate deployment, and then either gliding down to altitude or powering up to altitude. The choice of glide down or power up was made based on the current altitude and the desired altitude. If the current altitude was below the desired altitude, the simulation

ran a power up. If the current altitude was above the desired altitude, the code glid down to the desired altitude. A steady-state phase flew at a constant desired altitude. A varying altitude phase powered up to the higher altitude and then glid down to the lower altitude. Once at the lower altitude, it powered back up the higher altitude and then glid back down to the lower altitude. Nap-of-the-earth flight was defined as an altitude that is below radar. This altitude has been defined by the military as 60 meters above the ground or lower. These flight scenarios were:

- Ground Launch to Steady Level Flight: Nap-of-the-Earth (60 m)
- Ground Launch to Steady Level Flight: Medium Altitude (5,000 m)
- Ground Launch to Steady Level Flight: High Altitude (10,000 m)
- Ground Launch to Varying Altitude: Low to Medium Altitude (2,000 m to 5,000 m)
- Ground Launch to Varying Altitude: Medium to High Altitude (5,000 m to 10,000 m)
- Aerial Launch to Steady Level Flight: Nap-of-the-Earth (60 m)
- Aerial Launch to Steady Level Flight: Medium Altitude (5,000 m)
- Aerial Launch to Steady Level Flight: High Altitude (10,000 m)
- Aerial Launch to Varying Altitude: Low to Medium Altitude (2,000 m to 5,000 m)
- Aerial Launch to Varying Altitude: Medium to High Altitude (5,000 m to 10,000 m)

To simulate these scenarios, we developed the following 3-DOF particle model in MATLAB shown in Appendix 7.1 . The states being tracked were pitch angle, velocity, altitude, total weight, and horizontal position. During steady level flight, we assumed that the lift was equal to the weight acting in the vertical direction. This caused the rate at which the pitch angle changes to go to zero.

$$\dot{x} = \begin{bmatrix} \dot{\gamma} \\ \dot{V} \\ \dot{H} \\ \dot{W} \\ \dot{p}_x \end{bmatrix} = \begin{bmatrix} \frac{1}{mV}(T - D - Wsin(\gamma)) \\ \frac{1}{m}(T + L - Wcos(\gamma)) \\ Vsin(\gamma) \\ -c_t T \\ Vcos(\gamma) \end{bmatrix} \quad 7$$

In the beginning of steady-state we set the pitch angle to zero. Since the system was either ascending or descending, the pitch angle was non-zero. The steady state condition of lift equals weight forced the rate of γ to zero, which made the pitch angle become a constant at whatever value the pitch angle was when entering steady-state cruise. We made these assumptions to see what fuel burn at steady level flight was

and since the transition phase between launch condition and steady level flight would be negligible compared to a two-hour flight going approximately 1,000 km for overall performance.

From this simulation, we determined that the aerial delivery launches were more efficient than ground launches because the fuel expenditure for takeoff was avoided. Also, steady state flight at higher altitudes was more efficient than lower altitudes or varying altitudes since it took a considerable amount of power to climb to altitude compared to maintaining steady level flight.

Since our design requirements included ground launch as a priority, we chose to do two ground launch scenarios. These scenarios were steady-stat at higher altitudes and steady-state at Nap-of-the-Earth. Even though it the simulation showed that Nap-of-the-Earth was less efficient than higher altitudes, it was still flying comparable distance and has the added benefit of being at an altitude chosen to avoid hostile forces' radar. We wanted to be able to explore that as an option since the simulation proved it still was comparable distance even if slightly less efficient.

3.1.2 Design Ranking Weighted Equation

To explore the design space, we created a system to produce a rank based on output parameters. The three output parameters chosen were the total flight distance, the weight of remaining fuel, and the total mission time. These parameters were chosen because of their importance in evaluating the design performance of a design. The goal values which the outputs were compared with are 1000km for total distance, any value greater than 0 for weight of fuel, and 120 minutes for mission time. 1000km was chosen as the goal value for range because in project description for our project a range requirement of 200-500km was given, as a team we decided that 500km was a one-way flight to exhaustion and as such by doubling the number, we would be able to judge designs on their ability to return to base. The goal value was chosen to be greater than 0 kg for weight of fuel, because any design that can maintain fuel throughout the entire flight has the potential for landing to offload supplies as well as diverting to alternate landing zone on return. Finally, 120 minutes was chosen as the mission time goal as while mission time was not given in our requirements, we decided that if a system could deliver supplies in 2hrs it would be exceptional for emergency supply deliveries. We weighted the values accordingly with total distance being 50% of the score, weight of remaining fuel being 30% of the score, and mission time being 20% of the total score resulting in a score out of 100%.

$$Rank = 50\left(1 - \frac{10^6 - d}{10^6}\right) + 30\left(1 - \frac{(W_{fuel} - (W_{final} - (W_0 - W_{fuel})))}{W_{fuel}}\right) + 20(1 - \frac{(t - 120)}{600}) \qquad 8$$

A weight of 50% for distance was chosen because having a design that could make it to or exceed 1000km would give our design greater capabilities such as returning to base after resupplying. Weight of

fuel remaining was decided to be 2nd to the distance traveled but more important than the mission time because having a better fuel efficiency will improve the economics of a chosen design and as such was given a 30% weight. Finally, 20% weight was given to mission time because while delivering supplies in a timely manner is important, through talks with the U.S. Army Combat Capabilities Development Command we found that through scheduling and planning flight time can be accounted for. A distribution of 50-30-20 was chosen because of the relative importance of all categories chosen. We decided that distribution chosen gave the most importance to range while only giving slightly more importance to remaining fuel and keeping importance for mission time.

3.1.3 Design Space Exploration

The design space exploration was a continuation of what was done in section 3.1.1 and 3.1.2. However, instead of exploring different launch and cruise conditions, we explored the effect of aerodynamic parameters within the simulation. This was decomposed into two different processes.

The first process was to explore how different characteristics of flight affected our weighted equation of range, fuel burn, and time of flight. We chose the two simulations that both met the design requirements of the project and yielded the best results:

- Ground Launch to Steady Level Flight: Nap-of-the-Earth (60 m)
- Ground Launch to Steady Level Flight: Medium Altitude (5,000 m)

Within these two simulations, a total of 5 parameters were strategically varied (via "for" loops in MATLAB) based on previous research: the specific fuel consumption, fuel volume, power, planform area, and ratio if the payload mass to the total mass of the system. Table 6 below shows how each parameter was varied. For constancy purposes, when one parameter was varied, all the others were kept constant. The coefficients that were kept constant were pulled from two sources. The aerodynamic coefficients were from a parafoil simulated in [6]. Through simulation testing done over the ten different flight scenarios using the handful of engines selected based off initial specs the testing results revealed the Polini Thor 250 to be the most consistent across all flight scenarios [45]. This engine was chosen because it consistently produced enough thrust (without overpowering) to successfully complete the various missions tested before the design space exploration (i.e., testing different takeout and cruise conditions). The Polini Thor 250 has a maximum thrust of 1029 N with a fuel consumption of 2.9 liters/hour at 30kg of thrust, along with 36 hp at 8000 rpm.

Through simulation testing done over the ten different flight scenarios using the engines selected based on initial specifications, the Polini Thor 250 was chosen because it produced enough thrust to successfully complete the various missions tested while also being lightweight enough to not cause

detrimental effects to the aerodynamic characteristic of each aircraft [45]. The Polini Thor 250 has a maximum thrust of 1029 N with a fuel consumption of 2.9 liters/hour at 30kg of thrust, along with 36 hp at 8000 rpm.

Table 6 Design Space Exploration

Parameter	**Variation (initial value : step size : end value)**
Specific Fuel Consumption (N/W)	1E-7 : 5E-8 : 7E-7
Fuel Volume (Liters)	18.93 : 3.78 : 56.78 5:1:15 (Gallons)
Power (kW)	14.91 : 3.73 : 59.66 20:5:80 (HP)
Planform Area (m^2)	2 : 0.5 : 20
Payload Fraction (Mass of the payload to the total mass of the system)	0.33 : 0.037 : 1

The second process was to explore a set of pre-existing designs (with corresponding pre-existing aerodynamic parameters) and use our weighted equation to specifically rank them against each other. The same two simulations were used for each of these designs: ground launch to steady state at 60m and ground launch to steady state at 5000m. The Polini Thor 250 engine was again used in all the simulations. In total, a fixed wing, hang glider, two parawing designs, and the parafoil in [6] were also tested.

3.1.4 Obtaining Data for Design Space

To obtain our initial data for the design space exploration the team set about modeling the respective lifting surfaces for wach design in XFLR5. Standardized airfoils were taken from internet repositories and scaled to the desired size. Then a simulation was run to get the coefficients of lift and drag for the airfoil at different angle of attacks. For the analysis of the parafoil the team chose a gnuEasy Airfoil as it most closely resembled those seen on commercial parafoils. For fixed wing aircraft the team chose the NACA 4415 airfoil as it alligned with our desired performance characteristics.

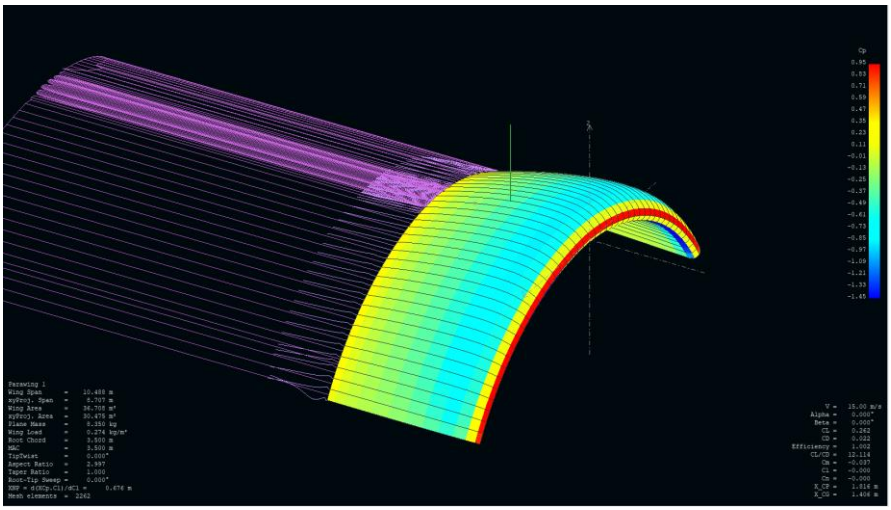

Figure 12 XFLR5 3D Analysis of gnuEasy Airfoil applied to a Parafoil Design

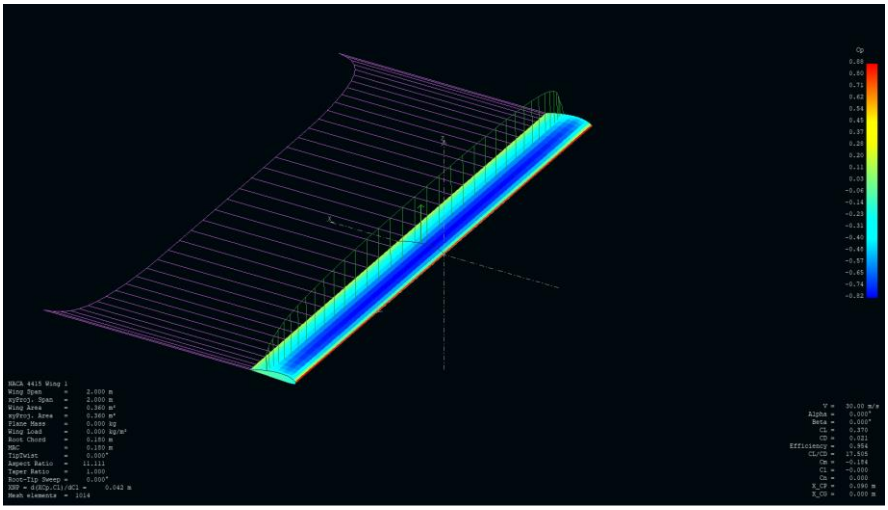

Figure 13 XFLR5 3D Analysis of NACA4415 Airfoil applied to a Fixed-Wing Design

For analysis and modeling of a hang glider the MH82 airfoil was used, applied to the dimensions of the Maverick 4 Trike Wing from NorthWing. One key observation from the data obtained by the analysis modeled in Figure 14 is that while the hang glider creates very stable response data, it is also only capable of stable flight for a small range of angle of attack, from about -3 degrees to 2.5 degrees.

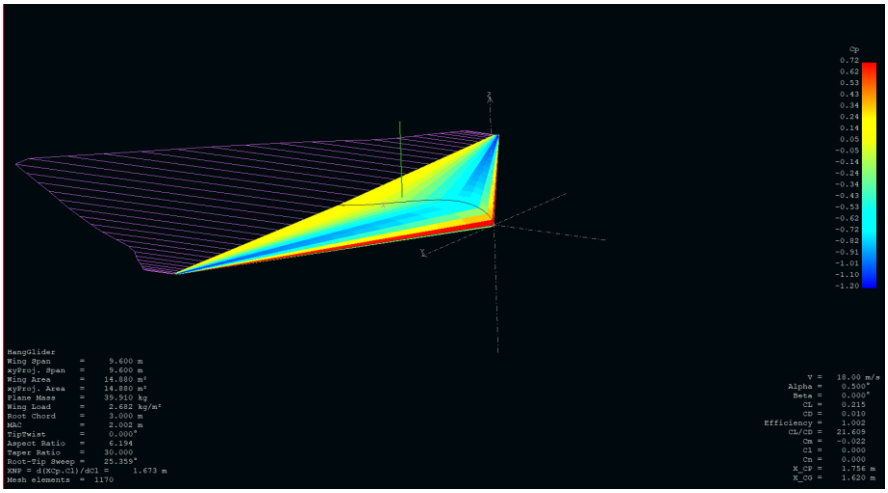

Figure 14 XFLR5 3D analysis of MH82 airfoil applied to Hang Glider Design

3.1.5 Design Ranking Results

The two processes described above produced ranks each time a simulation ran. For the first process, a trend of how each parameter affected the rank of the system was obtained and plotted. For the second process, different aerodynamic designs were run with the same engine to compare specific designs ranks. The aerodynamic coefficients used for this analysis were taken from [6], and although the performance trends presented in this section are paralleled in other aircraft designs, the exact numerical data in the following graphs and tables only applies to the wing geometry and coefficients associated with the parafoil from [6].

In the first parameter variation, specific fuel consumption was varied as shown in Table 6. The figure below shows that as specific fuel consumption increased, the rank decreased linearly. As more fuel is burned per second but no additional fuel is given, the system cannot fly as long, as far, or have additional fuel left over. Since these are the parameters that determine the weighted equation, it makes sense that the figure looks as it does.

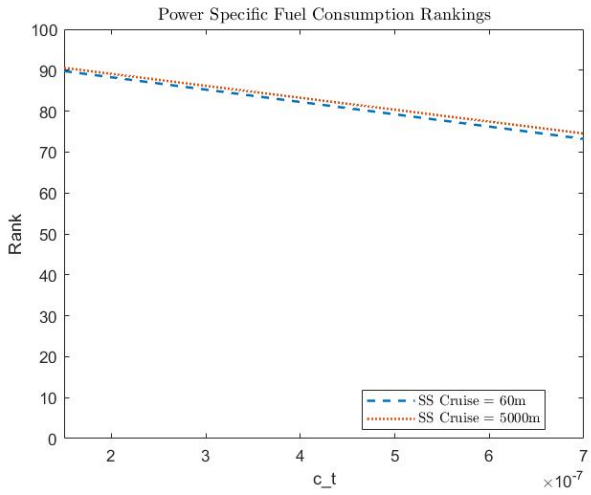

Figure 15 Power Specific Fuel Consumption Graph

In the second parameter variation, the volume of fuel was varied as shown in Table 6. Figure 16 shows that as the volume of fuel increases, the rank increases. The first few iterations saw a greater increase in rank than the later ones. There are diminishing returns to holding more fuel because at a certain point, the system is just holding more weight.

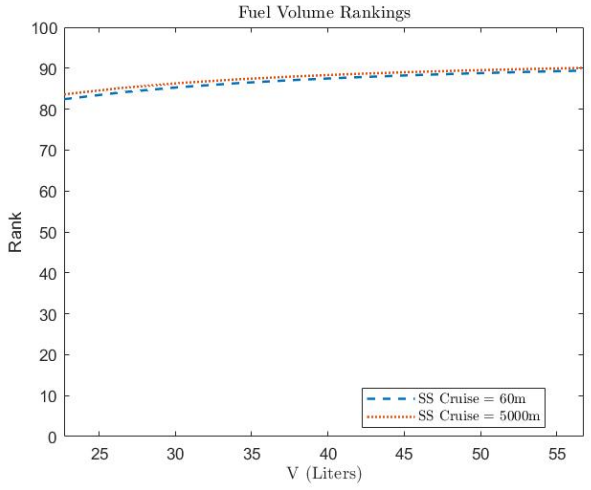

Figure 16 Fuel Volume Ranking Graph

In the third parameter variation, the power was varied as shown in Table 6. Figure 17 below shows that there is a certain power threshold. Above this threshold, the ranks significantly dropped. This upper power threshold is when the system has too much power. Any engine with this power causes the simulation to increase the pitch angle far above appropriate levels and fails due to a lack of a pitch controller.

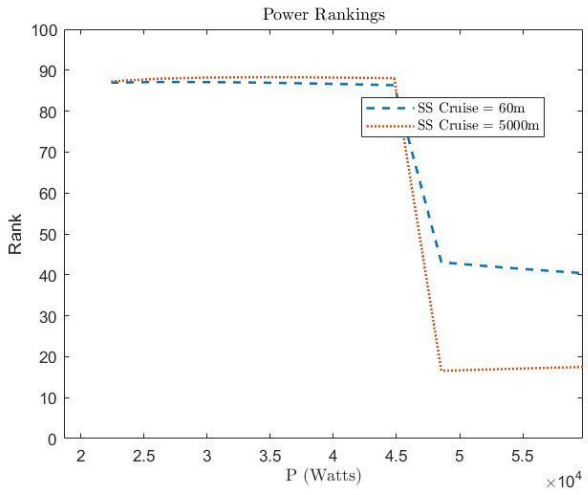

Figure 17 Power Ranking Graph

The fourth and fifth parameter variations, the planform area and mass payload to total weight fraction, are linked. They vary as shown above in Table 6. As planform area increases, the rank is not significantly impacted and as the mass fraction increases, the rank increases to a certain point before leveling off. Below are the figures showing these trends but there are certain ranges on each figure where the simulation failed, and the rank is 0. This is assumed to be due to either a lack of lift or adverse effects from having too much power for stable flight. We learned that if the planform area is too small for the mass it is carrying, the system cannot fly and falls to the ground. We also learned that if the wing loading is too small, there is too much lift, and the 3-DOF model we are using for this simulation fails due to a massive increase in pitch angle, above what is realistic. The pitch angle, in radians, would increase to values orders of magnitude bigger than reasonable values.

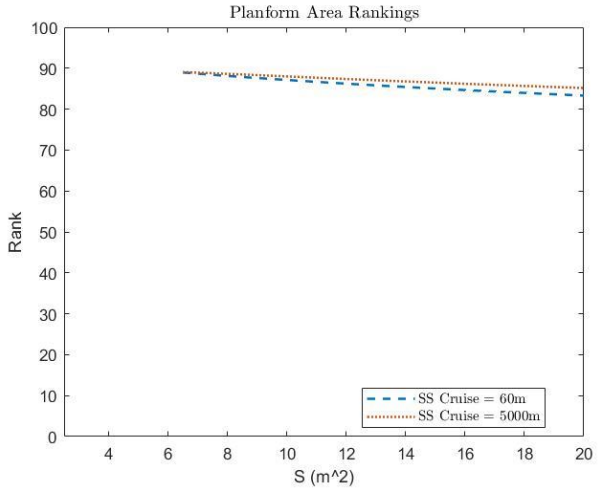

Figure 18 Planform Area Ranking Graph

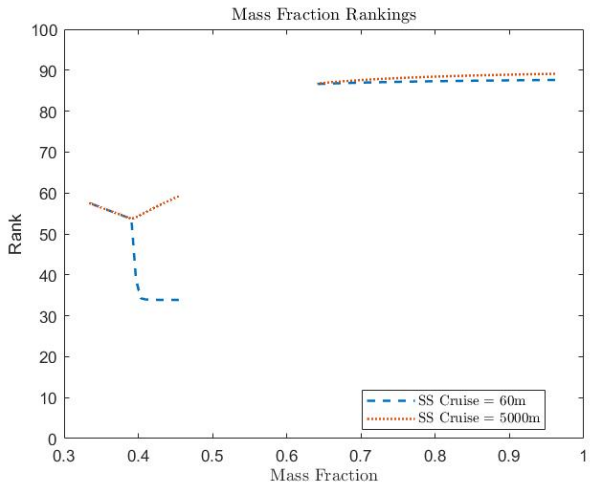

Figure 19 Payload Mass Fraction Ranking Graph

After we varied the different parameters, we tested different aerodynamic characteristics based on different types of aircraft. All aircraft were simulated using the Polini Thor 250 engine. The Polini Thor 250 The specifications for all tested engines can be found in 7.2 Engine Spec Sheet. Below in Table 7 we ranked the different designs based on the same simulation we used above. From this the fixed wing and Hang glider designs performed the best.

Table 7 Design Space Exploration: Aerodynamic Design Ranks

Design	**Rank at Ground-Nap**	**Rank at Ground-5,000**
Fixed Wing	86.5797	88.1318
Hang glider	85.6907	87.2489
Parawing 1*	85.4708	85.9065
Parawing 2*	79.8112	80.7836
Parafoil (Yakimenko)	67.2416	67.5953

*Due to the size of the planform area, this simulation was run with a 500 kg payload instead of 250 kg

The two parawing designs we used had over double the planform area than the other designs. When we ran the simulation with the normal payload, the parawings failed in the simulation due to the instability with mass to planform area at certain ranges mentioned earlier. To correct this we ran the parawing simulations with a 500 kg payload instead of 250 kg. The simulation then ran successfully. One small caveat of the simulation is that it is acting like a particle and not taking into effect the limitations of the designs. Both

parawing designs fail aerodynamically when above 25 m/s in XFLR5 while the simulation pushes their speed to approximately 55 m/s. This inaccuracy can only be corrected on a higher fidelity model that takes into effect the designs aerodynamic characteristics and treats the system as more than a point mass. Therefore, we chose two designs to pursue medium fidelity models, and one design to build at a smaller scale. The fixed wing and parawing designs were chosen for simulation because they were drastically different in terms of shape and concept, and the hang glider was chosen to build because it resembles a combination of the fixed wing and parawing designs.

3.2 Fixed Wing Design

With the low fidelity simulations complete the next step was to begin designing the aircraft. While multiple aircraft were designed, the first one designed was the fixed wing system. This was completed first as it was the area the project team had the most experience in. This enabled the design to be evaluated while the other two designs were being created. The following sections detail the fixed wing design process.

3.2.1 Initial Fixed Wing Sizing

The first part of designing our fixed wing aircraft was to set the total weight of the system. This was done by evaluating the weight payload fraction of other similar UAV aircraft such as the Hermes 450 and Hermes 900. The evaluation of these systems led the team to set the weight payload fraction at 1/3, which gave the aircraft a total weight of 680.39 kg [46], [47]. After that was decided, the next step was to determine the aspect ratio for the wing. This was done using historical data found in *Aircraft Design*, which led the team to select an aspect ratio of 6.6 [48]. Once the aspect ratio was chosen, the team selected a planform area of $15m^2$, which was done using the deign space exploration performed in section 3.1.4. This was chosen as it is approximately the same as similar sized aircraft, such as the Hermes 450, while still preforming well in our evaluations [46]. While the smaller planform areas received higher scores, they likely would not have been large enough to lift the entire load of the aircraft. With the planform area, aspect ratio, and total weight chosen, the flight velocity and altitude needed to be decided. For the flight velocity, 60 m/s was chosen as it was similar to the typical cruising speed of other similarly sized aircraft with comparable ranges, such as the Piper Arrow [49]. The altitude of 5000m was chosen as it was the altitude which produced higher scores in almost all of the design space explorations described in section 3.1.4.

With the initial parameters for the aircraft chosen, the next step was to select the airfoil. To do this, equation 3 below was used. This equation described the required coefficient of lift for the airfoil given the parameters chosen above. Equation 10 is shown below and was used to solve equation 9.

$$C_{L_{req}} = \frac{W}{q_c(S_w)}\left(1 + \frac{2}{AR_w}\right) \quad 9$$

$$q_c = \frac{1}{2}\rho_c V_c^2 \quad 10$$

This led to a required lift coefficient of 0.4374. To accomplish this, a NACA 2412 airfoil was chosen. The NACA 2412 was chosen because it is a widely used, low drag airfoil that at low incidence angles could accomplish the required lift. This is demonstrated in the graph below.

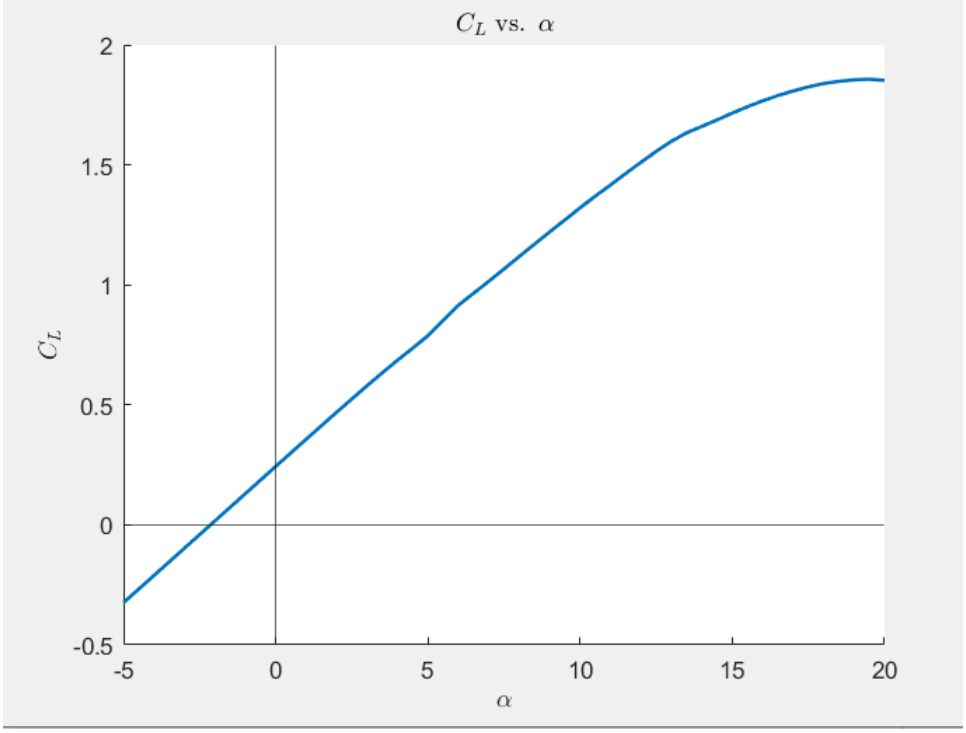

Figure 20 Lift Coefficient as a Function of AoA for NACA 2412 airfoil

With the airfoil established, the team began to determine the wingspan and chord length of the aircraft. This was done using equations 11 and 12 below. In the equations, b represents wingspan while C represents the chord length.

$$b_w = \sqrt{S_w(AR_w)} \quad 11$$

$$c_w = \frac{b_w}{AR_w} \quad 12$$

These equations led to a wingspan of 10 m and a chord length of 1.5 m. With the wing designed, the next step was to design the tail. Because the wing generated enough lift for the entire aircraft, the tail was chosen to be symmetric. This is a very standard practice as using an airfoil that creates large amounts of lift in the tail produces a large moment due to the large moment arm between the center of lift of the tail and the center of gravity of the aircraft. This led to the selection of the NACA 0012 airfoil.

With the airfoil for the tail selected, the next step was to size the tail. To do this, the distance of the leading edge of the tail from the leading edge of the wing was set. This was chosen to be 5 m based on historical data from aircraft such as the Hermes 450 [46]. The same distance for both the horizontal tail and vertical tail was selected. Equations 13 and 14 below show how the planform area for both the horizontal and vertical tails were selected. The coefficient of volume for each tail was selected using historical data provided in *Aircraft Design* [48]. The values ended up being 3.166 m^2 for the horizontal tail and 1.194 m^2 for the vertical tail.

$$S_{HT} = c_{HT}(S_w)\frac{c_w}{\bar{L}_{HT}} \tag{13}$$

$$S_{VT} = c_{VT}(S_w)\frac{b_w}{\bar{L}_{VT}} \tag{14}$$

With the planform area chosen, historical data presented in *Aircraft Design* was used to select the aspect ratio for each tail [48]. The horizontal tail was selected to have an aspect ratio of 3 and the vertical tail was selected to have an aspect ratio of 1.3. Using equations 11 and 12, but with the values for the tail instead of the wing, the horizontal tail was determined to have a span of 3.08 m and a chord of 1.03 m. The vertical tail was determined to have a span of 1.25 m and a chord of 0.96 m.

To determine the center of gravity of the aircraft and the required incidence angle for the tail and wing, the aircraft was modeled in XFLR5 as shown below.

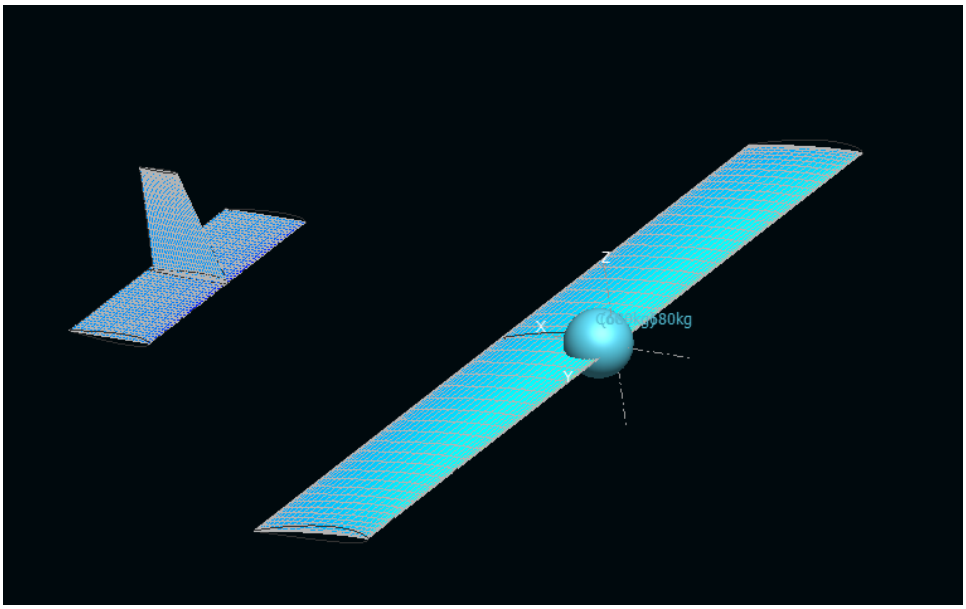

Figure 21 Fixed-Wing Wing and Tail configuration in XFLR5

The first step in XFLR5 was to determine the incidence angle of the wing. This was done by running a simulation at the flight conditions defined earlier in this section and increasing the incidence angle of the wing until the required lift was generated. This process determined the incidence angle of the wing to be 5°. The next step was to determine the center of mass for the aircraft. To do this, an incidence angle for the tail needed to be chosen. 0° was chosen as the tail incidence angle to minimize the drag on the aircraft as enough lift was being generated by the wing alone. Multiple simulations were run to determine if adding lift from the tail and lessening the incidence angle of the wing would increase the lift to drag ratio of the aircraft, but the best ratio was found with a tail incidence angle of 0°. The weight of the aircraft was represented by a singular point mass to determine the center of mass. The center of mass was determined as the location for the point mass at which there was no pitching moment when at 0° angle of attack. This condition was chosen as the aircraft would cruise at 0° angle of attack. The center of gravity was determined to be 0.217 m behind the leading edge of the wing. While determining the center of gravity, it was also determined that the aircraft was statically stable as the pitching moment vs. angle of attack graph had a negative slope as shown in the Figure 22.

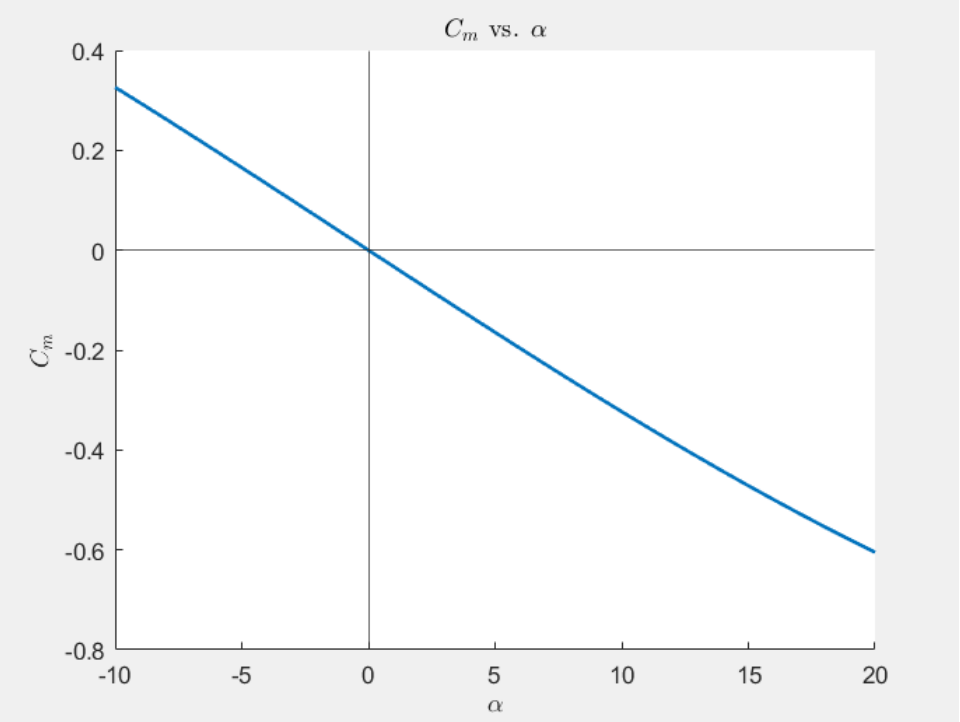

Figure 22 Moment coefficient as a function of AoA for the Fixed Wing and Tail system

3.2.2 Fuselage Design

The fixed wing fuselage design began by drawing a two-dimensional model of the payload with dimensions 129.54 cm long by 76.2cm tall on the Right Plane of a SOLIDWORKS Part file. Next a lengthwise 2-dimensional sketch of the fuselage outline was constructed using the spline tool. It is important to note that the spline angles should not exceed 90 degrees from their respective horizontals as this will cause a future step to fail. Next, ensuring there was room in front of the payload for an engine to fit, as well as adding a spar lengthwise along the inside top of the fuselage outline was important before adding any features. Selecting the vertical lines that serve as the beginning and the end of both the fuselage itself and the cargo bay, reference planes were added at these locations. On the planes at the beginning and end of the fuselage circles were added to serve as the opening for the propeller and the exit for the spar. Ovals were added to the two middle reference planes with the major axis vertical. The semi-minor axis was set to a value of 0.5 m to ensure there was room for the .53 m width of the payload as well as leave room to add ribbing for support later. A lofted-thin extrude was next used produce the shell of the fuselage and as shown in Figure 23 below.

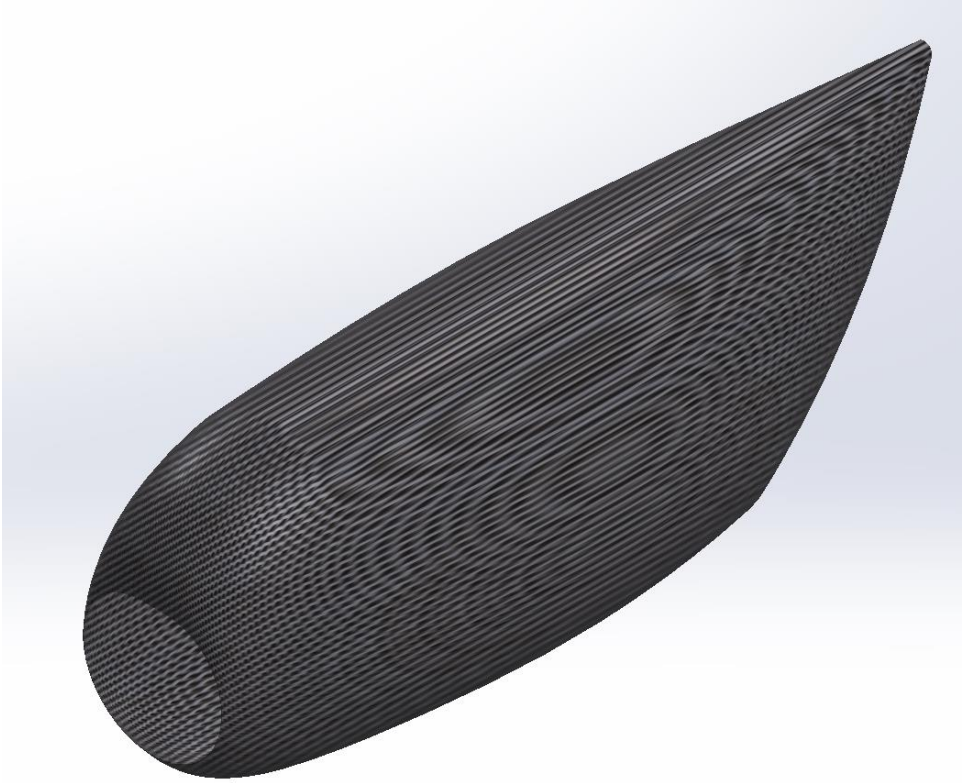

Figure 23 Fixed-Wing Fuselage outer shell

Following the lofted thin a vertical cut along the middle lengthwise was used to half and open the interior of the lofted-thin. On the Right Plane a new sketch was created, and the upper and lower edges of the body were converted into the new sketch using the converted entities tool. Lines were drawn from upper edge to lower edge equidistant from each other and then thin-extruded up to the rest of the body. Producing the following ribbing.

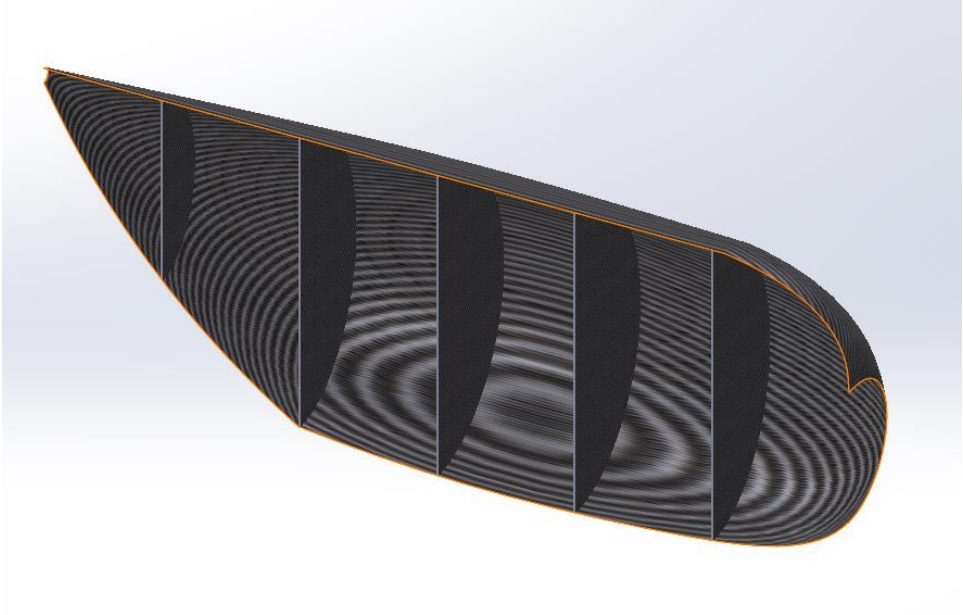

Figure 24 Fixed Wing Fuselage Ribbing

Lastly the spar drawn in the original sketch was extruded and then the entire body was mirrored to produce the final fuselage.

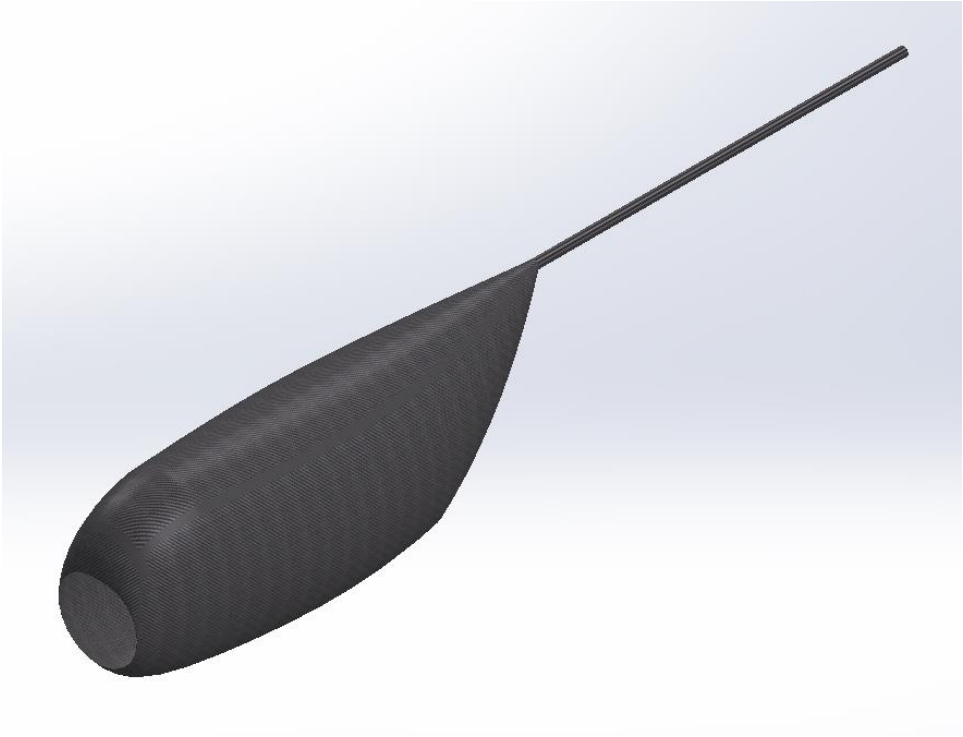

Figure 25 Final Fixed-Wing Fuselage with extended spar for mounting tail

When structural, thermal, and aerodynamic analysis begin the structure, and especially the ribbing will likely change to reflect discovery of structural weak points, or unnecessary material. Additionally,

working doors will be added to allow for those same analysis to be conducted with the cargo bay doors open as would occur when offloading the payload. Additionally, weight may need to be shifted throughout the fuselage in order to get the payload close to center of gravity (CG) as possible, so offloading payload has minimal effect on the stability of the aircraft.

3.2.3 Fixed Wing and Tail Plane Design

Given the calculated values in section 3.2.1, the wing was designed in SOLIDWORKS. First the data points for the NACA 2412 and 0012 were acquired from an online resource. Next the points were brought in to an Excel spreadsheet where they were multiplied by the required chord length and transformed such that the origin point would be at the half the chord length. The points were then saved as a text file and imported into SOLIDWORKS. The resultant points formed the airfoil curve which was extruded into 3D to form the basic shape of the wing. Individual ribs were created and an initial I beam spar were modeled to act as the internal structure of the wing. Afterwards cutouts were made in the wing skin and attachment points for the control surfacers were added. Finally, the ailerons were modeled and mated into place in the assembly. Once all parts were modeled, material properties were assigned to give accurate mass estimates of the wing assembly.

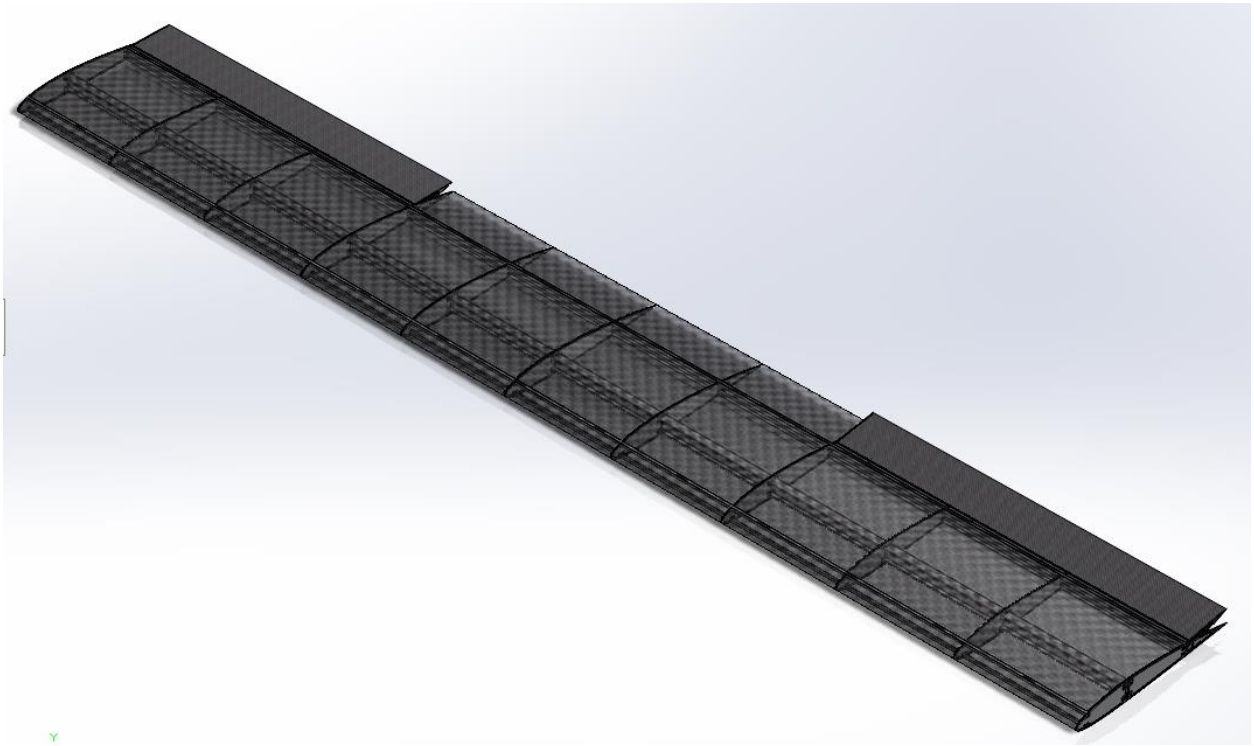

Figure 26 Wing of Fixed-Wing Configuration

The outer skin of the wing is constructed of a .635mm thick carbon fiber sheet. While thin the skin of the airfoil is mainly acting as the aerodynamic surface of the wing while the spar and ribs take the forces

involved. The ribs of the wing are made from 5.08mm carbon fiber plates to provide necessary ridged while remaining lightweight. Finally, the main spar and secondary spars are constructed from 6061 T6 Aluminum for its ridged properties and availability. Current material and thickness choices are preliminary and are subject to change post structural analysis.

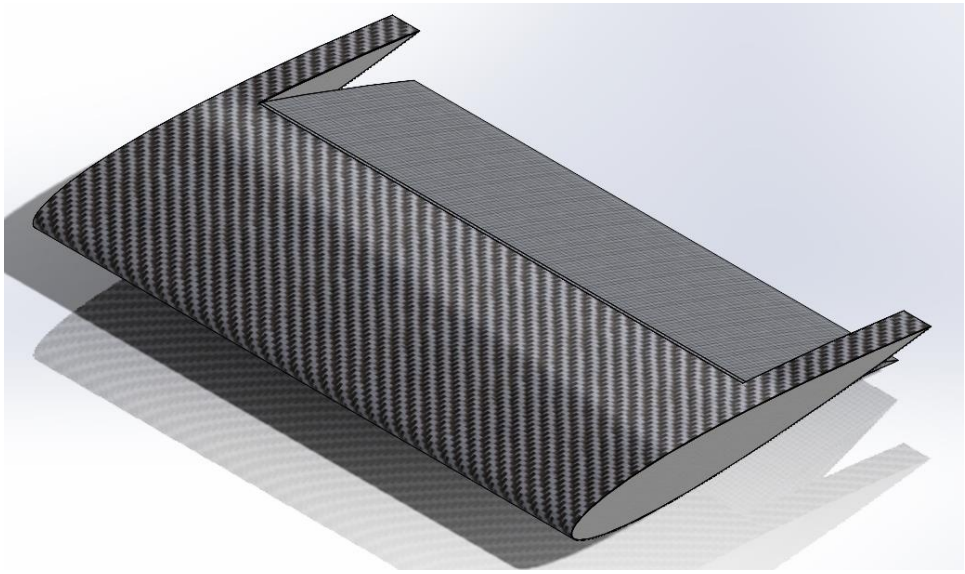

Figure 27 Fixed Wing Horizontal Tail

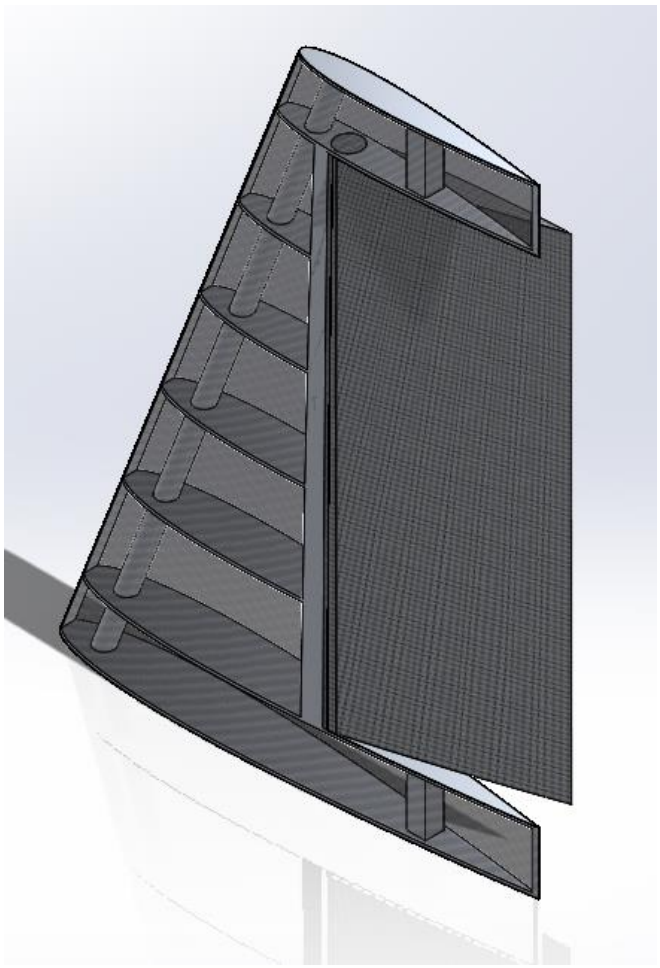

Figure 28 Fixed Wing Vertical Tail

The tail plane was modeled next using the same process for importing and sizing the NACA 0012 airfoil. The internal structure was model and the using the same rib and spar structure as on the wing and the same process was used to model the control surfaces. The vertical tail and horizontal tail use the same material choices as the wing because of their similar performance requirements.

3.2.4 Fixed Wing Assembly

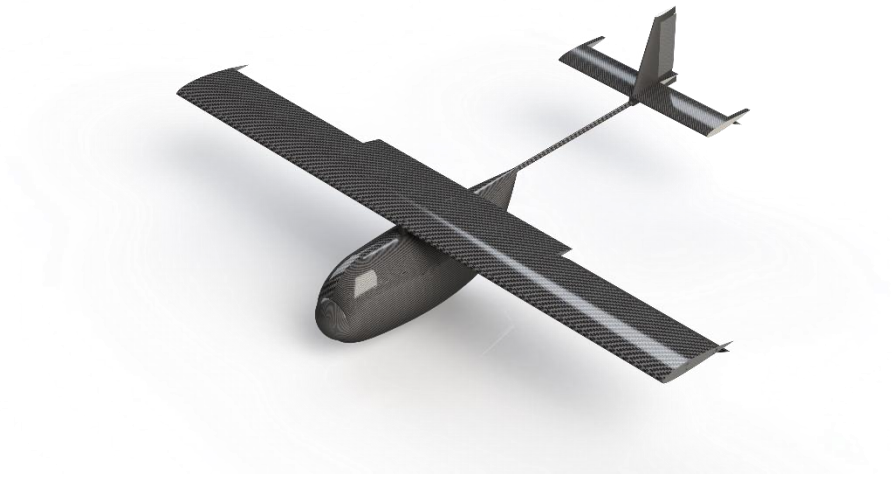

Figure 29 Fixed Wing Assembly

Using SOLIDWORKS the subassemblies were brought together into a final model. Using the base planes and a variety of mates each part was assembled. In order to place the wing in the correct place the mass function was used to create a center of mass point and the wings leading edge plane was mated the correct distance from it. Finally, interface parts were created to create a bridge from the tail plane and main wing spar to the main fuselage spar. The resultant assembly was then evaluated for mass to confirm that our dry mass was within the required amount.

Table 8 Fixed-Wing Mass Breakdown

	Individual Mass (kg)	**Quantity**	**Total (kg)**
Wing	184.47	1	184.47
Vertical Tail	47.26	1	47.26
Horizontal Tail	73.32	2	146.64
Fuselage	223.84	1	223.84
Engine	100	1	100
Payload	250	1	250
Total Dry Mass			729.29

Fuel	270.71	1	270.71
Total Wet Mass			1000

3.2.5 Fixed Wing Geometry Verification

With the fixed wing assembly complete, the team had a much better estimate of the aircraft's weight. The next step in the design process was to verify that our aircraft would generate enough lift at cruise with this new weight. To do this, the lift value of the aircraft was calculated for the cruise conditions of 60 m/s at 5000 m using equation 15 below. The coefficient of lift was taken from the XFLR5 data and plugged into the equation below. This showed that our aircraft generated 10,140 N of lift which meant it could lift 1,034 kg. This meant that the aircraft did not need to be redesigned due to aerodynamic requirements as the current configuration generated enough lift during cruise.

$$L = \frac{1}{2}\rho V^2 S C_L \qquad 15$$

With a CAD model for the aircraft created, and no redesign required based on the weight of the model, the next step was to ensure that no redesign needed to take place because of the fluid dynamics of the aircraft. This was done by evaluating the aircraft we had created in the Computational Fluid Dynamics (CFD) Software ANSYS Fluent. The procedure described in section 3.5.1 was used to ensure that the aircraft would be capable of flying in its current configuration. The results from those Fluent analyses did confirm that our aircraft did not need to be redesigned for it to be capable of the type of flight that it was designed to do.

3.2.6 Fixed Wing Structural Redesign

Structural analysis focused on ensuring the structural stability of the main wing. This required a redesign of the structural support components of the wing. More detail will be included in section 3.6.

3.2.7 Engine Selection for Fixed Wing

The first step in determining the engine for the fixed wing aircraft was to determine the power required for takeoff and cruise. The first step in determining the required power was to determine the weights at the different stages of flight; the weight for takeoff would be the initial weight of the aircraft, which weighed 9,810 N. To find the weight for cruise, the estimates provided in *Aircraft Design* were used. These state that total weight decreases by 3% for warmup and takeoff, and by an additional 1.15% for climb to cruise altitude [48]. This weight decrease accounts for the fuel burn during these two legs of the flight.

This led to the aircraft having an initial cruise weight of 9,373 N. The power required for cruise was calculated first as shown below in equations 16-19.

$$e = 1.78(1 - 0.045AR_w^{0.68}) - 0.64 \quad (16)$$

$$\frac{T}{W_c} = \frac{q_c C_{D_0}}{W_c/S_w} - \frac{W_c/S_w}{\pi AR_w e q_c} \quad (17)$$

$$\frac{P}{W_c} = \frac{T}{W_c}\left(\frac{V_c}{\eta_p}\right) \quad (18)$$

$$P_c = \frac{\frac{P}{W_c} W_c}{1000} \quad (19)$$

This led to the required cruise power being 25.96 kW. Once the cruise power was calculated, the takeoff power needed to be calculated. The calculation needed to be performed in imperial units due to the constants provided in *Aircraft Design* being provided in imperial units; these were later converted to metric units. This led to the required takeoff power being 117.8 kW as calculated below in equations 20 and 21 using α=0.025 and C=0.22.

$$\frac{P}{W_{TO}} = \alpha V_{max}^C \quad (20)$$

$$P_{TO} = \frac{P}{W_{TO}}(W_0)(0.7457) \quad (21)$$

As the power required for takeoff was significantly more than that required for cruise, that value was used as our baseline for engine selection. As takeoff typically occurs at maximum power, the selected engine was designed to have slightly more power production than our required takeoff power. This led us to selecting the UL Power UL390is engine which produces 119.3 kW of power [50][51].

3.3 Parawing Design

Once the fixed wing was designed, the team began to design the parawing system. Completing this system before the hang glider ensured it could be analyzed while the hang glider was being built.

3.3.1 Parawing Sizing

Similar to the first step in the fixed wing sizing, the total weight of the system needed to be determined first. This was done by building up the weight accounting for the weight of the payload, approximate weight of the parawing based on previous systems, approximate weight of paramotor engines, approximate weight of fuel, and approximate weight of the cargo body. This led to a total weight of 400 kg as the team's estimate.

After the weight was determined, the airfoil needed to be chosen. The NASA/Langley LS(1)-0417 was originally chosen because it is the current standard airfoil for many flexible lifting bodies [41]. When performing the simulations described in the next step, however, this airfoil could not be used. The shape of the NASA/Langley LS(1)-0417 airfoil makes it incompatible with XFLR5 software as certain regions exceed the local speeds XFLR5 allows. Because of this, for the XFLR5 simulations, the NACA-2617 was used. This airfoil is similar to the NASA/Langley LS(1)-0417 in thickness, camber, and location of maximum camber making it the ideal replacement for the NASA/Langley LS(1)-0417. The NACA-2617 does produce less lift than the NASA/Langley LS(1)-0417 but this helps to account for the inability of adding cutouts to the wing for the parafoil opening in XFLR5. These cutouts, used to inflate the wing, reduce the lift of the wing, resulting in lower lift which the NACA-2617 simulates.

With the airfoil chosen, it was time to design the wing. The wing was based around the Windtech Cargo paraglider. The Cargo is a tandem paraglider that when equipped with a motor is capable of lifting 360 kg [41]. It is also a paraglider which has several varied sizes, allowing us to produce our larger paraglider based on how Windtech scaled their various Cargo paragliders. All three models of the Windtech paraglider were created in XFLR5 as shown below using the NACA-2617 airfoil as mentioned above.

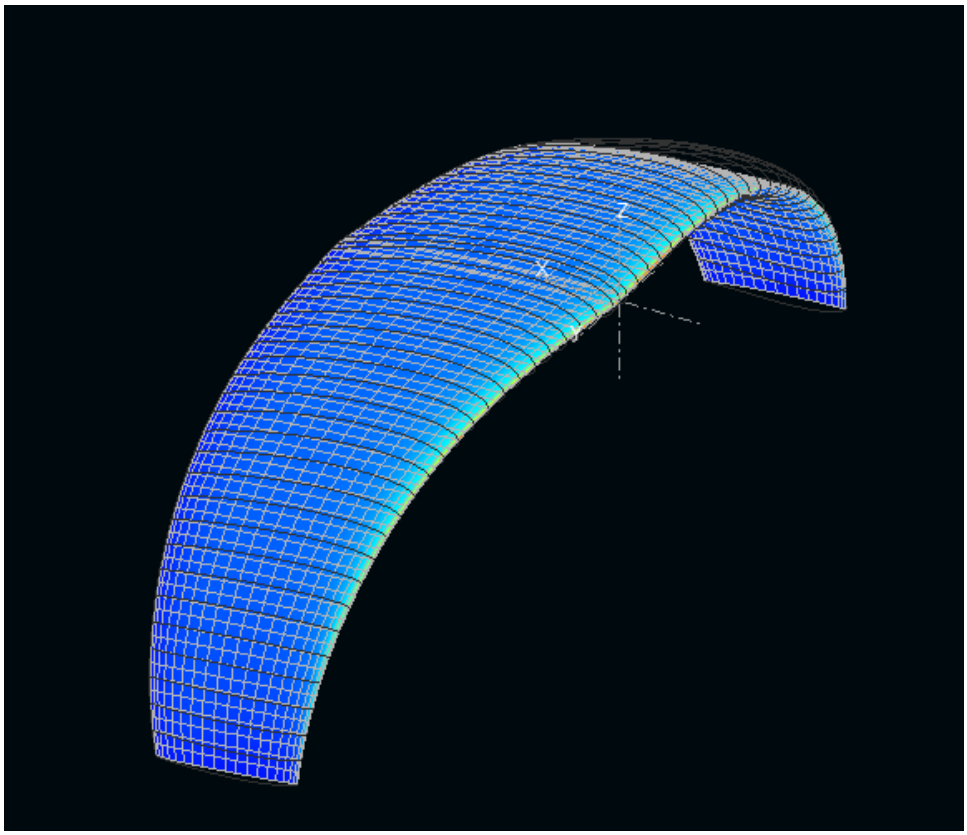

Figure 30 NACA 2617 parawing in XFLR5

All three paragliders were run through the same simulation at 20 m/s, the desired cruise speed of our parawing system, which allowed the coefficient of lift at various angles of attack to be calculated as shown in the table below.

Table 9 Lift Coefficient as a function of AoA

Angle of Attack	**Coefficient of Lift**
-2°	0.058
-1°	0.126
0°	0.195
1°	0.263
2°	0.331
3°	0.399

4°	0.466
5°	0.533

From this, the required projected surface area for each angle of attack was calculated using equation 22 below, where lift was set equal to the weight of the system as is standard for cruise condition resulting in the table below.

$$S_{W_{proj}} = \frac{2L}{C_L \rho_c V_c^2} \quad 22$$

Table 10 Projected Planform Area as a function of AoA

Angle of Attack	Projected Planform Area
-2°	549.4 m^2
-1°	211.5 m^2
0°	136.6 m^2
1°	101.3 m^2
2°	80.5 m^2
3°	66.8 m^2
4°	57.2 m^2
5°	50.0 m^2

Due to the significant reduction in size generated from higher angles of attack, 5° was chosen to be the flight angle for the parawing system. This still produced a high lift to drag ratio of approximately 30 before the payload body was added, making it a viable option. Once we had the projected surface area of the system, we were able to approximate the values of the other dimensions based on the way

Windtech scaled their paragliders, which was linear for all categories. This process is shown in the table below.

Table 11 Parawing Sizing Process

Value	Cargo 36	Cargo 39	Cargo 43	Size increase for each step	Number of step increases	Size for team parawing
Projected area (m^2)	33.84	35.72	37.61	1.9	6.5	50.0
Wing area (m^2)	35.12	39.13	43.66	3.75	6.5	68.03
Projected span (m)	10.8	11.4	12.01	0.6	6.5	15.91
Wingspan (m)	13.53	14.28	15.03	0.8	6.5	20.23
Projected Aspect Ratio	3.8	3.8	3.8	0	6.5	3.8
Aspect Ratio	5.2	5.2	5.2	0	6.5	5.2
# of cells	51	51	51	0	6.5	51
Max Chord (m)	3.23	3.41	3.59	0.18	6.5	4.76
Canopy weight (kg)	9.9	10.6	11.2	0.6	6.5	15.1

3.3.2 Parawing Fuselage Design

The design of the parawing fuselage was very similar to the design process outlined for the fixed wing in section 3.2.2, essentially following along the same path. The first main difference in this design compared to the fixed wing was there being no tail. With no tail being required for the parawing fuselage design configuration, no spar had to be incorporated. Secondly, the parawing is under tighter weight constraints based on the amount of lift it can produce. What this did was it forced the design to be more stringent regarding the shape of the fuselage. Thirdly the engine is located behind the payload in this configuration as a push prop is being used, requiring for more open space to be placed toward the back of the fuselage. Thus, a revolved extrude was required to produce a nose cone. Due to the parawing design calling for a push prop, it was decided upon to go with a sharper nose to the fuselage for aerodynamical purposed. The previous process combined with these changes produced the following weighing approximately 53 kg.

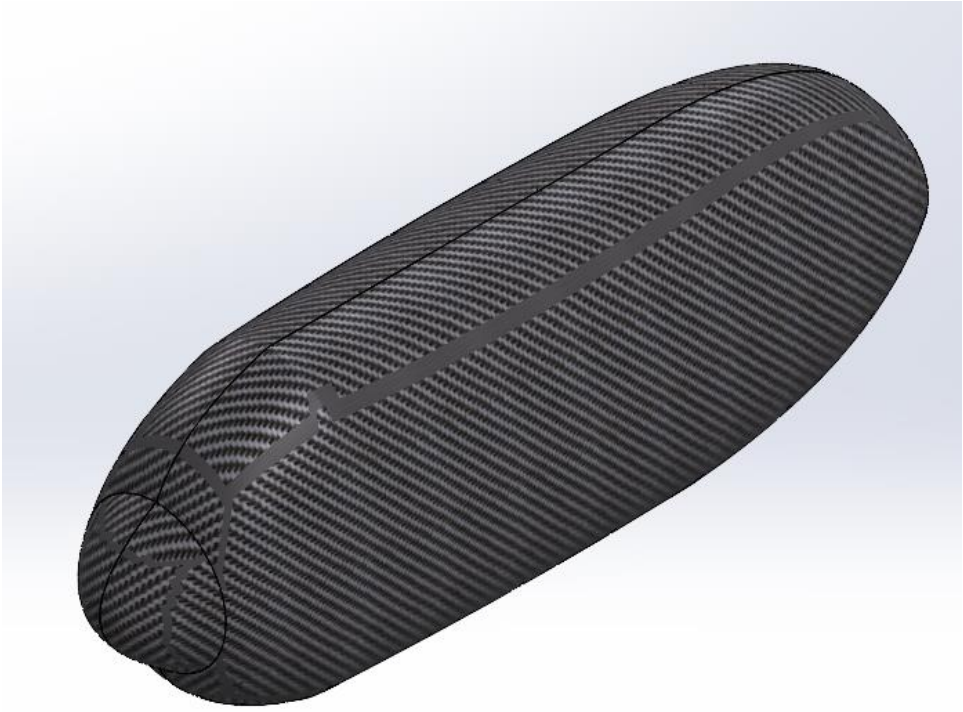

Figure 31 Parawing Fuselage

3.3.3 Parawing Redesign

After more research was conducted it was determined that parawings tend to have much lower stall angle of attacks due to their open faces when compared to the closed nose version of the wing [52]. This meant that the lifting capabilities of the NASA/Langley LS(1)-0417 airfoil were not sufficient as the wing

needed an incidence angle of 5° to get the lift required. Other parawings have been tested and found to have stall angle of attacks of approximately 7°. Because the Wing was originally designed for cruise this small margin between incidence angle and stall angle of attack meant that the airfoil likely would not be able generate the lift needed for climb.

As a result of the higher lift requirements m modified version of the Clark Y airfoil with a flat bottom was chosen to replace the NASA/Langley LS(1)-0417 airfoil. This airfoil was chosen due in part to it already being used by DEVCOM SC [52]. In addition to already being used by the DEVCOM SC Modified Clark Y is a very high lift but simply shaped airfoil meaning it will require a lower incidence angle of the wing lift the same weight. The simpler shape will make manufacturing easier as well.

Once the new airfoil had been chosen the wing originally designed for the NASA/Langley LS(1)-0417 was converted to being used with the Modified Clark Y airfoil. All of the other dimensions of the wing remained the same the only difference was the airfoil that was used. This new wing is shown below.

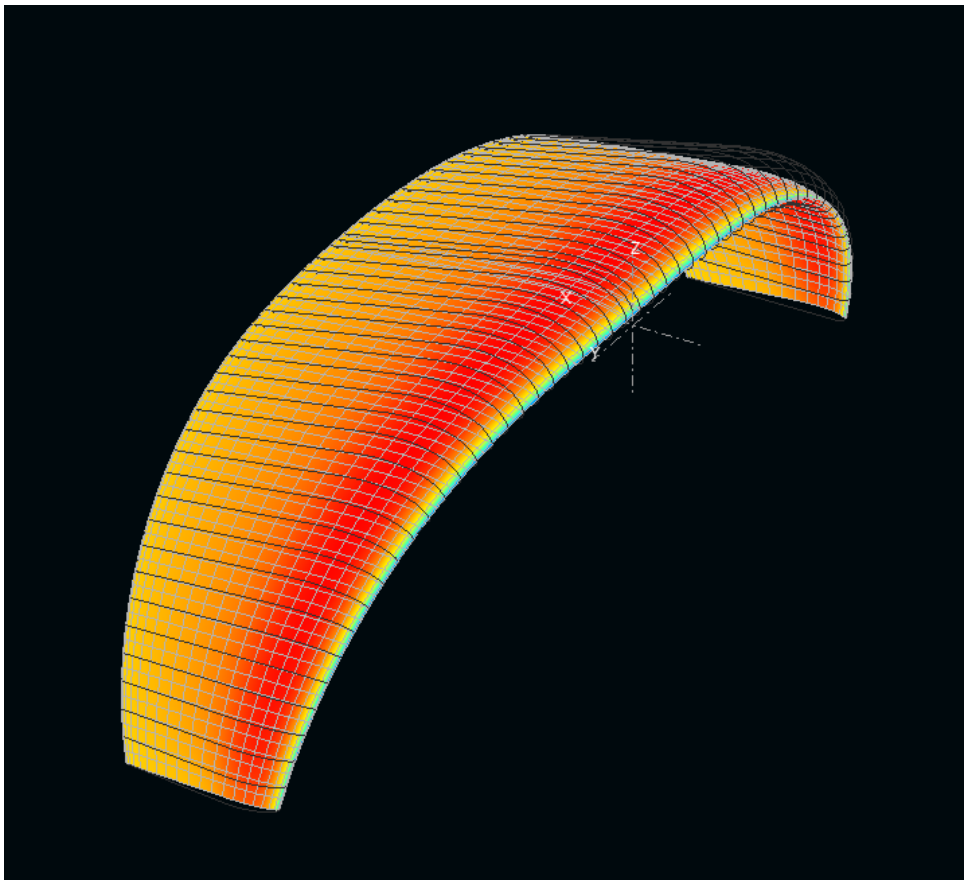

Figure 32 Modified Clark Y Airfoil with flat Bottom parawing in XFLR5

The new wing was then run through the same simulation as the previous parawing allowing for new lift coefficients with angle of attack and required projected planform area to be found as shown in Table 12 and Table 13 below.

Table 12 Lift Coefficient as a function of AoA

Angle of Attack	Coefficient of Lift
-2°	0.236
-1°	0.302
0°	0.367
1°	0.432
2°	0.497
3°	0.562
4°	0.626
5°	0.690

Table 13 Projected Planform Area as a function of AoA

Angle of Attack	Projected Planform Area
-2°	112.9 m^2
-1°	88.2 m^2
0°	72.6 m^2
1°	61.7 m^2
2°	53.6 m^2
3°	47.4 m^2
4°	42.6 m^2

5°	38.6 m^2

Based on these results the new wing allows an incidence angle of between 2° and 3° to be used and accomplish the same lift at cruise. This means the wing will better be able to produce the lift required to climb without going past the stall angle of attack for the wing.

3.4 Hang Glider Design

With the parawing and fixed wing systems designed, the final system, the hang glider, needed to be designed. This system was the last system to be designed, as it was to be built and flown by the team. Therefore, it is significantly smaller than the previous two systems and includes more easily attainable building criteria due to our access to materials and lab space.

3.4.1 Hang Glider Sizing

As with the other two systems, the first step of the design process was to set the total weight of the system. This was done using previous WPI MQP's as a basis, as this MQP would follow the same guidelines. Since the field that the team would be flying from was going to be the same as those previous projects, a similar total weight of 3 kg was chosen [43], [44].

The next step in the design process was to choose an aspect ratio and flight speed for the aircraft. The aspect ratio was chosen based on the North Wing Pacer 13 GT. This is a hang glider and ultralight trike wing with an aspect ratio of 7.25 [42]. A flight speed of 18 m/s was chosen based on research preformed that indicated small UAVs were capable of travel anywhere from 12-36 m/s [43], [53]. As our aircraft is on the lighter end of the spectrum and uses a flexible material for its wing, the cruise flight speed was chosen to be on the lower end of this range.

Once these values were chosen the team chose the wingspan to be 1.5 m, which is based on research in to previous MQP reports [43]. With the wingspan determined, equation 4 was modified to solve for the area of the wing. This resulted in a wing area of 0.31 m^2. Then, using these values in equations 3 and 4, the required lift coefficient was calculated to be 0.6082. The team settled on the MH-82 hang glider airfoil, shown below, at this point because it produced enough lift at all angles of attack greater than 3° as shown in the coefficient of lift vs. alpha plot below.

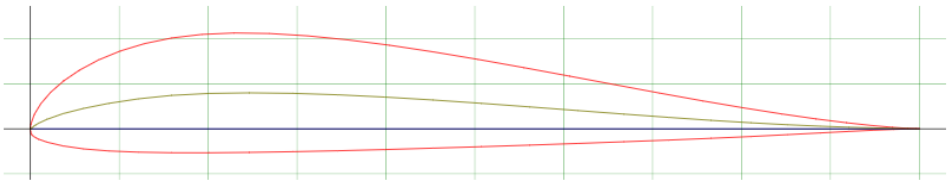

Figure 33 MH82 airfoil cross-section in XFLR5

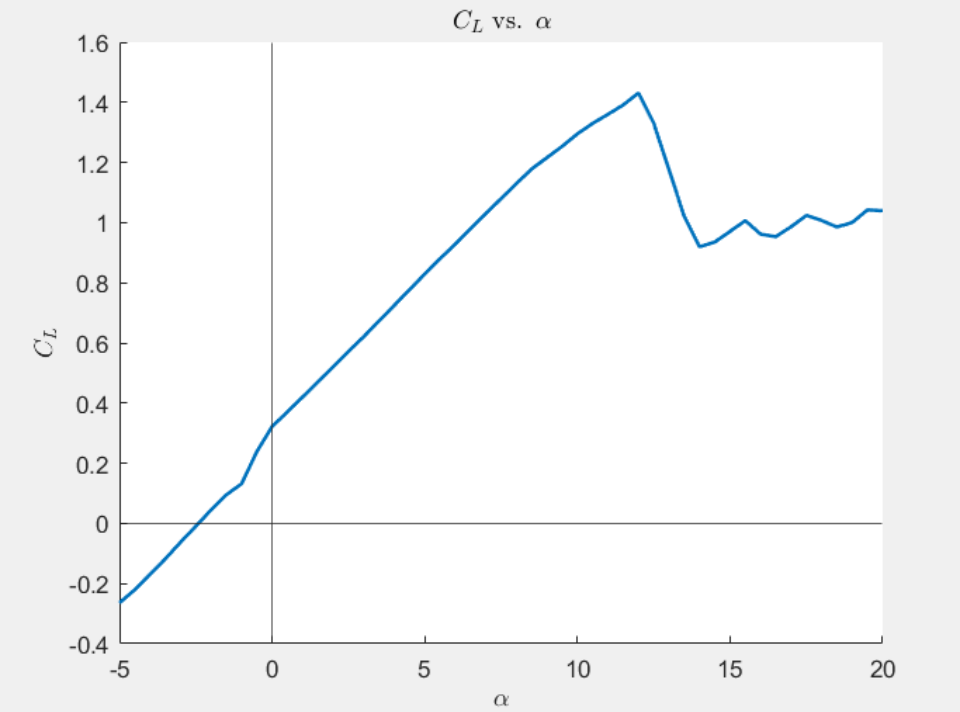

Figure 34 MH82 Airfoil Lift Coefficient as a function of AoA

With the airfoil chosen, the full wing design was next. A mean aerodynamic chord of 0.25 m was chosen based on research into previous similarly sized hang glider designs [43]. A taper ratio of 0.1 was selected for the wing as it best matched the shape of the Pacer 13 GT as seen in the two comparison pictures below, one of the Pacer 13 GT and one of our final Hang glider design in XFLR5.

Figure 35 North Wing Pacer 13 GT Hang Glider[42]

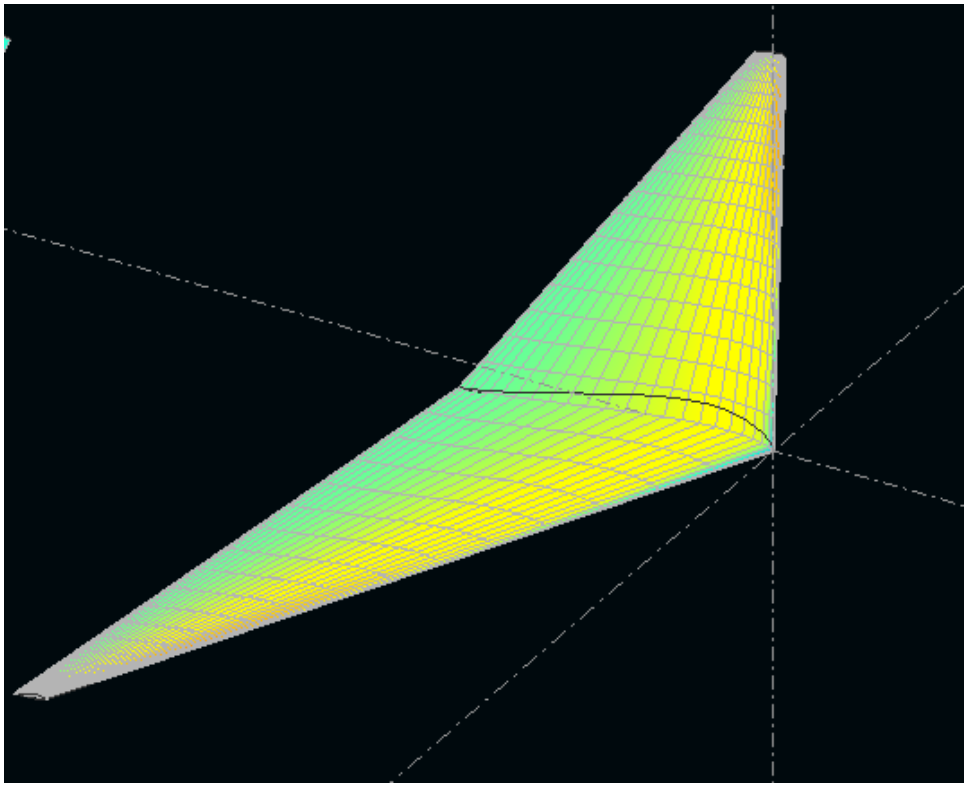

Figure 36 XFLR5 Hang Glider Design

Then using equation 23 below, the value for the root chord was able to be calculated. This gave us a root chord of 0.37 m. Utilizing the root chord and taper ratio, the tip chord was determined to be 0.037 m. A sweep angle of 24° was chosen to match the sweep of the Pacer 13 GT. When designing the hang glider in XFLR5, not all dimensions perfectly matched the intended values as shown below. As such, the incidence angle of the wing was adjusted to ensure enough lift generation.

$$c_{root} = \frac{3\bar{c}(1+TR)}{2(1+TR+TR^2)} \quad 23$$

Table 14 Hang Glider Aerodynamic Parameters

Parameter	Initial Design	Final Design
Aspect Ratio	7.25	7.37
Wingspan	1.5 m	1.5 m
Planform Area	0.31 m^2	0.305 m^2
MAC	0.25 m	0.249 m
Root Chord	0.37 m	0.37 m
Taper Ratio	0.1	0.1
Sweep Angle	24 °	18.418°
Incidence Angle	3°	5°

The next step was to design the tail for the hang glider. The team chose to utilize a v-tail due to the reduction in drag it would allow for [48]. The first steps to creating this tail were the same as for the fixed wing. Using equations 13 and 14 the necessary horizontal and vertical tail areas were calculated. A distance of 1 m was used from the leading edge of the wing to the leading edge of the tail. This was chosen to reduce the necessary size of the tail to make manufacturing it easier. This resulted in the tail areas being 0.053 m^2 for the horizontal stabilizer and 0.018 m^2 for the vertical stabilizer. Because a v-tail was used, the total tail area projected onto the vertical and horizontal planes needed to be equal to the necessary area for the horizontal and vertical stabilizers. This was accomplished using a tail that was 0.057 m^2 at a 19° angle from the horizontal. This was accomplished using equations 24 and 25 below, where theta was varied starting at 30°. Theta was decreased if the resulting guess for the planform area for

the vertical tail was too large and increased if it was too small. With the tail area determined, equations 5 and 6 were used to find the span and chord length of the tail. They were found to be 0.412 m and 0.137 m, respectively.

$$S_{vtail} = \frac{S_{ht}}{\cos\left(-\Gamma_{vtail}\right)} \tag{24}$$

$$S_{vt_{guess}} = S_{vtail}\sin\left(\Gamma_{vtail}\right) \tag{25}$$

To determine the hang glider center of gravity and the required incidence angle for the tail, the same steps used for the fixed wing were repeated. The same incidence angle of 0° was chosen to reduce drag. The trim condition of 0° angle of attack at cruise was desired, so selecting the center of gravity was the same process as for the fixed wing. This resulted in a center of gravity at 0.197 m behind the leading edge of the wing. The aircraft was also found to be statically stable as shown in Figure 37 Moment Coefficient as a function of AoA for the Hang Glider designFigure 37 since the slope of the moment coefficient vs. Angle of attack graph is negative.

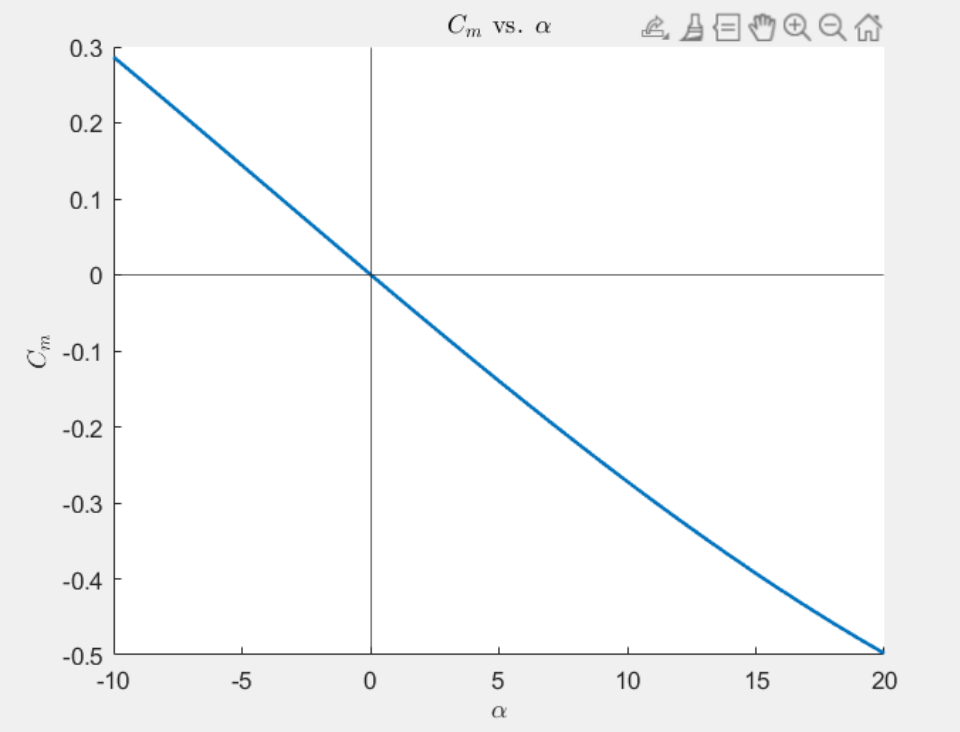

Figure 37 Moment Coefficient as a function of AoA for the Hang Glider design

3.5 Fixed Wing Stability and Control Derivatives

In order to accurately simulate the fixed wing aircraft described in section 2 the stability and control derivatives for the aircraft needed to be found. A variety of sources needed to be used to find these values. These methods consisted of ANSYS Fluent, numbers from similar aircraft, and equations, each described in more detail below.

3.5.1 ANSYS Fluent Analysis for the Fixed Wing

ANSYS Fluent is a CFD software that allows for numerical methods to be used to simulate fluid flows. The team used this software on a variety of parts of the fixed wing aircraft we created. Individual simulations were run on the wing, horizontal tail, horizontal tail with elevator deflection, vertical tail, and fuselage/wing of the aircraft. All the simulations were run at the same atmospheric conditions as detailed in Table 15 below.

Table 15 Fixed-Wing Atmospheric Conditions

Variable	Value
H	5,000 (m)
P	5.405e4 (Pa)
$Temp$	255.68 (K)
ρ	0.7364 (kg/m^3)
μ	16.27e-6 (Pa-s)
V	60 (m/s)

Each of the geometries was meshed using a body of influence geometry around the structure of interest. Additionally, the mesh as refined at the leading and trailing edges of the lifting surface of the structure of interest. Finally, a 10-layer inflation layer was added to help estimate the boundary layer around the structure. For all structures only half of the body was meshed using a symmetry plane condition in the solution to reduce the number of mesh elements and reduce the time for the solution to converge. This is an acceptable assumption since all structures were symmetric across the xz-plane at the midbody of the aircraft. This led to the geometries having the number of mesh elements shown in Table 16 below.

Table 16 Fixed-Wing CFD Mesh Details

Structure	Number of Mesh Elements	Average Orthogonal Quality
Horizontal Tail	980,000	0.74386
Horizontal Tail with Elevator Deflection	1,016,000	0.71906
Vertical Tail	621,000	0.74164
Wing	627,000	0.74649
Wing-Fuselage Combination	796,000	0.73213

The solutions were all run in fluent using either a k-epsilon turbulence assumption with the energy equation or a simplified k-omega turbulence assumption without the energy equation. The simplification took place as the models became more complex as it allowed for better convergence. The assumption to remove the energy equation was made because the low flight speed of the aircraft meant we were in the incompressible regime for the air flow meaning very little temperature change would take place across the structure. The lack of energy equation greatly reduced the time for the solution to converge. Using the results of each simulation run at a variety of angles of attack for each structure the values in Table 17 were found. The velocity profiles at the symmetry plane for both the wing-fuselage combination and horizontal tail can be found in Figure 38 and Figure 39 below.

Table 17 Fixed-Wing Aerodynamic Coefficients from CFD

Variable	Value	Variable	Value
C_{D_0}	0.0289	C_{L_1}	0.5079
C_{D_1}	0.0434	$C_{L_{\alpha_w}}$	4.1635
$C_{L_{\alpha_{wb}}}$	2.6872	$C_{L_{\alpha_{ht}}}$	3.1923
$C_{L_{\alpha_{vt}}}$	3.3575	C_{L_0}	0.5079

$C_{L_{\delta e_{ht}}}$	2.5888	$C_{D_{\delta e_{ht}}}$	0.0802

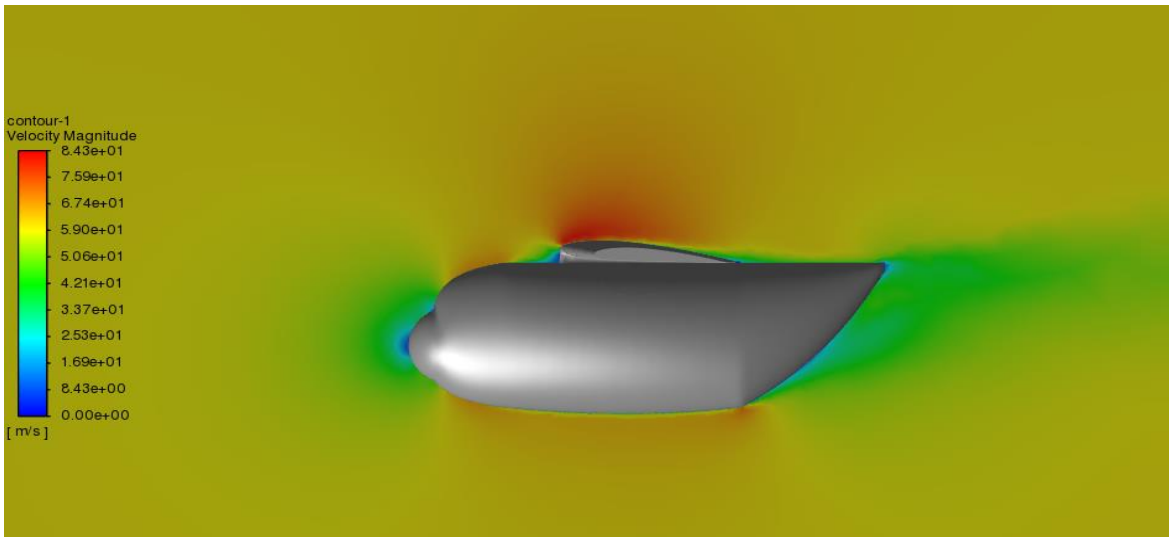

Figure 38 Velocity Magnitude Contour from Ansys Fluent for Fixed Wing Wing-Fuselage Combination at 0˚Angle of Attack

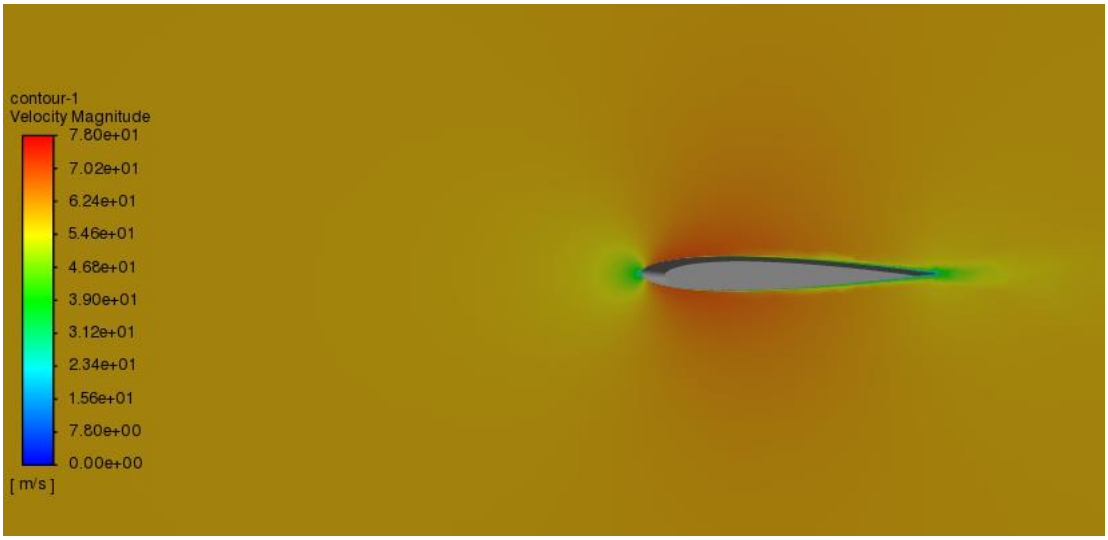

Figure 39 Velocity Magnitude Contour from Ansys Fluent for Fixed Wing Horizontal Tail Combination at 0˚Angle of Attack

3.5.2 Numbers from Similar Aircraft

Not all numbers could be found directly using fluent. Some values need to be found using experimental data. Because the team was not creating a model for the fixed wing aircraft a similar aircraft needed to be used to find these values. The Cessna 182 was chosen to serve as this aircraft for several reasons. The first is that the engine in the Cessna is very similar to the engine we chose for our fixed wing aircraft. This meant that the stability and control derivatives based around the engine could be approximated using the Cessna 182. The second reason the Cessna was a good fit was because it is very similarly sized and has the same general shape as our aircraft. This again reinforced that numbers approximated from the Cessna 182 would be close to the values for our aircraft. The values that were approximated for our aircraft using the Cessna 182 are listed in Table 18 below [54].

Table 18 Fixed-Wing Aerodynamic Coefficients from Similar Aircraft

Variable	Value	Variable	Value
$k_{a,yaw}$	-0.0425	$k_{a,eff}$	0.055
$k_{r,eff}$	0.0557	C_{m_1}	0
$C_{T_{x1}}$	0.032	$C_{m_{T1}}$	0
$C_{m_{u1}}$	0	$C_{m_{Tu}}$	0
$C_{T_{xu}}$	-0.096	$C_{y_{\delta a}}$	0

3.5.3 Equations

Once all the base values had been found from either ANSYS Fluent or from the Cessna 182 equations were used to calculate the rest of the stability and control derivatives. The equations listed below were used to calculate the derivatives listed in Table 19.

$$C_{L_\alpha} = C_{L_{\alpha_{wb}}} + (C_{L_{\alpha_{ht}}} \frac{S_{ht}}{S_w}(1 - k_{\varepsilon,\alpha})) \quad 26$$

$$C_{L_{\dot{\alpha}}} = 2C_{L_\alpha} k_{\varepsilon,\alpha} \bar{V}_{ht} \quad 27$$

$$C_{L_q} = 2C_{L_{\alpha_{ht}}} \bar{V}_{ht} \quad 28$$

$$C_{D_\alpha} = \frac{2C_{L_1}}{\pi ARe} C_{L_\alpha} \quad (29)$$

$$C_{m_q} = -C_{L_q} \frac{(\bar{l}_{ht} - (h_{ac} - h_{cm})\bar{c})}{\bar{c}} \quad (30)$$

$$C_{m_\alpha} = C_{L_\alpha}(h_{ac} - h_{cm}) - \bar{V}_{ht} C_{L_{\alpha_{ht}}}(1 - k_{\varepsilon,\alpha}) \quad (31)$$

$$C_{m_{\dot{\alpha}}} = -C_{L_{\dot{\alpha}}} \frac{(\bar{l}_{ht} - (h_{ac} - h_{cm})\bar{c})}{\bar{c}} \quad (32)$$

$$C_{m_{ac_w}} = \frac{C_{m_{0_{airfoil}}} AR \cos(\lambda_w)^2}{AR + 2\cos(\lambda_w)} \quad (33)$$

$$C_{m_0} = C_{m_{ac_w}} + C_{L_0}(h_{cm} - h_{ac}) - \bar{V}_{ht} C_{L_{\alpha_{ht}}}(i_{ht} - \varepsilon_0) \quad (34)$$

$$C_{D_{\delta e}} = \frac{S_{ht}}{S_w} C_{D_{\delta e_{ht}}} \quad (35)$$

$$C_{L_{\delta e}} = \frac{S_{ht}}{S_w} C_{L_{\delta e_{ht}}} \quad (36)$$

$$C_{m_{\delta e}} = C_{L_{\delta e}}(h_{cm} - h_{ac}) - C_{L_{\delta e_{ht}}} \bar{V}_{ht} \quad (37)$$

$$C_{y_\beta} = -C_{L_{\alpha_{vt}}} \frac{S_{vt}}{S_w} \quad (38)$$

$$C_{n_\beta} = -C_{y_\beta} \frac{l_{vt}}{b} \quad (39)$$

$$C_{l_\beta} = \frac{1}{6} C_{L_{\alpha_w}} \Gamma_w \left(\frac{1 + 2TR}{1 + TR}\right) - 2C_{L_1} \frac{y_{ac}}{b} \sin(2\lambda_w) + \frac{z_{vt}}{b} C_{y_\beta} \quad (40)$$

$$C_{y_p} = -2C_{L_{\alpha_{vt}}} \frac{z_{vt}}{b} \frac{S_{vt}}{S_w} \quad (41)$$

$$C_{n_p} = -C_{y_p} \frac{l_{vt}}{b} - \frac{1}{8} C_{L_1} \quad (42)$$

$$C_{l_p} = C_{y_p} \frac{z_{vt}}{b} \quad (43)$$

$$C_{y_r} = 2C_{L_{\alpha_{vt}}} \frac{l_{vt}}{b} \frac{S_{vt}}{S_w} \quad 44$$

$$C_{n_r} = -C_{y_r} \frac{l_{vt}}{b} \quad 45$$

$$C_{l_r} = C_{y_r} \frac{z_{vt}}{b} \quad 46$$

$$C_{n_{\delta a}} = -k_{a,yaw} C_{L_1} \quad 47$$

$$C_{l_{\delta a}} = k_{a,eff} C_{L_{\alpha_w}} \quad 48$$

$$C_{y_{\delta r}} = k_{r,eff} C_{L_{\alpha_{vt}}} \quad 49$$

$$C_{n_{\delta r}} = -k_{r,eff} \frac{l_{vt}}{b} C_{L_{\alpha_{vt}}} \quad 50$$

$$C_{l_{\delta r}} = k_{r,eff} \frac{z_{vt}}{b} C_{L_{\alpha_{vt}}} \quad 51$$

Table 19 Fixed-Wing Aerodynamic Coefficients from Equations

Variable	Value	Variable	Value
C_{L_α}	3.1589	$C_{L_{\dot{\alpha}}}$	1.4743
C_{L_q}	4.5466	C_{D_α}	0.1804
C_{m_q}	-14.3067	C_{m_α}	-1.8836
$C_{m_{\dot{\alpha}}}$	-4.6392	$C_{m_{ac_w}}$	-0.0415
C_{m_0}	-0.0974	$C_{D_{\delta e}}$	0.0175
$C_{L_{\delta e}}$	0.5661	$C_{m_{\delta e}}$	-1.9058
C_{y_β}	-0.2015	C_{n_β}	0.1012

C_{l_β}	-0.0112	C_{y_p}	-0.0223
C_{n_p}	-0.0523	C_{l_p}	-0.0012
C_{y_r}	0.2024	C_{n_r}	-0.1016
C_{l_r}	0.0112	$C_{n_{\delta a}}$	0.0216
$C_{l_{\delta a}}$	0.2290	$C_{y_{\delta r}}$	0.1870
$C_{n_{\delta r}}$	-0.0939	$C_{l_{\delta r}}$	0.0104

3.5.4 Longitudinal Non-Dimensional Derivatives

Once the stability and control derivatives were calculated many of the values were used to calculate the longitudinal non-dimensional derivatives. These are the final values that need to be found before design of a controller for an aircraft can begin. The equations below show how these values were found and Table 22 in section 4.1.1 shows the values for these variables.

$$C_{x_u} = -(C_{D_u} + 2C_{D_1}) \quad 52$$

$$C_{x_\alpha} = C_{L_1} - C_{D_\alpha} \quad 53$$

$$C_{x_{\dot{\alpha}}} = 0 \quad 54$$

$$C_{x_q} = 0 \quad 55$$

$$C_{x_{\delta e}} = -C_{D_{\delta e}} \quad 56$$

$$C_{x_{\delta p}} = C_{T_{xu}} + 2C_{T_{x1}} \quad 57$$

$$C_{z_u} = -(C_{L_u} + 2C_{L_1}) \quad 58$$

$$C_{z_\alpha} = -(C_{L_\alpha} + C_{D_1}) \quad 59$$

$$C_{z_{\dot{\alpha}}} = -C_{L_{\dot{\alpha}}} \quad (60)$$

$$C_{z_q} = -C_{L_q} \quad (61)$$

$$C_{z_{\delta e}} = -C_{L_{\delta e}} \quad (62)$$

$$C_{z_{\delta p}} = 0 \quad (63)$$

$$C_{m_u} = C_{m_{u1}} + 2C_{m_1} \quad (64)$$

$$C_{m_{\delta p}} = C_{m_{Tu}} + 2C_{m_{T1}} \quad (65)$$

3.6 Parawing Stability and Control Derivatives

Similar to the fixed wing stability and control derivatives the parawing derivatives were gathered from several sources. Due to the lack of equations for parawing stability and control derivatives the values were gathered in two methods, using Fluent and from [52].

3.6.1 ANSYS Fluent Analysis for the Parawing

The atmospheric conditions for the Fluent analyses were the same use described in section 3.5.1 with the exception of V. For the parawing case $V = 20$ m/s was used instead because of the structural limitations of parawings as described previously. Two simulations were run. One which analyzed the fuselage of the parawing and one which analyzed the wing itself. The technique used to mesh the two bodies was the same as described in section 3.5.1. Both simulations were run with 0 angle of attack. The number of elements and average orthogonal quality of the mesh I listed in Table 20 below. The wing used was the same one used in [52]. While this wing did not have the same shape or overall dimensions as our final wing, as shown in Figure 40 vs Figure 32, it utilized the same airfoil so would likely provide similar non-dimensional aerodynamic coefficients to our wing.

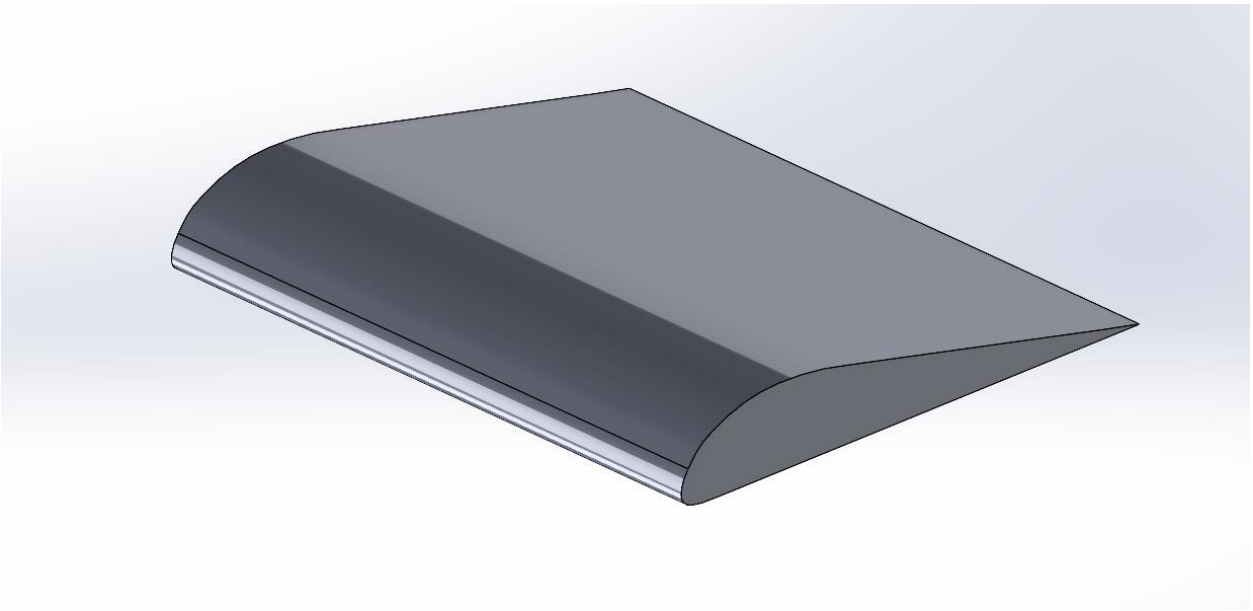

Figure 40 Wing from [52]

Table 20 Parawing CFD Mesh Details

Structure	Number of Mesh Elements	Average Orthogonal Quality
Fuselage	1,174,000	0.786
Wing	3,111,000	0.76095

The simulations, led to the values in Table 21 below being found. Both the lift and drag coefficients found during the simulation for the wing matched the values displayed in [52] validating the results of the simulation. The velocity profiles at the symmetry plane for both the parawing and fuselage can be found in Figure 41 and Figure 42 below.

Table 21 Parawing Aerodynamic Coefficients from CFD

Structure	C_L	C_D
Fuselage	0	0.0014
Wing	0.2358	0.0270

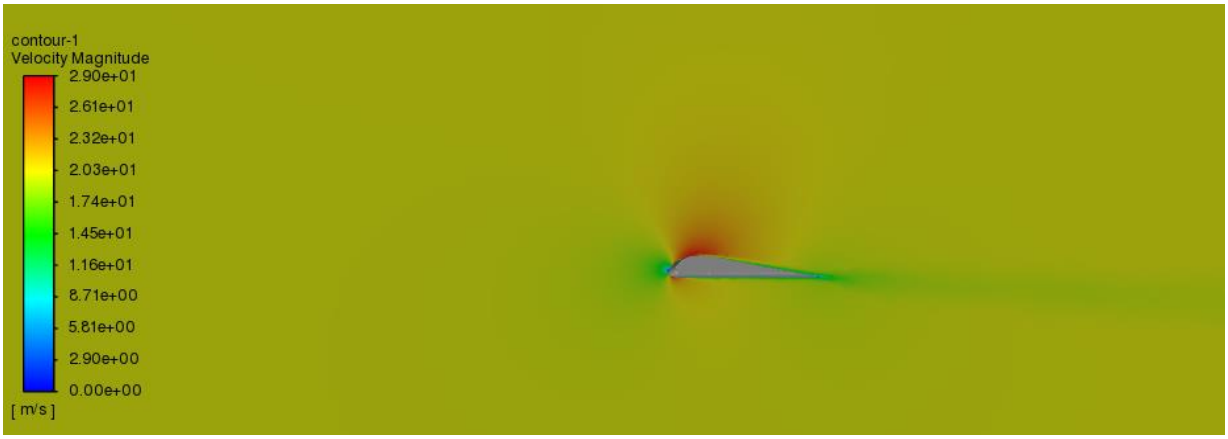

Figure 41 Velocity Magnitude Contour from Ansys Fluent for Parawing at 0° Angle of Attack

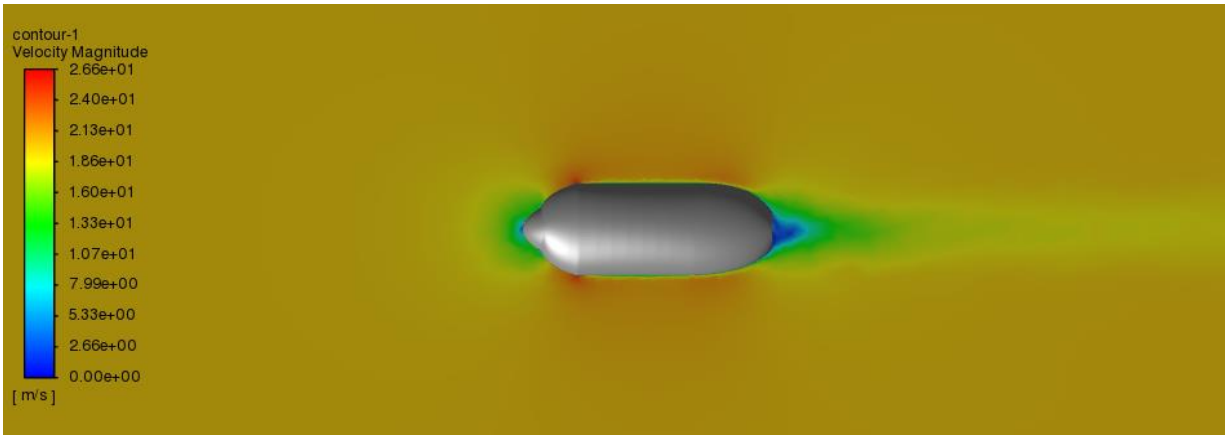

Figure 42 Velocity Magnitude Contour from Ansys Fluent for Parawing Fuselage at 0° Angle of Attack

3.6.2 Values from [52]

Table 1 from [52] was used to find the majority of the stability and control derivatives for the parawing. As discussed in section 3.6.1 the geometry of the wing in [52] does not perfectly match the geometry of our wing however the values in Table 1 from [52] were the closest approximation to the values of our wing we could find. Using those values along with the values in Table 21 in conjunction with the equations discussed in section 3.5.4 the final non-dimensional derivatives were calculated as shown in section 4.1.2. When calculating the values for the longitudinal control derivatives symmetric deflection of the parawing was assumed so the values in Table 1 from [52] were doubled. When finding the lateral control derivatives, the deflection was assumed to be asymmetric, so the values were not doubled.

3.7 Trajectory Generation

As the fixed wing, parawing, and hang glider is designed and modeled in SOLIDWORKS, the simulation code in MATLAB is expanded and improved upon as well. The 3-DOF state space model is

adjusted to include lateral motion, therefore allowing the system to have 6 degrees to freedom: motion along the x, y, and z axes as well as roll pitch and yaw. After this state space expansion, simple trajectories are implemented within the simulation to test the performance of the new model. To do this, control equations are created for different legs of the trajectory (ie., takeoff, cruise, descending helix, glide). Conditions for when the trajectory changed phases were also developed. The simple trajectory generation methods will be further explained below. This trajectory takes an input file. We have two different input files, one for fixed wing and one for parawing.

3.7.1 6-DOF System

The six degree of freedom state space model included a total of seven state variables: position in the x, y, and z directions (p_x, p_y, p_z), body fixed velocity (V), pitch angle (γ), yaw angle (ψ), and mass (m). Although the roll angle (ϕ) was not an actual state variable, it was used as an input for the $\dot{x}$ matrix; more specifically, ϕ is an input variable for $\dot{\psi}$ and $\dot{\gamma}$. This state space accounts for both lateral and longitudinal motion but is still a simplified model to some extent because it does not account angular rotation rates or body fixed velocity components.

$$\dot{x} = \begin{bmatrix} \dot{p_x} \\ \dot{p_y} \\ \dot{p_z} \\ \dot{V} \\ \dot{\gamma} \\ \dot{\psi} \\ \dot{m} \end{bmatrix} = \begin{bmatrix} V\cos(\psi)\cos(\gamma) \\ V\sin(\psi)\cos(\gamma) \\ -V\sin(\gamma) \\ \frac{T - D - W\sin(\gamma) - \dot{m}V}{m} \\ \frac{L\cos(\phi) - W\cos(\gamma)}{mV} \\ \frac{L\sin(\phi)}{mV\cos(\gamma)} \\ -c_t * power \end{bmatrix} \quad (66)$$

3.7.2 Control Equations

The equations for the control inputs of each phase of the trajectory were created. The four phases of the trajectory are climb, cruise, descending helix, and descent. The control inputs put into the system are engine power, lift and drag, coefficients of lift and drag, and the bank angle.

The cruise and climb phases have the following governing equations:

$$P = C * \eta_{prop} P_{max} \frac{\rho}{\rho_{SL}} \quad 67$$

$$C_L = \frac{mg * cos(\gamma)}{\frac{1}{2}\rho V^2 S} \quad 68$$

$$\phi = 0 \quad 69$$

We use 80% power for climb. The bank angle is 0 since we are not turning during climb.

The equations for cruise are very similar to climb, but we need less power, 65%, since we are maintaining steady level flight. Steady level flight is when lift equals weight and our pitch angle is zero. This simplifies the equation from the previous climb equation.

The descending helix is the only flight mode with nonzero heading and roll angles. The heading angle is set to a constant determined by:

$$\dot{\psi} = \frac{V}{R} \quad 70$$

When solving our equations of motion with the constraints for a turning aircraft, we achieve the following equations:

$$P = \frac{DV * WVsin(\gamma_0)}{1 + c_t V^2} \quad 71$$

$$C_L = \frac{mgcos(\gamma_0)}{qScos(\phi)} \quad 72$$

$$\phi = tan^{-1}\left(\frac{V^2}{Rg}\right) \quad 73$$

This equation is not in terms of engine power since it is an accelerated maneuver and the amount of power needed depends on the velocity going into the maneuver. The coefficient of lift is dependent on the bank angle and we solved the bank angle to be dependent only on two constants, radius of turn and gravity, and the velocity entering the turn.

3.7.3 Trajectory Phase Transitions

The different phases of the trajectory have a few parameters that mark when they end or how they behave. Previously, the design space exploration trajectory included a takeoff (climb) phase to reach a desired altitude, a steady level cruise phase until the aircraft had no fuel remaining, and a glide phase to return to the ground. For the current simulations, a slightly different approach was taken. For the climb phase, the phase ends when the particle that is modeled reaches a desired altitude of 5km (same as DSE). The cruise condition ends when a specific x position of 500km is reached. Then the aircraft enters a helical descent is initiated. The helical ends when we reach a payload drop altitude of 50 meters and then a climb occurs back into a second cruise phase. Once an additional 500km of flight is achieved, the aircraft descends till it hits the ground (sea level in this simulation). In Figure 43Figure 43 Full Scale , the full flight pattern of the fixed wing aircraft is shown.

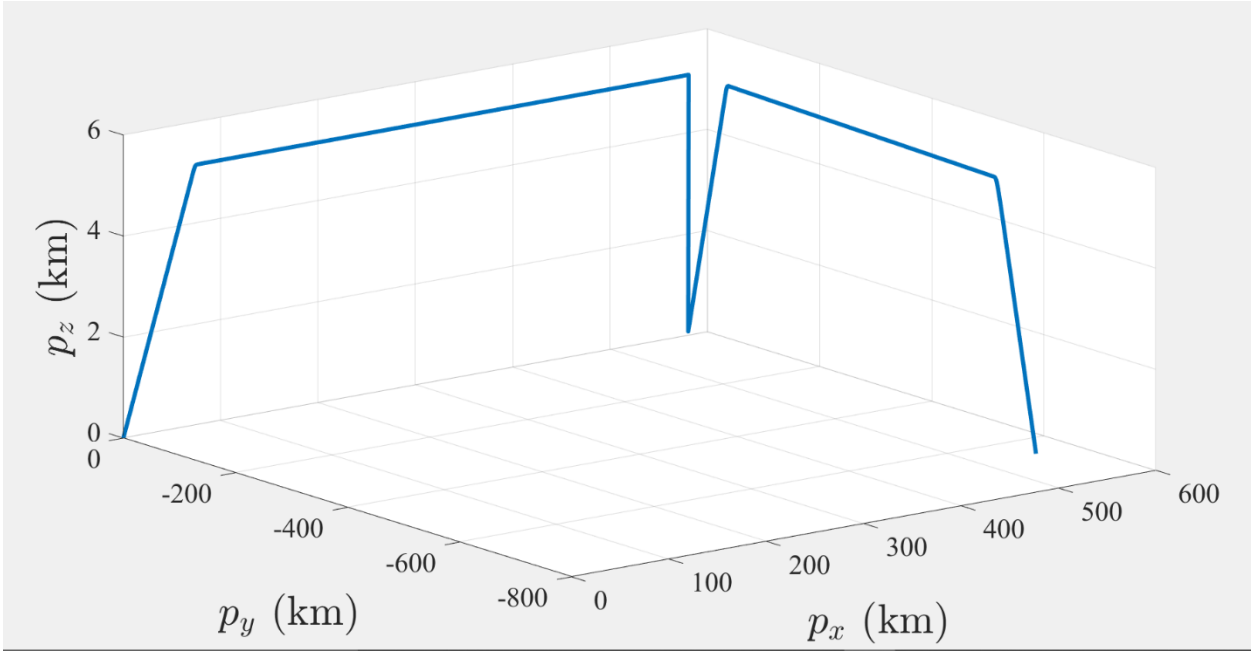

Figure 43 Full Scale Trajectory

3.8 High-Fidelity Controllers

Once the trajectory was generated, the aircraft needed to be analyzed at a high level of fidelity. To do this we use Etkin and Reid's linearized 12 state model of motion [40]. These equations of motion are

linearized about an equilibrium point. The equilibrium points used are trim states pulled from the beginning of each phase our trajectory that we created. We pulled one point from each of the phases of flight to create a trim A and B matrix for each phase of flight both longitudinal and lateral.

Etkin and Reid's Model defines a series of control and stability derivatives as non-dimensional values similar to the definition of coefficients of lift and drag. The control and stability derivatives needed to find the aircraft's dimensional derivatives are found in the Fluent simulations. Equations 74-103 are these stability and control derivatives. These equations are used to find the matrices in equations 104-110. The square matrix is our A matrix, and the second term includes our B matrix.

$$X_u = 2\frac{mg}{V^*}sin\theta^* + \frac{1}{2}\rho^* V^* S(C_{D_u} + 2C_D^*) \tag{74}$$

$$X_w = \frac{1}{2}\rho^* V^* S(C_L^* - C_{D_\alpha}) \tag{75}$$

$$X_q = 0 \tag{76}$$

$$X_{\dot{w}} = 0 \tag{77}$$

$$Z_u = -2\frac{mg}{V^*}cos\theta^* - \frac{1}{2}\rho^* V^* S(C_{L_u} + 2C_L^*) \tag{78}$$

$$Z_w = -\frac{1}{2}\rho^* V^* S(C_D^* - C_{L_\alpha}) \tag{79}$$

$$Z_q = -\frac{1}{4}\rho^* V^* S\bar{c}C_{L_q} \tag{80}$$

$$Z_{\dot{w}} = -\frac{1}{4}\rho^* S\bar{c}C_{L_{\dot{\alpha}}} \tag{81}$$

$$M_u = \frac{1}{2}\rho^* V^* S\bar{c}C_{M_u} \tag{82}$$

$$M_w = \frac{1}{2}\rho^* V^* S\bar{c} C_{L_\alpha} \quad 83$$

$$M_q = \frac{1}{4}\rho^* V^* S\bar{c}^2 C_{M_q} \quad 84$$

$$M_{\dot{w}} = \frac{1}{4}\rho^* V^* S\bar{c}^2 C_{M_{\dot{\alpha}}} \quad 85$$

$$X_{\delta e} = -\frac{1}{2}\rho^* (V^*)^2 S C_{D_{\delta e}} \quad 86$$

$$Z_{\delta e} = -\frac{1}{2}\rho^* (V^*)^2 S C_{L_{\delta e}} \quad 87$$

$$M_{\delta e} = \frac{1}{2}\rho^* (V^*)^2 S\bar{c} C_{M_{\delta e}} \quad 88$$

$$Y_v = \frac{1}{2}\rho^* V^* S C_{Y_\beta} \quad 89$$

$$l_v = \frac{1}{2}\rho^* V^* S b C_{l_\beta} \quad 90$$

$$N_v = \frac{1}{2}\rho^* V^* S b C_{N_\beta} \quad 91$$

$$Y_p = \frac{1}{4}\rho^* V^* S b C_{Y_p} \quad 92$$

$$l_p = \frac{1}{4}\rho^* V^* S b^2 C_{l_p} \quad 93$$

$$N_p = \frac{1}{4}\rho^* V^* S b^2 C_{N_p} \quad 94$$

$$Y_r = \frac{1}{4}\rho^* V^* S b C_{Y_r} \quad (95)$$

$$l_r = \frac{1}{4}\rho^* V^* S b^2 C_{l_r} \quad (96)$$

$$N_r = \frac{1}{4}\rho^* V^* S b^2 C_{N_r} \quad (97)$$

$$Y_{\delta a} = \frac{1}{2}\rho^* V^* S C_{Y_{\delta a}} \quad (98)$$

$$l_{\delta a} = \frac{1}{2}\rho^* (V^*)^2 S b C_{Y_\beta} \quad (99)$$

$$N_{\delta a} = \frac{1}{2}\rho^* (V^*)^2 S b C_{Y_\beta} \quad (100)$$

$$Y_{\delta r} = \frac{1}{4}\rho^* (V^*)^2 S C_{Y_{\delta r}} \quad (101)$$

$$l_{\delta r} = \frac{1}{4}\rho^* (V^*)^2 S b C_{l_{\delta r}} \quad (102)$$

$$N_{\delta r} = \frac{1}{4}\rho^* (V^*)^2 S b C_{N_{\delta r}} \quad (103)$$

$$M' = \frac{M_{\dot{w}}}{m - Z_{\dot{w}}} \quad (104)$$

$$J' = \begin{bmatrix} J_x{}' \\ J_z{}' \\ J_{zx}{}' \end{bmatrix} = \begin{bmatrix} \frac{J_x J_z - J_{zx}^2}{J_z} \\ \frac{J_x J_z - J_{zx}^2}{J_x} \\ \frac{J_{zx}}{J_x J_z - J_{zx}^2} \end{bmatrix} \quad (105)$$

$$\begin{bmatrix}\Delta\dot{u}\\ \Delta\dot{w}\\ \Delta\dot{q}\\ \Delta\dot{\theta}\\ \Delta\dot{p}_z\\ \Delta\dot{p}_x\end{bmatrix}=\begin{bmatrix} X_u/m & X_w/m & 0 & -g\cos\theta^* & 0 & 0\\ \dfrac{Z_u}{m-Z_{\dot{w}}} & \dfrac{Z_w}{m-Z_{\dot{w}}} & \dfrac{Z_q+mu^*}{m-Z_{\dot{w}}} & \dfrac{-mg\sin\theta^*}{m-Z_{\dot{w}}} & 0 & 0\\ \dfrac{M_u+M'Z_u}{J_y} & \dfrac{M_w+M'Z_w}{J_y} & \dfrac{M_q+M'(Z_q+mu^*)}{J_y} & \dfrac{-M'mg\sin\theta^*}{J_y} & 0 & 0\\ 0 & 0 & 1 & 0 & 0 & 0\\ -\sin\theta^* & \cos\theta^* & 0 & -V^*\cos\theta^* & 0 & 0\\ \cos\theta^* & \sin\theta^* & 0 & -V^*\sin\theta^* & 0 & 0\end{bmatrix}\begin{bmatrix}\Delta u\\ \Delta w\\ \Delta q\\ \Delta\theta\\ \Delta p_z\\ \Delta p_x\end{bmatrix}+\begin{bmatrix} X_{\delta_e}/m\\ \dfrac{Z_{\delta e}}{m-Z_{\dot{w}}}\\ \dfrac{M_{\delta_e}}{J_y}+\dfrac{M_{\dot{w}}Z_{\delta e}}{J_y(m-Z_{\dot{w}})}\\ 0\\ 0\\ 0\end{bmatrix}\Delta\delta e \tag{106}$$

$$\begin{bmatrix}\Delta\dot{v}\\ \Delta\dot{p}\\ \Delta\dot{r}\\ \Delta\dot{\phi}\\ \Delta\dot{\psi}\\ \Delta\dot{p}_y\end{bmatrix}=\begin{bmatrix} Y_v/m & Y_p/m & -V^*+Y_r/m & & & \\ \dfrac{l_v}{J'_x}+J'_{zx}N_v & \dfrac{l_p}{J'_x}+J'_{zx}N_p & \dfrac{l_r}{J'_x}+J'_{zx}N_r & g\cos\theta^* & 0 & 0\\ \dfrac{N_v}{J'_z}+J'_{zx}l_v & \dfrac{N_p}{J'_z}+J'_{zx}l_p & \dfrac{N_r}{J'_z}+J'_{zx}l_r & 0 & 0 & 0\\ 0 & 1 & \tan\theta^* & 0 & 0 & 0\\ 0 & 0 & \sec\theta^* & 0 & 0 & 0\\ 1 & 0 & 0 & 0 & V^*\cos\theta^* & 0\end{bmatrix}\begin{bmatrix}\Delta v\\ \Delta p\\ \Delta r\\ \Delta\phi\\ \Delta\psi\\ \Delta p_y\end{bmatrix}+\begin{bmatrix} Y_{\delta a}/m & Y_{\delta r}/m\\ \dfrac{l_{\delta a}}{J'_x}+J'_{zx}N_{\delta a} & \dfrac{l_{\delta r}}{J'_x}+J'_{zx}N_{\delta r}\\ \dfrac{N_{\delta a}}{J'_z}+J'_{zx}l_{\delta a} & \dfrac{N_{\delta r}}{J'_z}+J'_{zx}l_{\delta r}\\ 0 & 0\\ 0 & 0\\ 0 & 0\end{bmatrix}\begin{bmatrix}\Delta\delta a\\ \Delta\delta r\end{bmatrix} \tag{107}$$

$$\begin{bmatrix}\Delta\dot{u}\\ \Delta\dot{w}\\ \Delta\dot{q}\\ \Delta\dot{\theta}\\ \Delta\dot{p}_z\\ \Delta\dot{p}_x\end{bmatrix} = \begin{bmatrix} \frac{X_u}{m} & \frac{X_w}{m} & 0 & -g\cos\theta^* & 0 & 0\\ \frac{Z_u}{m-Z_{\dot{w}}} & \frac{Z_w}{m-Z_{\dot{w}}} & \frac{Z_q+mu^*}{m-Z_{\dot{w}}} & \frac{-mg\sin\theta^*}{m-Z_{\dot{w}}} & 0 & 0\\ \frac{M_u+M'Z_u}{J_y} & \frac{M_w+M'Z_w}{J_y} & \frac{M_q+M'(Z_q+mu^*)}{J_y} & \frac{-M'mg\sin\theta^*}{J_y} & 0 & 0\\ 0 & 0 & 1 & 0 & 0 & 0\\ -\sin\theta^* & \cos\theta^* & 0 & -V^*\cos\theta^* & 0 & 0\\ \cos\theta^* & \sin\theta^* & 0 & -V^*\sin\theta^* & 0 & 0 \end{bmatrix} \begin{bmatrix}\Delta u\\ \Delta w\\ \Delta q\\ \Delta\theta\\ \Delta p_z\\ \Delta p_x\end{bmatrix} + \begin{bmatrix} \frac{X_{\delta s}}{m}\\ \frac{Z_{\delta s}}{m-Z_{\dot{w}}}\\ \frac{M_{\delta_s}}{J_y}+\frac{M_{\dot{w}}Z_{\delta s}}{J_y(m-Z_{\dot{w}})}\\ 0\\ 0\\ 0 \end{bmatrix}\Delta\delta s \quad (108)$$

$$\begin{bmatrix}\Delta\dot{v}\\ \Delta\dot{p}\\ \Delta\dot{r}\\ \Delta\dot{\phi}\\ \Delta\dot{\psi}\\ \Delta\dot{p}_y\end{bmatrix} = \begin{bmatrix} Y_v/m & Y_p/m & -V^*+Y_r/m & & & \\ \frac{l_v}{J'_x}+J'_{zx}N_v & \frac{l_p}{J'_x}+J'_{zx}N_p & \frac{l_r}{J'_x}+J'_{zx}N_r & g\cos\theta^* & 0 & 0\\ \frac{N_v}{J'_z}+J'_{zx}l_v & \frac{N_p}{J'_z}+J'_{zx}l_p & \frac{N_r}{J'_z}+J'_{zx}l_r & 0 & 0 & 0\\ 0 & 1 & \tan\theta^* & 0 & 0 & 0\\ 0 & 0 & \sec\theta^* & 0 & 0 & 0\\ 1 & 0 & 0 & 0 & V^*\cos\theta^* & 0 \end{bmatrix} \begin{bmatrix}\Delta v\\ \Delta p\\ \Delta r\\ \Delta\phi\\ \Delta\psi\\ \Delta p_y\end{bmatrix} + \begin{bmatrix} Y_{\delta a}/m\\ \frac{l_{\delta a}}{J'_x}+J'_{zx}N_{\delta a}\\ \frac{N_{\delta a}}{J'_z}+J'_{zx}l_{\delta a}\\ 0\\ 0\\ 0 \end{bmatrix}[\Delta\delta as] \quad (109)$$

Once our A and B matrices are found, we create linear controllers for longitudinal and lateral motion in each phase of flight. We control all the states except the x-direction position, because this had no effect on the aircraft's deviation from the desired trajectory. We used a linear quadratic regulator (LQR) to find the values for each gain matrix. The LQR solves the algebraic Riccati equation to find the optimal gain values given a specified weight of the states and control inputs. The algebraic Riccati equation is as follows:

$$A^T S + SA - SBR^{-1}B^T S + Q = 0 \quad (110)$$

Where the weight matrices ('R' and 'Q') are found using an iterative guess and check method until the response of the system reaches a desired level of efficiency. The 'A' and 'B' matrices defined by the system dynamics. Then, the gain matrix 'K' and control input 'u' are given by:

$$K = R^{-1}B^T S \quad (111)$$

$$u = -Kx \quad (112)$$

3.9 Structural Simulations

Structural analysis of the fixed wing and parafoil designs was planned and conducted in Ansys Workbench utilizing the static structural simulation. For the fixed wing, focus was placed on the structural integrity of the Main Wing and mounting system. Iteration to correspond to the results of this simulation helped to create a more structurally stable wing by changing the CAD model without altering aerodynamics or control actuators. Due to carbon fiber's orthotropic elasticity multiple separate materials were created corresponding to different orientations of the fibers. Three in total, for versions of the material that could be oriented along the principal axes.

3.9.1 Fixed-Wing Structural Simulation

To get the airframe to properly mesh without applying large loads on the computers, an element size of 5 mm was chosen. A fine span angle center was chosen to allow for a more detailed mesh along curved regions of the model. The fixed support was placed on the inside of the central wing mounting, while the net lift force was placed on the bottom facing faces of the stringers and I-beams that would be in contact with the skin. A drag force was added to the front facing faces; however, the mesh is not detailed enough in the areas that these forces resolve to reveal any useful results.

Simplifying the fixed-wing model to successfully run the simulation, while also retaining and adding the necessary details to the model such that connections between parts represent actual physical connections. The simulation focuses on the structural integrity of the main wing. To apply fixed supports the wing mounting apparatus was also included. A fixed Support is attached to the bottom of the wing mounting apparatus, to simulate attachment to the fuselage of the aircraft. The skin of the wing caused

complications when meshing. To address this problem the skin was suppressed, and the assumption was made that all the aerodynamic forces were applies directly to the ribs and spars on faces that would be connected to the skin. The inertial gravity feature was used to apply gravity and the thrust force was applied to the rear of the wing mounting system. The ailerons were also ignored as the assumption was that the forces would all be assumed to stress the interior structure of the wing. This assumption was necessary because when applying forces in Ansys on faces, the force would be more distributed across the aileron causing a fictitious rotating moment along the length of the wing.

The initial simulation yielded a about a 27 cm or 5.4% deflection on both sides of the wing, as well as high stress points around the connections between the stringers and the ribs, as can be seen in Figure 44 and Figure 45 respectively. These high stress points are overestimated because the element size along these contact points is too large. Adding more detail to the mesh at these locations could reduce the maximum principal stress.

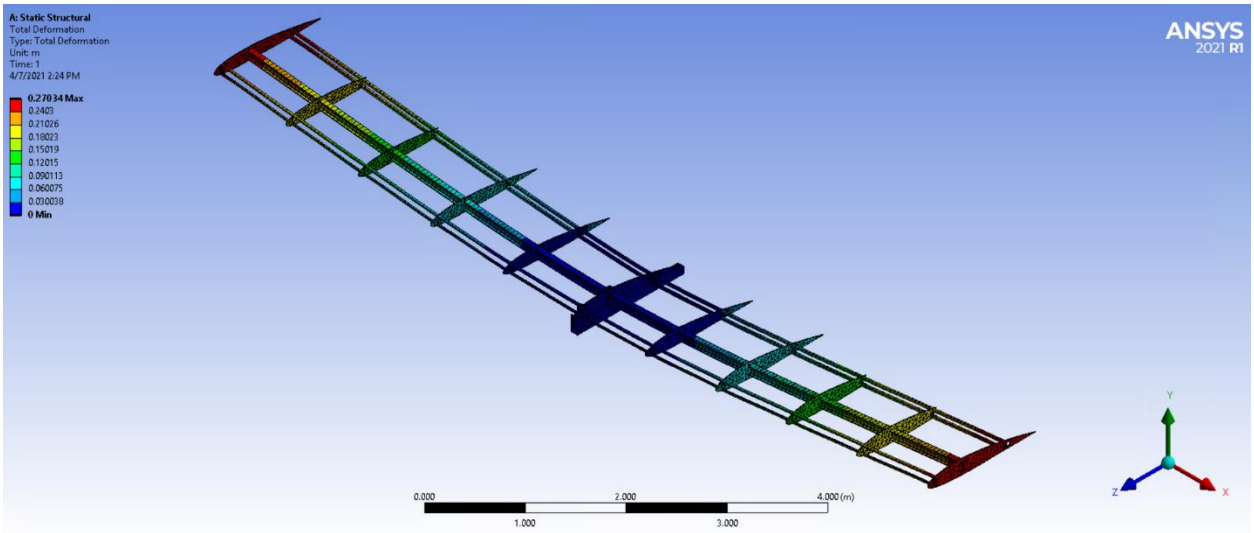

Figure 44 Deflection of Main Wing Under Steady Level Flight

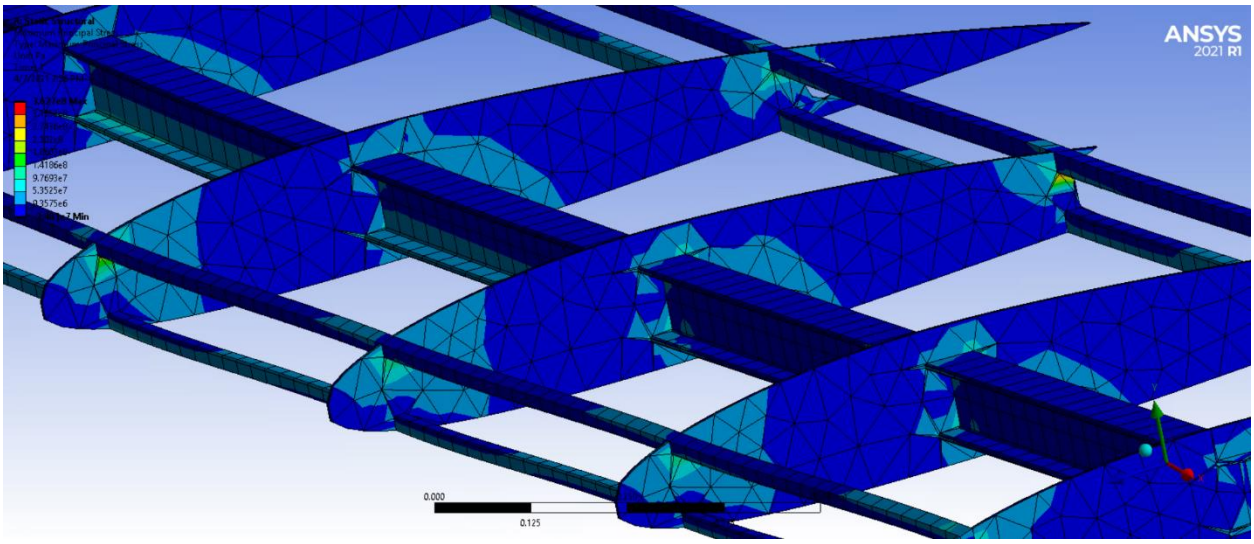

Figure 45 Stress Points along Stringers

To correct the deflection and high max principal stress, a second Main I-beam spar was added 38.1 cm rear of the first I-beam. Adding the I-beam allowed the reduction of deformation and made the deformation chordwise much more even. Considering the loss of support from suppressing the skin, another I-beam may not be necessary when compared to adding another set of stringers but testing this was outside the scope of the project.

3.9.2 Parawing Structural Simulation

Due to the flexible nature of parawings, the structural simulation will focus on strictly the fuselage, power, deployment apparatus. Two attachment points are added to the fuselage design to serve as force application points to apply the lift force of parawing to the fuselage. The drag force will be applied to the nosecone of the fuselage, the thrust force to rear of the fuselage, and gravity using inertial gravity in the mechanical simulation. The purpose being to test the structural integrity of the fuselage under the systems operating conditions.

3.10 Subscale Hang Glider Build

The build process was dictated by the scaled hang glider model SOLIDWORKS model, which can be seen in Figure 46. The design process of the aircraft began with aerodynamic analysis detailed in section 3.4.1. From there models of the wing and tail were created in SOLIDWORKS by importing scaled airfoil curves created using Excel. Individual ribs and spar parts were created and then mated together in an assembly. The parts were then revised to include attachment points for fasteners and clean up intersections. Using the scale payload model the group was able to determine the sizing of all major components that made up the overall aircraft. The group then determined the most effective combination

of electronics to achieve flight. The fuselage was then designed to house all electronic components and a $1/10^{th}$ scaled payload. The design was then iterated through different material choices including solid carbon fiber, carbon wood composite, solid foam, and foam carbon composite. Foam carbon composite was then chosen due to its high strength to weight ratio and its relative affordability. With the electronic parts list determined, bill of materials set, and the design process discussed the group was able to complete assembly of aircraft model.

Figure 46 Final Small-Scale Hang Glider Aircraft Design

3.10.1 Build Process

Based upon the beginning design specifications generated through the SOLIDWORKS model, the team developed the basis for the model build process. The process began with the team laser cutting wood blanks that were used as templates for the carbon foam core composites. Using the foam core pieces, carbon molds were then created, like what can be seen in Figure 47 and Figure 48. To create the molds the team wetted one side of the carbon sheet and laid them over the foam once epoxied. With the foam core epoxied and covered with carbon fiber, the entire sheet was then place into a vacuum bag where it was heated in order to shorten the time needed for the epoxy hardening process. A pressure gauge and valve were used to suck air out of the bag enclosing the model, ensuring a tight seal within the carbon fiber sandwich. Following the oven, the team cut and sanded each individual piece that made up the model ensuring a clean fit throughout the entire build. With all pieces cut out and sanded the team then drilled holes into both the stock material and the carbon sandwich pieces.

Figure 47 Fuselage Carbon Fiber Mold Post Vacuum

Figure 48 Wing Spares Carbon Fiber Mold in Vacuum

For the outer shell of the fuselage, the team 3-D printed components used to shape the mold. As can be seen in Figure 49, those components were assembled together to create the desired shape of the fuselage. Once conjoined, the outer surface of the 3-D mold was covered with wax to ensure a smooth removal process when the time came to separate the carbon fiber shell from the 3-D mold. For the carbon fiber, two sheets wetted in epoxy were applied to the entirety of the 3-D fuselage, which can be seen in Figure 50. Multiple sheets of carbon fiber were used in order to reduce the internal stress on the fuselage. Unlike with the carbon sandwiches that were created for both the wing and tail components of the model, the fuselage mold was place in a similar vacuum configuration but was unable to use heat during the curing process. As was discovered through trial and error, applying the heat to the fuselage shell resulted in the 3-D mold yielding and concaving in on itself. This process for creating the fuselage mold was duplicated in order to have both a right side and left side shell. Once both sides were cut and sanded, they were bolted to the internal structure comprised of the two main carbon sandwiched parts of the fuselage.

With the carbon fiber molds of the wing and tail components, as well as the fuselage shell put together overall assembly began. For the formation of the wing and tail; the carbon fiber molds were stacked on another with spacers placed throughout ensuring proper wing shaping. Two spars were run through both the entirety of the stack for the wing and tail as to add structural support. With the shape and structures of the wing set in place the exterior was covered in sailcloth. To finalize the formation of the fuselage, all components were epoxied to one another. A carbon fiber rod that ran from the center of the fuselage was used as the mounting point for the wing and tail.

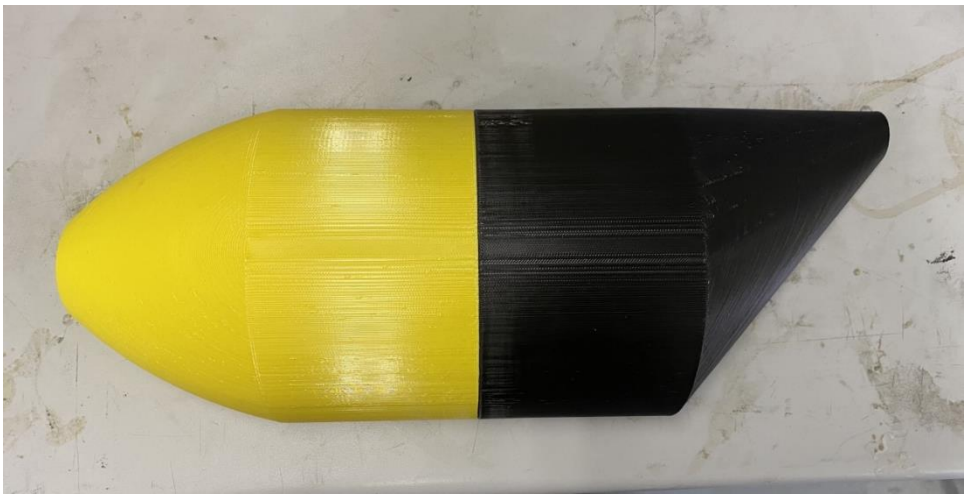

Figure 49 3-D Printed Structure Used to Shape Fuselage Mold

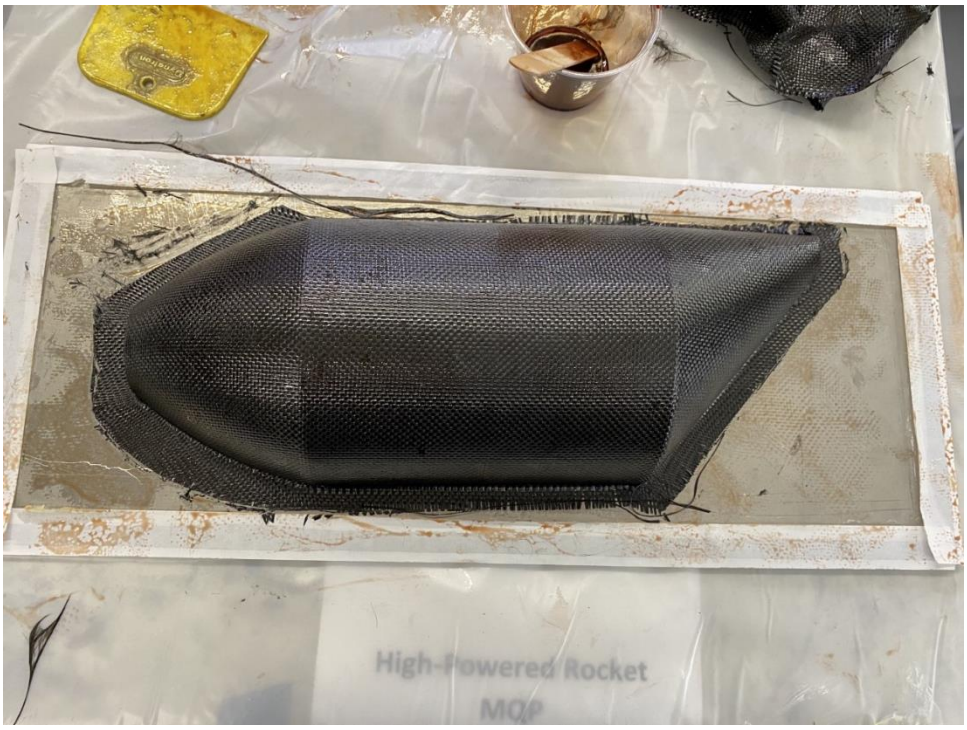

Figure 50 Carbon Fiber Layup of Fuselage Shell Before Treatment

3.10.2 Selected Electronics

Using eCal the group was able to determine the most effective combination of a controller, motor, battery cell and propellers. Based upon the calculations the group decided to go with the PROPDRIVE v2 4248 650KV Brushless Outrunner for a motor, a Rhino 4000mAh 4S 50C Lipo Battery Pack w/XT90 for the battery, the HobbyKing 50A (2~4S) ESC 4A UBEC for an electronic stability controller (ESC), the PixHawk 4 mini for the flight controller and then 2 13x8 propellers. To verify the theoretical calculations the group wired all of the different electronic components together. This process was first completed by finding the necessary connectors and cables needed to connect the power module to the flight controller. As can be seen in Figure 51, the power module, ESC, and battery were soldered together ensuring power distribution across all electronics. Through the ESC, the motor and receiver were connected; with the ESC controlling commands sent through the receiver regarding motor outputs. The motor was connected to the ESC through solder and heat shrink, as shown in Figure 52. Through all soldering and wiring the group was able to verify all theoretical calcualtions completed using eCalc. In order to gather flight data, the group connected the flight controller to the desktop program *QGroundControl* via USB. Through *QGroundControl* all flight data was uploaded to *Flight Review* where all flight data was analyzed.

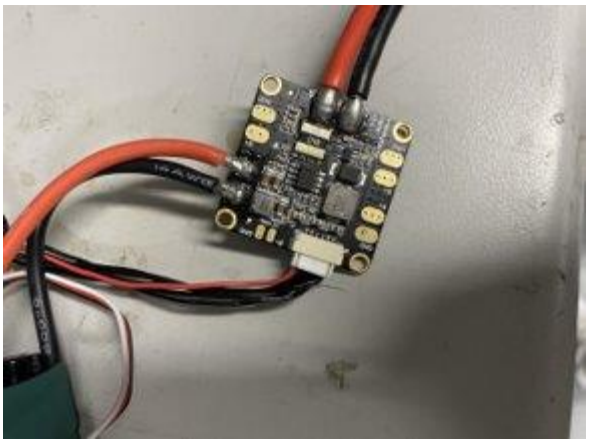

Figure 51 Soldered Power Module Connected to ESC, Flight Controller, and Battery

Figure 52 Motor Connected to ESC through Wire Connectors and Heat Shrink

4 Results

This section contains the numerical simulation and experimental results of our system designs. The experimental results section includes what would have been done if the team had time to complete the flight test portion of this project.

4.1 Numerical Simulation Results

The numerical simulation results of this paper are divided into 3 individual sections: the aerodynamic analysis results, the flight simulation analysis results, and the structural analysis results. The details of each result category are located in the subsections to follow.

4.1.1 Fixed Wing Non-Dimensional Derivatives

The results obtained from the fixed wing analyses are listed in Table 22 below. These results validate our XFLR5 data and all the coefficients in the table prove that our designed system generates enough lift and drag to perform as needed. These results are used in the further flight analysis simulations.

Table 22 Fixed-Wing Non-dimensional Derivatives

Variable	Value	Variable	Value
C_{D_1}	0.0434	C_{D_u}	0
C_{D_α}	0.1804	$C_{D_{\delta e}}$	0.0175
C_{L_1}	0.5079	C_{L_u}	0
C_{L_α}	3.1589	$C_{L_{\dot{\alpha}}}$	1.4743
C_{L_q}	4.5466	$C_{L_{\delta e}}$	0.5661
C_{m_u}	0	C_{m_α}	-1.8836
$C_{m_{\dot{\alpha}}}$	-4.6342	C_{m_q}	-14.3067
$C_{m_{\delta e}}$	-1.9058	C_{y_β}	-0.2015
C_{y_p}	-0.0223	C_{y_r}	0.2024

$C_{y_{da}}$	0	$C_{y_{dr}}$	0.1870
C_{l_β}	-0.0112	C_{l_p}	-0.0012
C_{l_r}	0.0112	$C_{l_{da}}$	0.2290
$C_{l_{dr}}$	0.0104	C_{n_β}	0.1012
C_{n_p}	-0.0523	C_{n_r}	-0.1016
$C_{n_{da}}$	0.0216	$C_{n_{dr}}$	-0.0939

4.1.2 Parawing Non-Dimensional Derivatives

The results obtained from the parawing analyses are listed in Table 23 below. These results validate our XFLR5 data and all the coefficients in the table prove that our designed system generates enough lift and drag to perform as needed. These results are used in the further flight analysis simulations.

Table 23 Parawing Aircraft Non-dimensional Derivatives

Variable	Value	Variable	Value
C_{D_1}	0.0441	C_{D_u}	0
C_{D_α}	0.6704	C_{D_δ}	0.0734
C_{L_1}	0.5215	C_{L_u}	0
C_{L_α}	3.2340	$C_{L_{\dot{\alpha}}}$	0
C_{L_q}	2.1135	C_{L_δ}	0.2342
C_{m_u}	0	C_{m_α}	-0.04
$C_{m_{\dot{\alpha}}}$	0	C_{m_q}	-1.5212
C_{m_δ}	-0.0930	C_{y_β}	-0.0802

C_{y_p}	-0.1775	C_{y_r}	0.0365
C_{y_δ}	-0.0098	C_{l_β}	-0.1440
C_{l_p}	0.3704	C_{l_r}	-0.0657
C_{l_δ}	0.0330	C_{n_β}	0.0252
C_{n_p}	0.0602	C_{n_r}	0.0100
C_{n_δ}	-0.0066		

4.1.3 Fixed Wing Controlled Simulations

Using the non-dimensional derivatives tabulated in the previous sections, the dimensional derivatives for the fixed wing were calculated and used to develop linear quadratic regulator (LQR) controllers to guide the aerial delivery vehicles along the desired trajectories. There were 6 legs of flight in the trajectory, and each leg of flight required 2 controllers: one for lateral motion and one for longitudinal motion. The lateral controllers made use of the aileron and rudder deflections, and the longitudinal controllers used the elevator deflection. The gain matrices for the fixed wing aircraft are tabulated in Appendix 7.3 (longitudinal) and Appendix 7.4 (lateral).

To evaluate the effectiveness of the controllers, Simulink was used to test the small disturbance response of the closed loop system. The block diagram for the longitudinal response of the fixed wing can be seen in Figure 53 below.

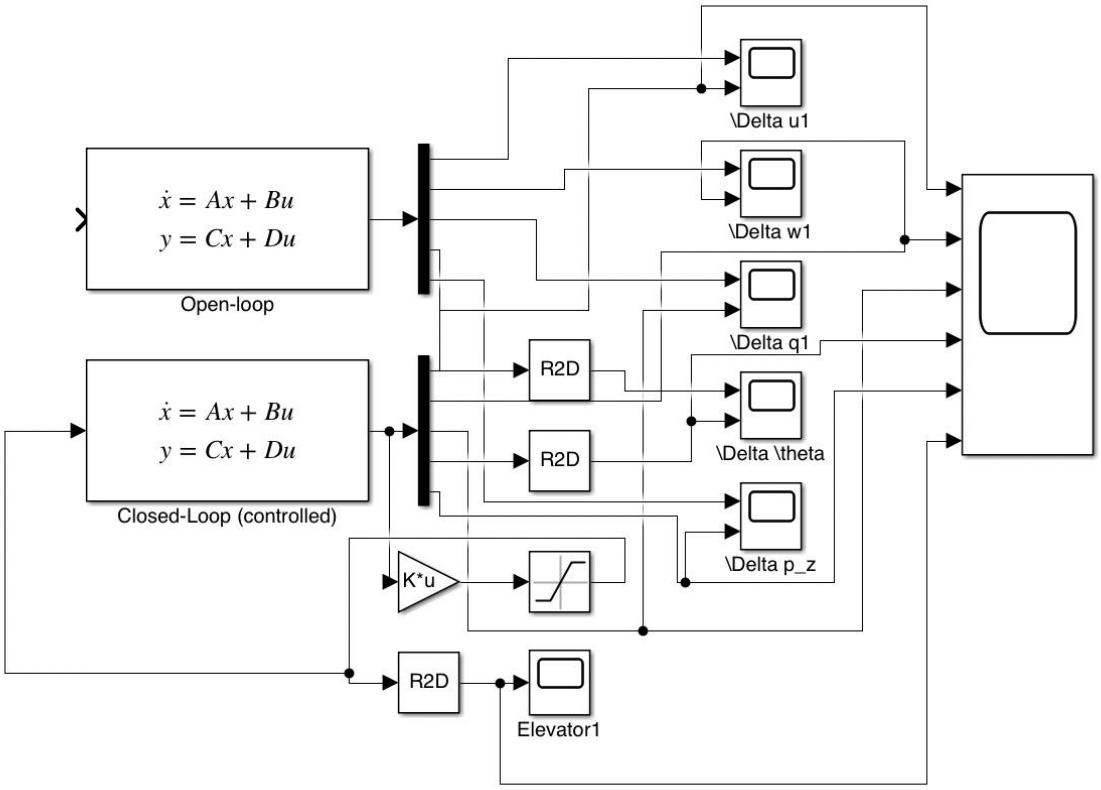

Figure 53: Simulink Block Diagram for Fixed Wing Longitudinal Motion

Using this block model, the standard parameters associated with longitudinal motion were evaluated after being disturbed from their trim state for each leg of flight. The position in the x-direction was omitted from this block diagram because it had no effect on the aircraft's deviation from the desired trajectory. Additionally, saturation limits were imposed on the elevator deflection to ensure that it was an accurate representation of what the aircraft was capable on. A typical elevator on any fixed wing aircraft can deflect a maximum of +28 degrees and a minimum of -20 degrees, so the saturation limits were set at such. The Simulink block diagram for the lateral state variables was similar to the longitudinal model, except the lateral model required two control inputs to include for the aileron and the rudder. Saturation limits for the aileron were set to +30 degrees and -15 degrees, while the limits for the rudder were set to 26 degrees in either direction. The block diagram for the lateral model is shown in Figure 54.

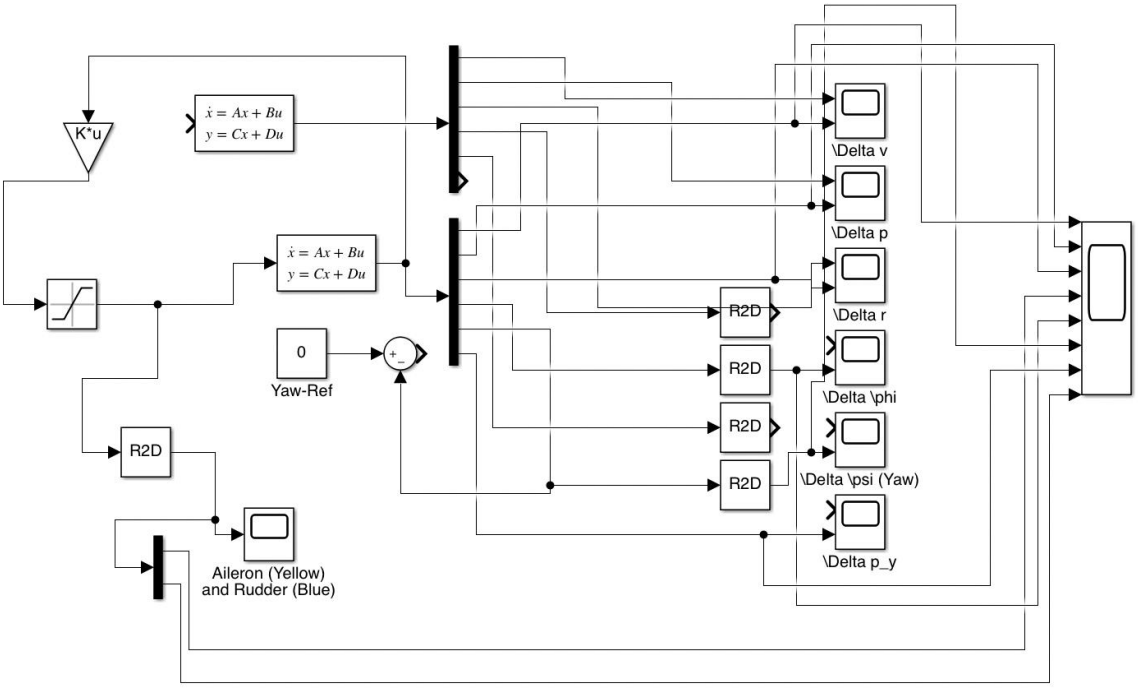

Figure 54: Simulink Block Diagram for Fixed Wing Lateral Motion

Using these block diagrams, the uncontrolled motion of the fixed wing was plotted. The resulting graphs showed that the uncontrolled small disturbance response never settled; instead, the values of the state variables exponentially increased. This led us to investigate the uncontrolled eigenvalues for each leg of flight, which contained positive real parts in some instances. This meant that the fixed wing aircraft, although statically stable, lacked dynamic stability. Consequently, it became difficult to settle all the state variables at the same time. In an effort to produce the best results, the team decided to settle most state variables as quickly as possible, and other less time-sensitive variables slightly slower. Considering the duration of the flight path is upwards of several hours, the altitude and the y-position were determined to be the least essential states. By settling these two states over the span of several minutes, the Euler angles, Euler angle rates, and body-fixed velocities were capable of settling within seconds of the proposed disturbance. The simulation graphs produced for both the longitudinal and lateral states during the initial climb leg of the trajectory are shown in Figure 55 and Figure 56 below. In these figures, it is demonstrated that the controller is able to settle most of the state variables within 15-20 seconds for longitudinal motion, and within 5-10 seconds for lateral motion. Although the y-position and z-position appear to not settle, they slowly tend towards 0. The rest of the fixed wing small disturbance responses are located in Appendices 7.5 through 7.16.

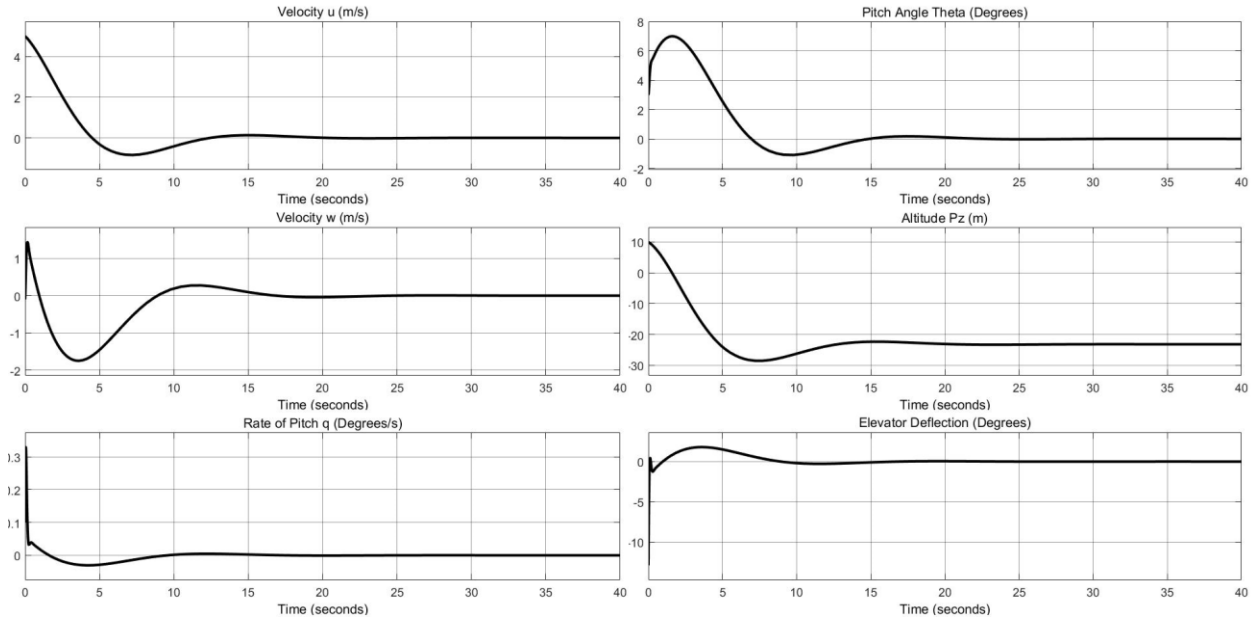

Figure 55: Small Disturbance Response - Fixed Wing Initial Climb (Longitudinal)

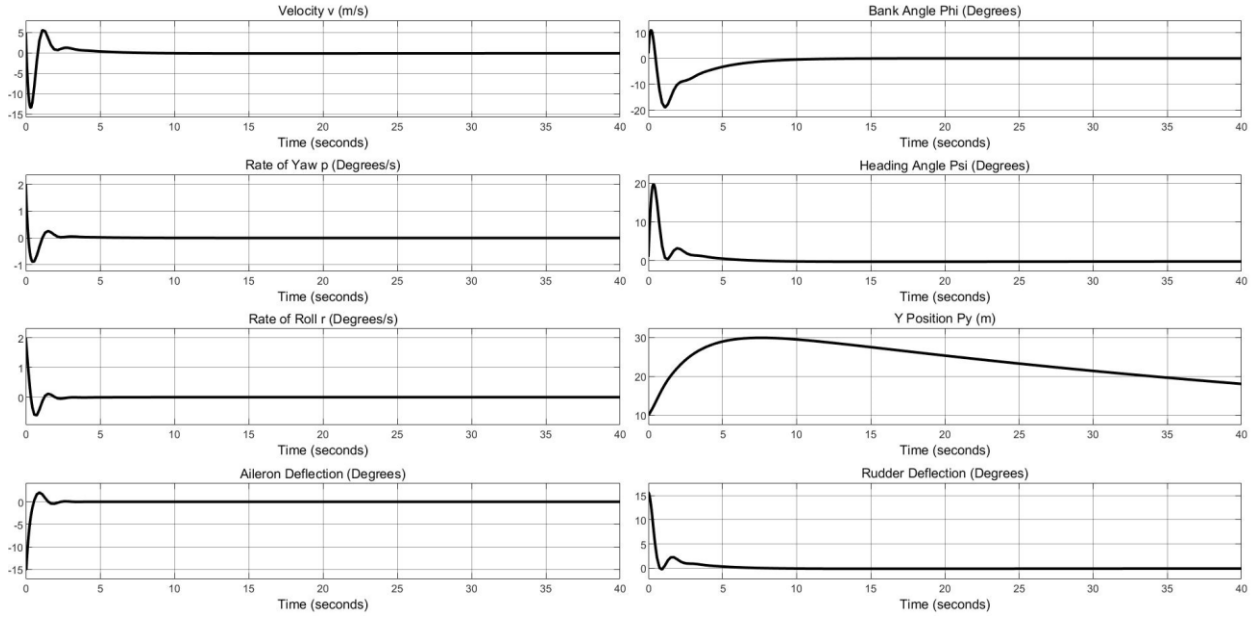

Figure 56: Small Disturbance Response - Fixed Wing Initial Climb (Lateral)

In addition to the small disturbance responses in Simulink, the versatility of the controllers was further investigated through wind disturbance simulations in MATLAB. To represent a wind threat field, constant wind velocities were randomly generated based on a normal distribution every 30 seconds using the build in modulus command. The body fixed velocities of the aircraft were adjusted based on the random wind, and the closed loop response of the system was simulated over a time span of 5 minutes. The resulting

positions, velocities, Euler angles, and angle rates are shown in Figure 57 through Figure 60 These graphs demonstrate the controller's ability to respond the random disturbances and settle before the next disturbance occurs. These graphs are also located in Appendix 7.17

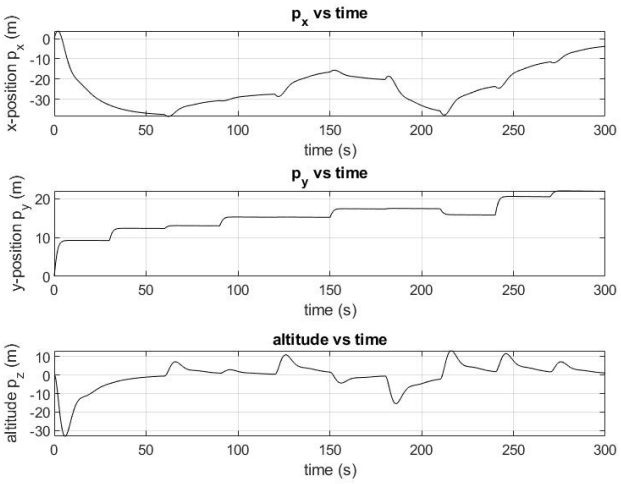

Figure 57 Linear Position Aircraft Response with Wind Disturbance

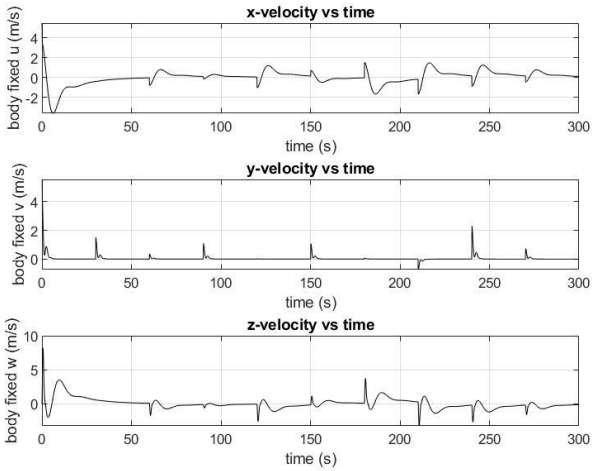

Figure 58 Linear Velocity Aircraft Response with Wind Disturbance

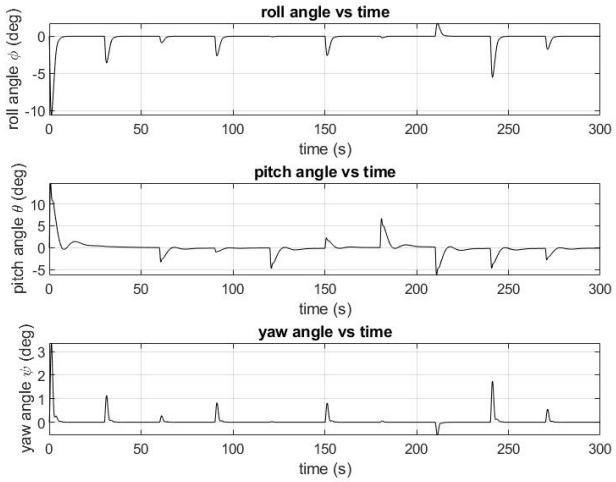

Figure 59 Angular Position Aircraft Response with Wind Disturbance

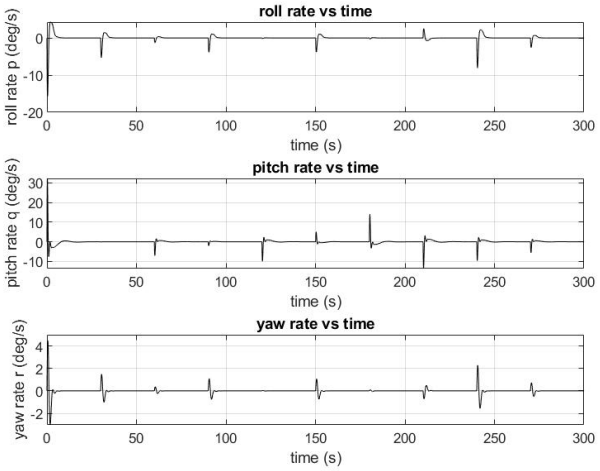

Figure 60 Angular Velocity Aircraft Response with Wind Disturbance

Finally, it was determined that to fly the full trajectory, the fixed wing aircraft would burn a total of approximately 133 kilograms of fuel. The amount of fuel used during each leg of flight is tabulated below.

Table 24 Fuel Expenditure during Various Legs of Flight (Fixed-Wing)

Leg of Flight	Fuel Required
Climb 1 (Out)	14.3717 kg
Cruise 1 (Out)	46.1293 kg
Helix (Payload Delivery)	16.8875 kg
Climb 2 (Back)	12.4508 kg
Cruise 2 (Back)	40.3004 kg
Descent (Land)	2.7648 kg
Total for all legs:	132.9045 kg

4.1.4 Parawing Controlled Simulations

Simulations for the parawing aircraft generally followed the same procedure as the simulations for the fixed wing aircraft, but with different values for stability and controls derivatives as well as different moments of inertia. In a standard parawing, the lateral motion is controlled using the asymmetric deflection of the canopy, while the longitudinal motion is controlled by the symmetric deflection of the canopy. However, only the longitudinal motion of our aircraft was controlled via symmetric deflection; the lateral motion and asymmetric deflection were left uncontrolled. Upon analyzing the uncontrolled eigenvalues of our model, it was determined that the system's lateral dynamic instability was substantial – having only one negative real part (stable) eigenvalue, and positive eigenvalues with values upwards of 30 for most flight scenarios. In order to fully settle the lateral states, the control input (asymmetric deflection) needed to be in the order of magnitude of 10^2 degrees. Due to this, the lateral motion of the parawing was considered uncontrollable, especially given the control input saturation limits we imposed on the model. The uncontrollable nature of the parawing was likely due to the method through which the stability and control derivatives were found. The wing used to find these derivatives was not the wing designed by the team, so the derivatives were not completely accurate to the wing designed by the team. This likely led to the instability found in the simulations when the derivatives were applied to the team's wing; the instability is not likely due to the shape of the wing itself. The reason the team does not believe the wing geometry to be at fault is because it was based on a commercially available paraglider which has stable flight

characteristics. In addition to the substantial lateral instability, the eigenvalues for the longitudinal motion were also slightly unstable, but to a much lesser extent, so the system's longitudinal states could still be effectively controlled. Therefore, only the symmetric deflection was used to control the longitudinal motion of the parawing, resulting in 6 gains matrices. The gain matrices for the parawing aircraft are tabulated in Appendix 7.18.

Similar to the controller validation done for the fixed wing model, Simulink was used to test the small disturbance response of the closed loop system and evaluate the accuracy and effectiveness of the gain matrices. The position in the x-direction was again omitted from this block diagram because it had no effect on the parawing's deviation from the desired trajectory. Additionally, saturation limits were induced on the symmetric deflection control input to reflect the capabilities of the parawing more accurately. Although there is limited data regarding the deflection capabilities of parafoils and parawings, the team proceeded with saturation limits of 20 degrees in both the positive and negative directions because it was a reasonable value in comparison to several parafoil simulation data sets. The block diagram for the longitudinal response of the parawing can be seen in Figure 61 below.

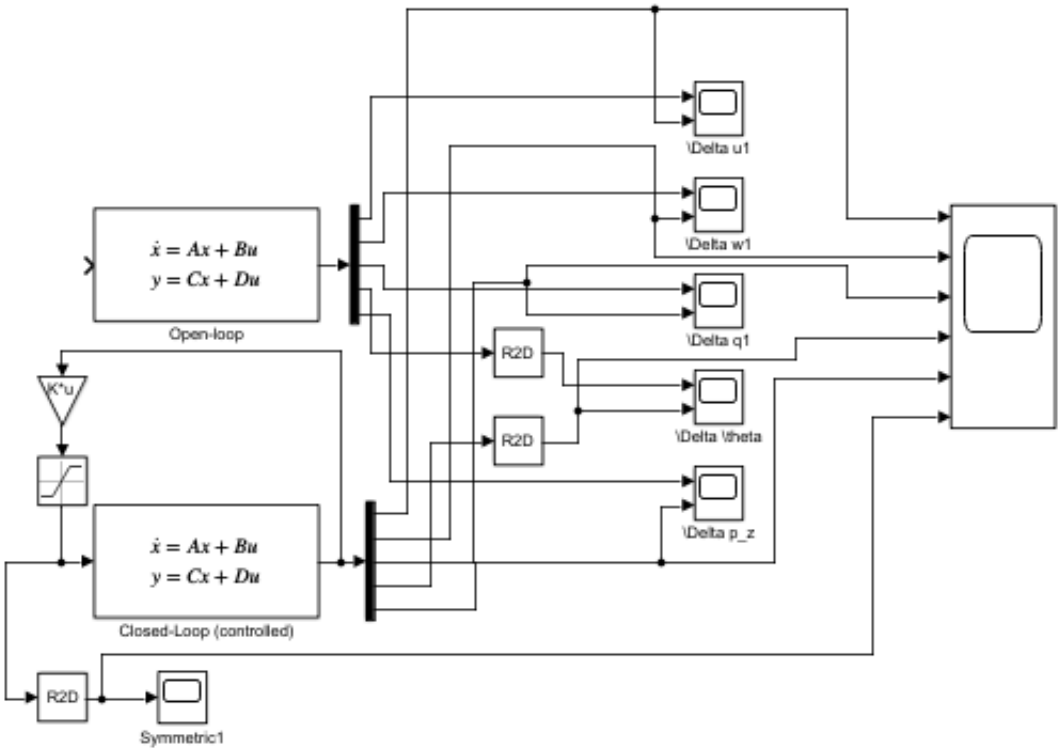

Figure 61: Simulink Block Diagram for Parawing Longitudinal Motion

Due to the fact that the longitudinal states were slightly unstable, settling all states at the same rate was not the most suitable method of control. Instead, the team decided to settle most state variables as quickly as possible, and other less time-sensitive variables slightly slower, similar to what was done for the fixed wing controllers. The altitude (p_z) was the state chosen to settle less quickly than the others because the duration of the flight path is upwards of several hours, so the altitude will have plenty of time to correct itself with the slightly slower controller. By settling the altitude over the span of several minutes, the Euler angles, Euler angle rates, and body-fixed velocities were settled within seconds of the proposed disturbance. The simulation graphs produced for the longitudinal states during the initial climb leg of the trajectory are shown in Figure 62 below. In these figures, it is demonstrated that the controller is able to settle most of the state variables within 10-20 seconds. Although the z-position appears to not settle, it slowly tends towards 0. The rest of the parawing small disturbance responses are located in Appendices 7.19 through 7.24.

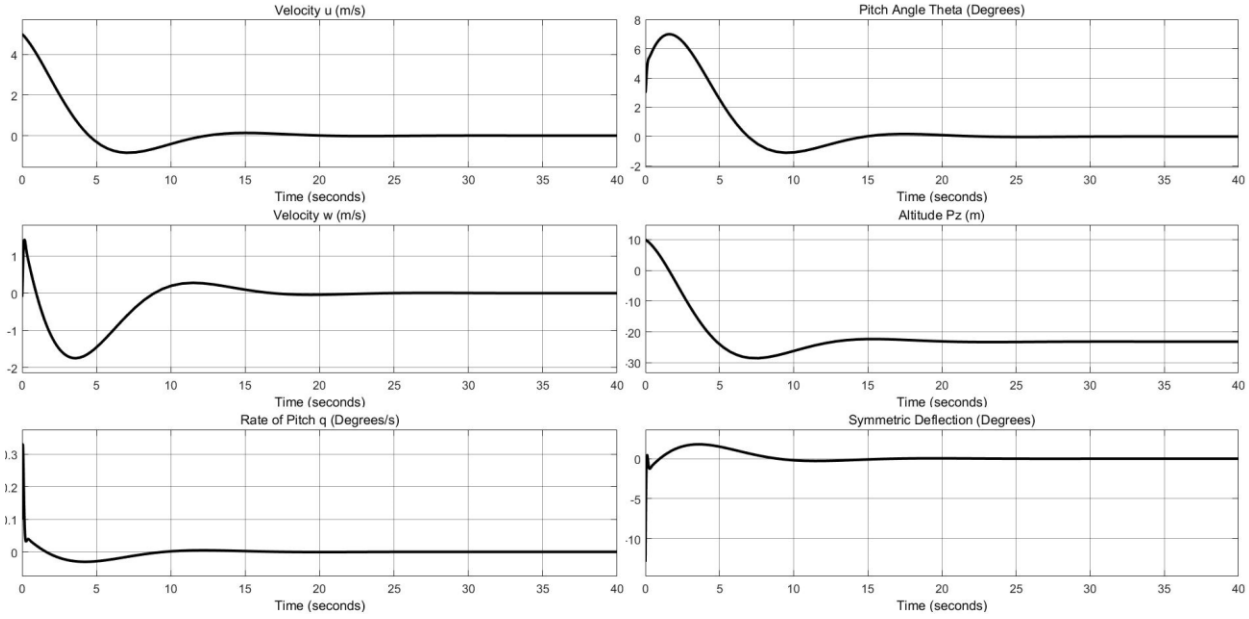

Figure 62: Small Disturbance Response - Parawing Initial Climb (Longitudinal)

Unlike the procedure followed for the fixed wing aircraft, the parawing was not simulated in the wind threat generation model due to its uncontrolled lateral motion. The wind model uses longitudinal and lateral motion in conjunction with one another to represent the full state space model throughout different time instances when subjected to random wind disturbances. However, since the lateral motion was completely uncontrolled, the wind model simulation does not yield meaningful results to represent how the entire system would respond to random disturbances over time (i.e., the system will never settle).

Despite the lack of lateral control, the fuel consumption for each leg of flight was still calculated. It is important to note that these calculations are contingent upon the functionality of both the longitudinal and lateral controllers to ensure that the parawing does not deviate from the generated trajectory. Operating under this assumption, it was determined that to fly the full trajectory, the parawing would burn a total of approximately 30 kilograms of fuel. This is over a 75% reduction in fuel consumption when compared to the fuel consumption of the fixed wing aircraft. The amount of fuel used during each leg of flight is tabulated below.

Table 25 Fuel Expenditure during Various Legs of Flight (Parawing)

Leg of Flight	**Fuel Required**
Climb 1 (Out)	2.9602 kg
Cruise 1 (Out)	10.0690 kg
Helix (Payload Delivery)	3.6066 kg
Climb 2 (Back)	2.6640 kg
Cruise 2 (Back)	9.5508 kg
Descent (Land)	0.7389 kg
Total for all legs:	29.5895 kg

4.1.5 Structural Simulations Results

The results of the final simulation can be seen in Figure 63. The deformation slightly under 20 cm is just under 4% deformation which is within an acceptable range of 3-5% according to [55]. Additionally, the maximum principal stress is below the listed maximum ultimate stress of the material by a factor of 100. This is an overestimation of the deformation and stress considering the loss of support from suppressing the skin. This shows that the wing is capable of sustaining steady level flight.

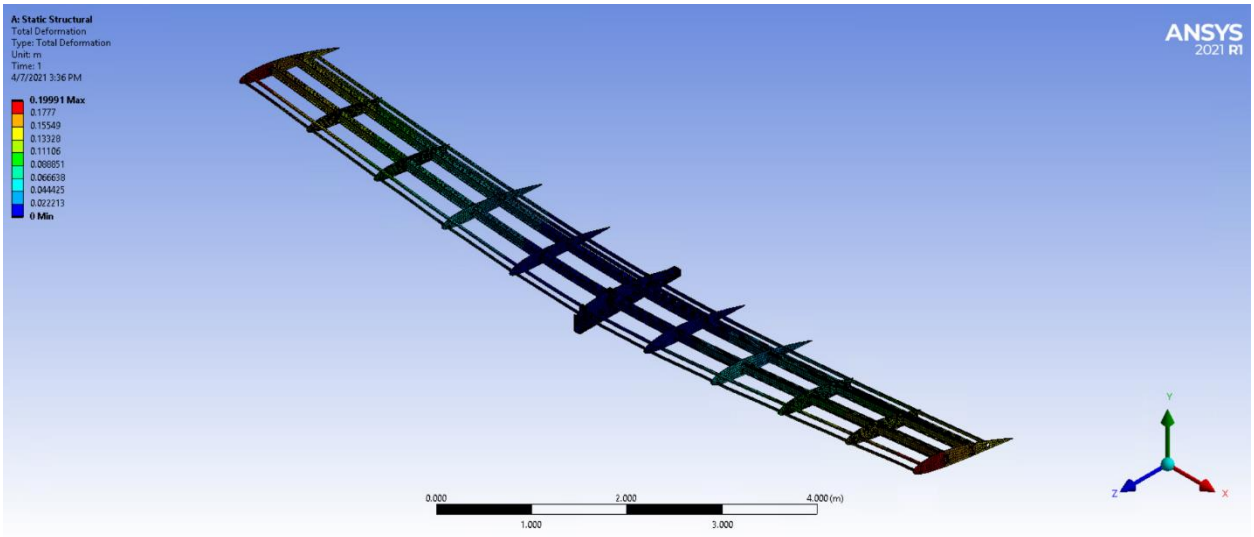

Figure 63 Fixed-Wing main wing Final Deformation under Cruise Conditions

4.2 Experimental Results

Due to the restrictions imposed by COVID 19 the team we unable to complete the build process in time to get results. However, we did devise a series of tests for the completed subscale model in order to get a baseline for performance. The first of which is the glide test. For the test the Plane will be thrown and using the IMU and GPS on the Pixhawk 4 the performance will be tracked and compared to predicted performance values. Next is the climb rate test in which the plane will take off under engine power and climb at different angles while the rate of climb is recorded by the IMU. Next is the circle of turn test where the plane will take off under engine power and turn at different angles while the GPS position is recorded by the IMU. The flight duration test is then performed where the plane will take off under engine power and fly until power is exhausted. The GPS position is recorded by the IMU and the total distance traveled is calculated. Finally, the simulated mission test is conducted where the plane will take off under engine power and proceed to half the max distance found in the duration test. The Plane will then drop the simulated payload. Afterwards the plane will return to its takeoff point and land. All data acquired throughout the test period will be uploaded to *QGroundControlI* where all of the acquired data will be converted into interpretive charts using *Flight Review*.

5 Conclusions

The goal of this project was to design and analyze autonomous aerial delivery vehicle concepts with terrestrial launch and/or aerial deployment capabilities as well as increased range and accuracy compared to the state of the art. The design requirements given to us by our sponsor, DEVCOM SC, detailed a PADS that could launch from the ground, carry 100-200 kg of cargo to destinations 200-500 km away, and then return to either the launch location or a secondary location at a comparable distance. The final location of the supply drop was required to be less than 100m from the desired location. After launch, the system needed to be capable of autonomous guidance to the destination with the possibility of encountering wind threat fields along its path. To accommodate to these design requirements, the team planned to create 3 distinct aerial delivery model: a fixed wing aircraft, a parawing, and a hang glider. When choosing these designs, it was intended for simulations and numerical analysis to be performed for both the fixed wing and parawing, and the small-scale model of the hang glider was meant to be physically constructed.

To choose these three final designs, a design space exploration was conducted using both low and medium fidelity computational models and simulations developed using MATLAB and XFLR5 to narrow down potential design options. After the three designs with the highest rankings were selected, several sizing iterations and calculations were completed for each design in order to ensure that they were statically stable and feasible for further development. Additionally, computer-aided design (CAD) assemblies were created using SOLIDWORKS for all three designs. The fixed wing and parawing CAD models allowed for aerodynamics and structural analyses as well as high fidelity flight simulations. For aerodynamic analysis, computational fluid dynamics simulations were developed using Fluent to determine non-dimensional stability and control derivatives and lift and drag coefficients at different angles of attack. For structural analysis, Ansys simulations were developed to measure stress and displacement of the wing and wing mounting under the conditions of lift, drag, thrust, and gravity, and to analyze the structural integrity of the same two designs. To simulate the flight of the fixed-wing and parawing designs, trajectories were generated for different phases of flight (i.e., climb, cruise, etc). These trajectories are used to find trim conditions that lead to linearized flight dynamical models. Linear quadratic regulator (LQR) autopilot controllers were designed to control airspeed, altitude, climb angle, and heading angle. The closed-loop responses of the aircraft under autopilot control were tested using MATLAB and Simulink and implemented within a wind gust model. Finally, the hang-glider CAD model was physically assembled on a 1-10 scale using a foam-carbon composite. Small scale testing was intended to be completed to analyze performance characteristics for various phases of flight, but due to time constraints this was not fully executed.

From our results and our historical analysis of fixed wings and parawings, the following benefits were found for each system. The parawing excels in scenarios where cost is the main limiting factor whereas the fixed wing excels when time is the limiting factor. The parawing is a lightweight, easily packable system. This means it costs less to transport the parawing system to a base compared to a fixed wing. It also uses less fuel, an approximately 75% fuel reduction between our parawing and fixed wing. A parawing also costs less to manufacture since the design lacks structural supports. The fixed wing on the other hand is significantly heavier and requires more expensive materials to construct. We studied the use of carbon fiber in fixed wing aircraft construction, which is an expensive material to work with. There are other options, but the shear amount of mass needed for a fixed wing design makes it more expensive. The fixed wing was able to complete the trajectory given significantly faster than the parawing. Our fixed wing design completed our trajectory in approximately 6 hours where the parawing completed it in approximately 16 hours. Finally, parawings are more susceptible to wind than a fixed wing. Fixed wings are more stable, particularly laterally, than parawings making autonomous control schemes easier to implement.

In the process of conducting the trade-off study and executing this project, our team learned a few lessons that would be beneficial for follow-on projects. The first thing we learned in hindsight was that it took all of A Term and part of B Term to understand the focus of the project, including what the end result should be and exactly what was expected of us. It would have been helpful and efficient if we were able to figure this out before the end of A Term so we could get into the design steps quicker. We also learned that more time should have been left to fully conduct the necessary design iterations before we began the next steps in the project. We did not leave time for iterations, and therefore ended up with dynamically unstable designs that we had to change, causing us to course correct throughout the project. We learned that meshing requires CAD knowledge, and Fluent and Ansys were required to simulate computational fluid dynamic simulations of our models. We should have had someone who knew how to use CAD on the structures team or had introduction to CAD listed as a required course for someone on the team. Similarly with Fluent, there were no experts on the software that we could reference at WPI, which made it difficult when learning a new software. Those who were required to use Ansys and Fluent should have had a required course to complete beforehand and should have a list of people they can reference if they have questions. Another thing we learned was that orthotropic materials yield complications in structural simulations, making it difficult to simulate two out of our three designs. This MQP was ambitious, even for eight students, and we have learned that attempting to simulate a complex design like an entire aircraft, while simultaneously developing two other distinct designs and creating high fidelity flight simulations for them is beyond the scope of one MQP, or at least requires a larger team than we had available.

5.1 Recommendations for Future Work

In general, future work for this project should include iterating the current parawing and fixed wing designs to produce dynamically stable aircrafts. This will enable the implementation of more effective controllers as well as reduce the risk of failure due to possible disturbances along the flight path (such as large gusts of wind). More specific recommendations can be found in the subsections to follow.

5.1.1 Future Aerodynamic Analysis

Future project can expand upon the aerodynamic procedures performed in this paper in order to get more accurate measures of all aerodynamic coefficients for their designs. This can be accomplished in two ways for both the fixed wing aircraft and the parawing. The first would be to use dynamic CFD simulations to estimate the aerodynamic parameters more accurately as opposed to the equations-based method or pulling the values from other papers as was done in this project. Additionally, scale models could be created to be tested in a wind tunnel to validate those numerical results.

For the parawing, in addition to utilizing the two techniques listed above for the fixed wing, a more accurate representation of the parawing could be used. The parawing used in this project was a flat wing which was much smaller than the teams designed wing. The coefficients for this flat wing were then applied to the designed wing shape and assumed they were still valid. Future projects could test the airfoil on the actual parawing shape as well as adding holes to the parawing to more accurately simulate the parawing's behavior.

5.1.2 Future Flight Simulation and Control

For the simulation and control aspect of this project, additional trajectories can be created and controlled by implementing different combinations of the current legs of flight, or by creating new legs of flight entirely (such as a varying altitude leg of flight or a special descent pattern). Along the same lines, optimal trajectories may be created using optimal control laws and theories, and the cost functional to be minimized can resemble the ranking equation created in section 3.1.2 of this report. In order to ensure that the controllers are fully functional along these trajectories, trajectory tracking as well as payload tracking can also be implemented. Payload tracking can be used to further adhere to the original design requirements, keeping the CEP within 100 meters.

Additionally, since a linearized model was used for trajectory generation, control generation, and small disturbance response testing, another possible aspect of future work could include the re-implementation of the controlled flight path in a non-linearized model to produce more accurate results. The non-linearized model makes far less assumptions but required a much more detailed analysis to determine the values of the variables required for the A and B matrices. In terms of the wind disturbance

simulations, future work may include deriving a more accurate wind gust model or determining how to implement the black box wind gust transfer function that MathWorks provides in the form of a Simulink block. Any one or combination of these suggestions will yield results that more accurately represent real world conditions and scenarios.

5.1.3 Future Structural Analysis

Future projects can take structural analysis in many directions. The structural analysis of this project focused solely on the structural stability of the interior support structures of the main wing of the fixed-wing design. A future project can build on this by working to incorporate the skin of the wing. Additionally, exploring the other parts of the aircraft such as the fuselage and the tail structure would also yield useful information. To do this, estimations would need to be made about how the aerodynamic forces would affect just that part of the aircraft. A more ambitious goal would be to attempt to run a whole aircraft structural simulation. This type of simulation is extremely complex and will take an extensive amount of research and troubleshooting as structural simulations of this magnitude are extremely difficult to set up and extensively time-consuming in both running and troubleshooting.

Additionally, Ansys structural can be linked with results from Ansys Fluent to produce simulations that use actual imported aerodynamic forces from Fluent. This can allow for not only higher fidelity simulations, but also an easier iterative process such that the structure of the wing is not limited to one aerodynamic design. For potential future projects, this would allow for an easier workflow, where the structural design is included in the iterative process.

5.1.4 Future Subscale Evaluation

Future projects can take the different unforeseen issues that the team found themselves facing and develop a design and build process that prevent against them from occurring. Although no experimental results came from the build of the subscale model, a future team could run test to evaluate the performance of the subscale hang glider subscale design in order to test the performance and success of the design. Given more time it could also be an interesting goal to have a future teamwork towards building the other two models at a subscale level in order to determine which of the three models perform at a higher level outside of just electronic simulations. A future project could make more use of additive manufacturing in order to speed up the build process, rather than choosing to make a majority of the design on their own. Using pre-impregnated carbon fiber could also speed up the build process in the future drastically, although future teams would need to take into consideration the added costs when dealing with that type of material.

6 Bibliography

[1] J. A. N. Eaton, “Point of Impact: Delivering Mission Essential Supplies to the Warfighter through the Joint Precision Airdrop System.”

[2] S. Dunker, J. Huisken, D. Montague, and J. Barber, “Guided Parafoil High Altitude Research (GPHAR) Flight at 57,122 ft,” Apr. 2015, doi: 10.2514/6.2015-2121.

[3] K. M. Klinkmueller *et al.*, “Airborne delivery of unmanned aerial vehicles via joint precision airdrop systems,” *AIAA Scitech 2019 Forum*, no. January, pp. 1–13, 2019, doi: 10.2514/6.2019-2285.

[4] J. S. Haller, T. D. Fields, and O. A. Yakimenko, “Precision aerial delivery with a steerable cruciform parachute,” 2017, doi: 10.2514/6.2017-3539.

[5] D. C. Meier, “Application of Satellite-Derived Wind Profiles to Joint Precision Airdrop System (JPADS) Operations,” 2010. [Online]. Available: https://scholar.afit.edu/etd/2171.

[6] O. A. Yakimenko and A. I. of A. and Astronautics. Staff, *Precision Aerial Delivery Systems.* American Institute of Aeronautics and Astronautics, 2015.

[7] H. Gao *et al.*, “In-flight wind field identification and prediction of parafoil systems,” *Applied Sciences (Switzerland)*, vol. 10, no. 6, Mar. 2020, doi: 10.3390/app10061958.

[8] N. Slegers and M. Costello, “Aspects of Control for a Parafoil and Payload System.” [Online]. Available: https://digitalcommons.georgefox.edu/mece_fac.

[9] E. Scheuermann, M. Ward, M. R. Cacan, and M. Costello, “Combined lateral and longitudinal control of parafoils using upper-surface canopy spoilers,” *Journal of Guidance, Control, and Dynamics*, vol. 38, no. 11, pp. 2122–2131, 2015, doi: 10.2514/1.G000892.

[10] B. le Floch, J. P. How, M. Stoeckle, and L. Breger, “Trajectory planning for autonomous parafoils in complex terrain,” 2017, doi: 10.2514/6.2017-3220.

[11] J. Barber and J. McGrath, “Status report on the development and testing of single surface gliding cargo airdrop systems,” 2003, doi: 10.2514/6.2003-2123.

[12] C. P. Gibson, “Powered paraglider longitudinal dynamic modeling and experimentation,” 2016.

[13] E. Niewiadomska-Szynkiewicz and A. Sikora, “Progress in Automation, Robotics and Measuring Techniques,” *Advances in Intelligent Systems and Computing*, vol. 351, pp. 181–190, 2015, doi: 10.1007/978-3-319-15847-1.

[14] J. O. Choi and D. B. Kim, “A new UAV-based module lifting and transporting method: Advantages and challenges,” in *Proceedings of the 36th International Symposium on Automation and Robotics in Construction, ISARC 2019*, 2019, pp. 645–650, doi: 10.22260/isarc2019/0086.

[15] M. Becker and D. Sheffler, “Designing a high speed, stealthy, and payload-focused VTOL UAV,” *2016 IEEE Systems and Information Engineering Design Symposium, SIEDS 2016*, pp. 176–180, 2016, doi: 10.1109/SIEDS.2016.7489294.

[16] V. Devalla and O. Prakash, “Developments in unmanned powered parachute aerial vehicle: A review,” *IEEE Aerospace and Electronic Systems Magazine*, vol. 29, no. 11, pp. 6–20, 2014, doi: 10.1109/MAES.2014.130173.

[17] A. S. Puranik, “Dynamic modeling, simulation and control design of a parafoil-Dynamic modeling, simulation and control design of a parafoil-payload system for ship launched aerial delivery system (SLADS) payload system for ship launched aerial delivery system (SLADS),” 2011. [Online]. Available: https://digitalcommons.mtu.edu/etds.

[18] L. W. Traub and S. Okayama, “Investigation of a Morphable Parawing for Unmanned Aerial Vehicle Application,” *Journal of Aircraft*, vol. 55, no. 3, pp. 1217–1230, 2018, doi: 10.2514/1.C034557.

[19] J. Jacob and S. Smith, “Design Limitations of Deployable Wings for Small Low Altitude UAVs,” in *47th AIAA Aerospace Sciences Meeting including The New Horizons Forum and Aerospace Exposition*, American Institute of Aeronautics and Astronautics, 2009.

[20] L. W. Traub and S. Okayama, “Investigation of a Morphable Parawing for Unmanned Aerial Vehicle Application,” *Journal of Aircraft*, vol. 55, no. 3, pp. 1217–1230, 2018, doi: 10.2514/1.C034557.

[21] J. Tao *et al.*, “Modeling and control of a powered parafoil in wind and rain environments,” *IEEE Transactions on Aerospace and Electronic Systems*, vol. 53, no. 4, pp. 1642–1659, Aug. 2017, doi: 10.1109/TAES.2017.2667838.

[22] United States Army, “Reduced Signature Powered Parafoils,” Accessed: Oct. 24, 2020. [Online]. Available: https://www.sbir.gov/node/1654431.

[23] S. C. Crosbie, M. D. Polanka, P. J. Litke, and J. L. Hoke, “Increasing reliability of a two-stroke internal combustion engine for dynamically changing altitudes,” in *Journal of Propulsion and Power*, 2014, vol. 30, no. 1, pp. 87–95, doi: 10.2514/1.B34753.

[24] A. P. Kelley, “Dynamics of Expanding Flames,” 2011.

[25] T. H. Bradley, B. A. Moffitt, T. F. Fuller, D. N. Mavris, and D. E. Parekh, “Comparison of design methods for fuel-cell-powered unmanned aerial vehicles,” *Journal of Aircraft*, vol. 46, no. 6, pp. 1945–1956, 2009, doi: 10.2514/1.41658.

[26] K. E. Swider-Lyons, J. A. Mackrell, J. A. Rodgers, G. S. Page, M. Schuette, and R. O. Stroman, “Hydrogen Fuel Cell Propulsion for Long Endurance Small UAVs,” 2011.

[27] P. Oettershagen *et al.*, “Design of small hand-launched solar-powered UAVs: From concept study to a multi-day world endurance record flight,” *Journal of Field Robotics*, vol. 34, no. 7, pp. 1352–1377, Oct. 2017, doi: 10.1002/rob.21717.

[28] S. Morton, R. D’Sa, and N. Papanikolopoulos, “Solar powered UAV: Design and experiments,” Sep. 2015, doi: 10.1109/IROS.2015.7353711.

[29] A. G. Escobar-Ruiz, O. Lopez-Botello, L. Reyes-Osorio, P. Zambrano-Robledo, L. Amezquita-Brooks, and O. Garcia-Salazar, “Conceptual Design of an Unmanned Fixed-Wing Aerial Vehicle Based on Alternative Energy,” *International Journal of Aerospace Engineering*, vol. 2019, 2019, doi: 10.1155/2019/8104927.

[30] K. P. Valavanis and G. J. Vachtsevanos, *Handbook of unmanned aerial vehicles*. Springer Netherlands, 2015.

[31] R. Matheson, “Hybrid drones carry heavier payloads for greater distances,” *MIT News*, Aug. 04, 2017. https://news.mit.edu/2017/hybrid-drones-carry-heavier-payloads-greater-distances-0804 (accessed Apr. 27, 2021).

[32] S. Luo, Q. Sun, W. Wu, M. Sun, Z. Chen, and Y. He, “Accurate flight path tracking control for powered parafoil aerial vehicle using ADRC-based wind feedforward compensation,” *Aerospace Science and Technology*, vol. 84, pp. 904–915, 2019, doi: https://doi.org/10.1016/j.ast.2018.11.022.

[33] J. Tao, Q. Sun, P. Tan, Z. Chen, and Y. He, “Autonomous homing control of a powered parafoil with insufficient altitude,” *ISA Transactions*, vol. 65, pp. 516–524, 2016, doi: https://doi.org/10.1016/j.isatra.2016.08.016.

[34] S. Luo, Q. Sun, W. Wu, M. Sun, Z. Chen, and Y. He, “Accurate flight path tracking control for powered parafoil aerial vehicle using ADRC-based wind feedforward compensation,” *Aerospace Science and Technology*, vol. 84, Jan. 2019, doi: 10.1016/j.ast.2018.11.022.

[35] Y. Li *et al.*, “6-DOF Modeling and 3D Trajectory Tracking Control of a Powered Parafoil System,” *IEEE Access*, vol. 8, 2020, doi: 10.1109/ACCESS.2020.3016669.

[36] "Lauri Kadakas sets new paramotor world record at 1,130 km," *Cross Country*, Mar. 18, 2019. https://xcmag.com/news/paramotor-world-record-lauri-kadakas-cross-country-magazine/#:~:text=Estonian%20paramotor%20pilot%20Lauri%20Kadakas,Australia%20on%209%20March%202019. (accessed Apr. 27, 2021).

[37] D. Gilman, "Unmanned Aerial Vehicles in Humanitarian Response," Aug. 2014. [Online]. Available: www.reliefweb.int.

[38] E. Tatsidou *et al.*, "Reflecting upon the humanitarian use of unmanned aerial vehicles (drones)," *Swiss Medical Weekly*, vol. 149, no. 13–14. EMH Swiss Medical Publishers Ltd., 2019, doi: 10.4414/smw.2019.20065.

[39] D. Jenkins and B. Vasigh, "The economic impact of unmanned aircraft systems integration in the United States," Mar. 2013.

[40] R. Cowlagi, *Integrated Notes AE 3713 Introduction to Aerospace Control Systems AE 4733 Guidance, Navigation, and Communications AE 4723 Aircraft Dynamics and Control*. 2019.

[41] Windtech, "Cargo," 2020. https://www.windtech.es/en/products/cargo/data.html (accessed Dec. 11, 2020).

[42] North Wing, "Pacer 13 GT," 2020. http://www.northwing.com/pacer-wing.aspx (accessed Dec. 12, 2020).

[43] D. Driscoll, B. Ferrarotti, J. Karlin, and R. Patil, "Quad-plane Design for Autonomous Cargo Delivery A Major Qualifying Project Report," 2020.

[44] H. A. Gonzalez, J. Demaio, H. Gonzalez, A. Okhipo, S. Naji, and M. Salamone, "Fixed-Wing Micro Air Vehicle for the 2020 WPI UAV Competition A Major Qualifying Project Report Submitted to the Faculty of the WORCESTER POLYTECHNIC INSTITUTE in Partial Fulfillment of the Requirements for the Degree of Bachelor of Science in Aerospace Engineering Acknowledgements 8," 2001.

[45] Polini, "Thor 250 DS," Accessed: Nov. 14, 2020. [Online]. Available: https://www.polinithor.com/en/polini-thor-250-thor-250-ds-2/.

[46] Elbit Systems, "Hermes™ 450," 2020. https://www.elbitsystems.com.au/uas-hermes-450-tactical-long-endurance-uas/ (accessed Dec. 11, 2020).

[47] Elbit Systems, " Hermes™ 900," 2020. https://elbitsystems.com/products/uas/hermes-900/ (accessed Dec. 11, 2020).

[48] D. Raymer, *Aircraft Design: A Conceptual Approach, Sixth Edition*. Washington, DC: American Institute of Aeronautics and Astronautics, Inc., 2018.

[49] Piper Aircraft, “Arrow,” 2020. https://www.piper.com/model/arrow/ (accessed Dec. 11, 2020).

[50] ULPower Aero Engines, “UL390is,” 2020. https://ulpower.com/en/engines/ul390/ul390is#1-specs (accessed Dec. 11, 2020).

[51] S. Becker and P. Bruce, “Experimental Study of Paraglider Aerodynamics,” 2017.

[52] M. Ghoreyshi, K. Bergeron, A. Jirasek, J. Seidel, A. J. Lofthouse, and R. M. Cummings, “Computational aerodynamic modeling for flight dynamics simulation of ram-air parachutes,” *Aerospace Science and Technology*, vol. 54, pp. 286–301, Jul. 2016, doi: 10.1016/j.ast.2016.04.024.

[53] J. Yao, B. Chen, Y. Yan, W. Feng, C. Huang, and L. Yan, “Layout designment of an in-flight-deployable and fast self-stable small-UAV,” Oct. 2019, doi: 10.1109/ICUS48101.2019.8995992.

[54] M. R. Napolitano, *Aircraft Dynamics: From Modeling to Simulation*. 2011.

[55] D. Olinger, *AE4770 Aircraft Design Lecture 24 Notes*. 2020.

7 Appendix

7.1 Link to Github

https://drive.google.com/drive/folders/1JZgt9YgWaX9PvUQVXqZbWU8NHwc6o4cn?usp=sharing

7.2 Engine Specification Sheet

Engine Title	Thrust Max(N)	Propellar Size(m)	Efficiency	Engine Mass(kg)	Fuel Density	Fuel Type	Fuel Mass	Fuel Consumption	Power(HP)	RPM
Polini Thor 130 evo engine				13.8	800	Lead-Free Petrol with 2%Synth Oil			21.5	8800
Polini Thor 250 engine	1029	1.5		18	810	E5 petrol or LL AV GAS-al with 2,5% synthetic oil 100%		2.9 L/hr at 30kg thrust	36	8000
Vittorazi Moster 185 Plus MY	750	1.3		14.2	715-780	Unleaded gasoline - Synthetic oil 2.5%		4 L/hr at 30kg thrust	25	7800
Vittorazi Atom 80 MY20	550	1.3		10.5		Unleaded gasoline - Synthetic oil 1.5%		2.25 L/hr at 30kg thrust	16	9500
Continental C-90				97.61					90	2475
AMW 636				52.21					90	7000
Cam Turbo 90				65.376					90	5300
Norton Aerotor				59.02					90	7500
ROTAX 912 iS SPORT L			75%	73.5		min. MON 85 RON 95* min. AKI 91*		15 L/hr	100	5800
ROTAX 915 iS A						min. MON 85 RON 95* min. AKI 91*			141	5800
EOS 100 ICI standard	590	1.3		9.7	703	unleaded 98 octane-2%oilmix		3 L/hr avg	20	9200
EOS 100 ICI RV5	610	1.3		9.9	703	unleaded 98 octane-2%oilmix		3.25 L/hr avg	21	9500
EOS 150 ICI RV3	700	1.3		11.5	703	unleaded 98 octane-2%oilmix		3.65 L/hr avg	25	9000
Victor 2 Super	1962			52	715-780			15 L/hr at 5400 rpm	100	6200
49T8				39.498		Gasoline			27	

7.3 Gains Matrices: Fixed Wing (Longitudinal)

The LQR solves the algebraic Riccati equation for S. The algebraic Riccati equation is as follows:

$$A^T S + SA - SBR^{-1}B^T S + Q = 0$$

given Q and R matrices decided by the team, and A and B matrices defined by the system dynamics.

The gain values K are given by:

$$K = R^{-1}B^{T}S$$

The K values for various scenarios are as follows:

Climb1				
0.079888	-0.0748	-0.3912	-2.72414	-3.16E-06
Cruise1				
0.0608258	0.015065	-0.03547	-0.8151	-0.00707
Helix				
0.0371565	0.02387	-0.05819	-1.49335	7.07E-06
Climb2				
0.1938116	-0.39108	-3.92243	-7.08366	1.83E-05
Cruise2				
0.0418296	-0.0078	-0.23201	-1.29513	1.41E-05
Descent				
0.0578344	-0.04661	-0.42945	-2.03869	1.00E-05

7.4 Gains Matrices: Fixed Wing (Lateral)

Climb1					
0.020714	0.136737	-0.0599	0.514407	1.076046	0.000301
-0.00433	0.013423	-0.13423	-0.00947	-0.53272	-1.09E-05

Cruise1					
0.016697	0.171639	-0.05161	0.310566	0.681115	3.15E-06
-0.0072	0.033808	-0.31365	0.012493	-0.73248	-2.22E-07
Helix					
0.015128	0.188571	-0.02493	0.505515	0.73292	9.52E-06
-0.0046	0.020931	-0.21919	0.000615	-0.52427	-3.77E-07
Climb2					
0.015651	0.100601	-0.04479	0.482245	1.13494	0.000301
-0.003	0.010269	-0.10147	-0.00625	-0.51287	-5.13E-06
Cruise2					
0.011578	0.168213	-0.01854	0.482655	0.675263	3.02E-05
-0.0039	0.022334	-0.20995	0.013984	-0.53092	-6.38E-08
Descent					
0.036459	0.232247	-0.16025	0.892247	1.774095	3.00E-05
-0.00426	0.012063	-0.16155	-0.01443	-0.48245	-1.04E-06

7.5 Simulink Small Disturbance Response: Fixed Wing – Climb 1 (Longitudinal)

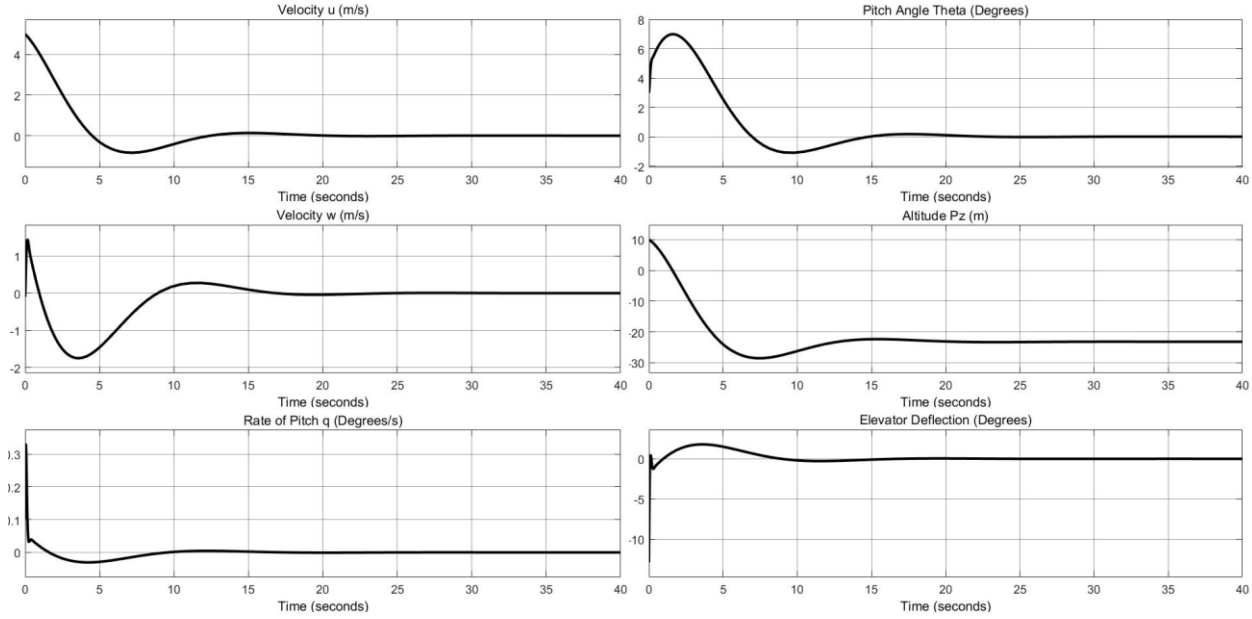

7.6 Simulink Small Disturbance Response: Fixed Wing – Climb 1 (Lateral)

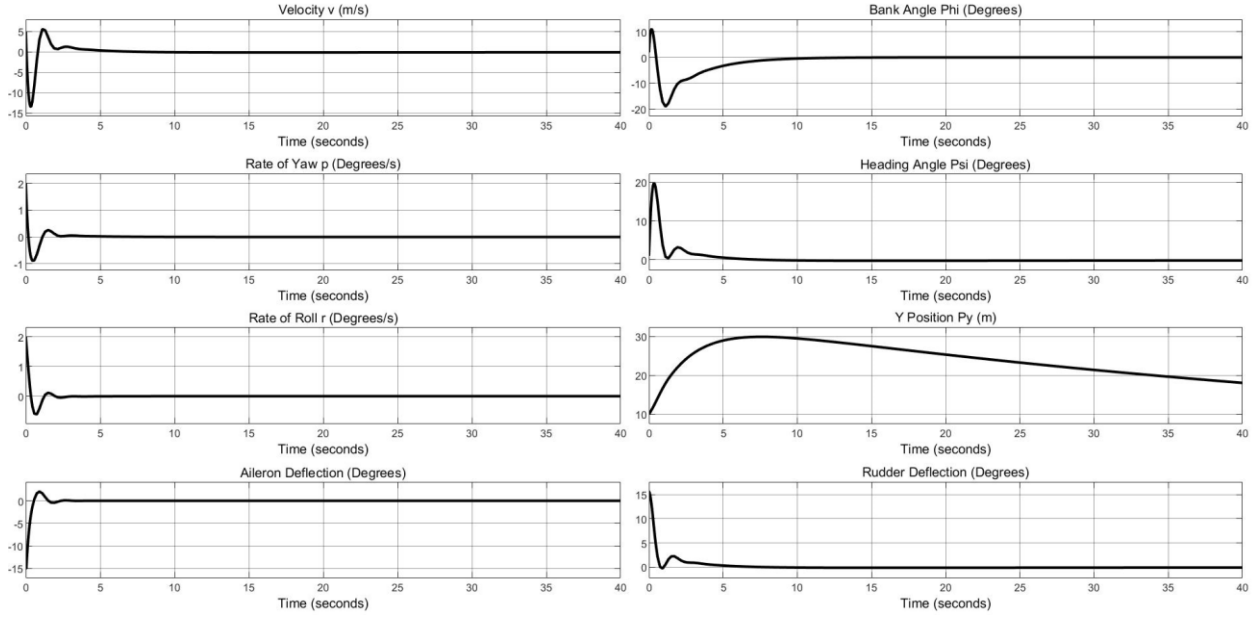

7.7 Simulink Small Disturbance Response: Fixed Wing – Cruise 1 (Longitudinal)

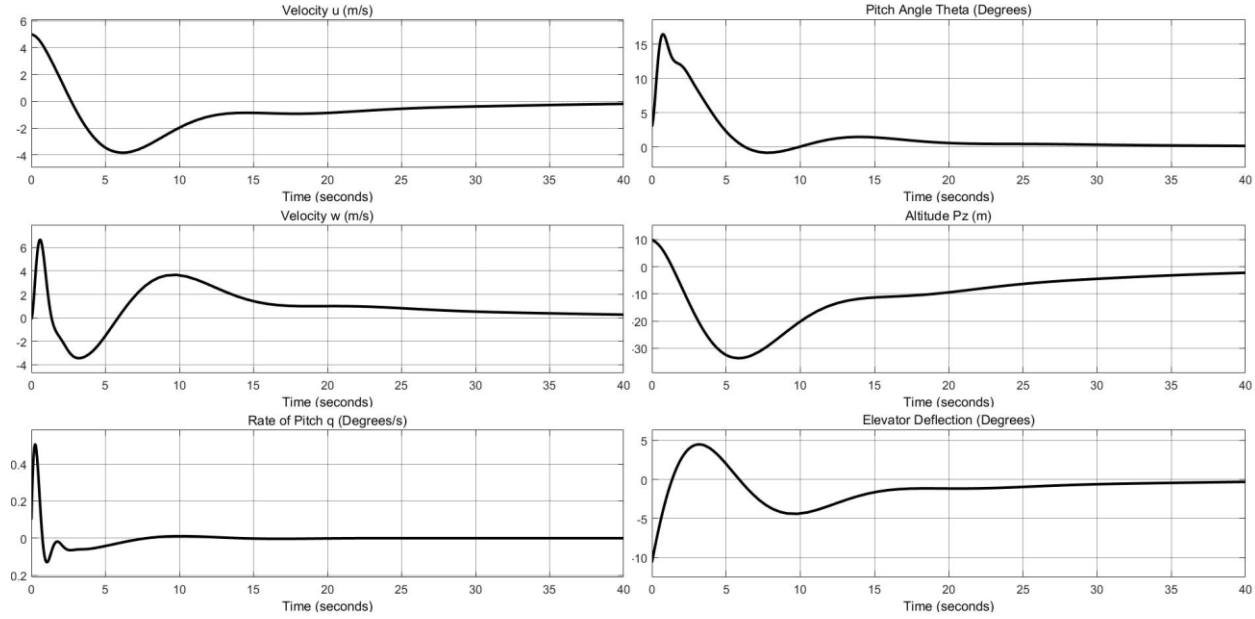

7.8 Simulink Small Disturbance Response: Fixed Wing – Cruise 1 (Lateral)

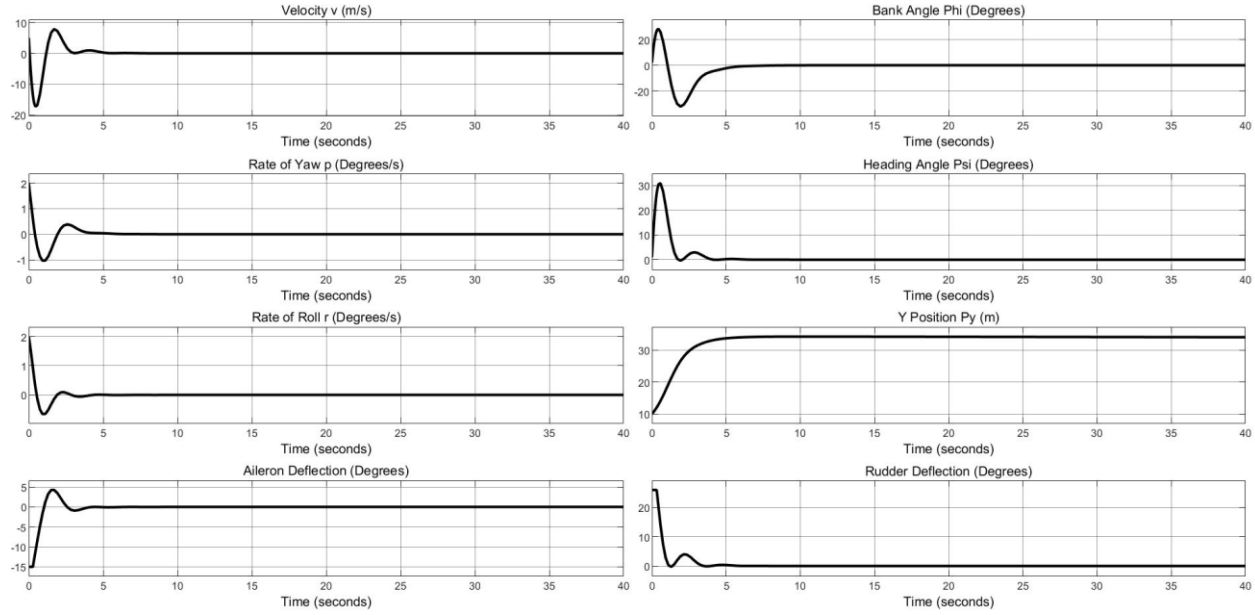

7.9 Simulink Small Disturbance Response: Fixed Wing – Helix (Longitudinal)

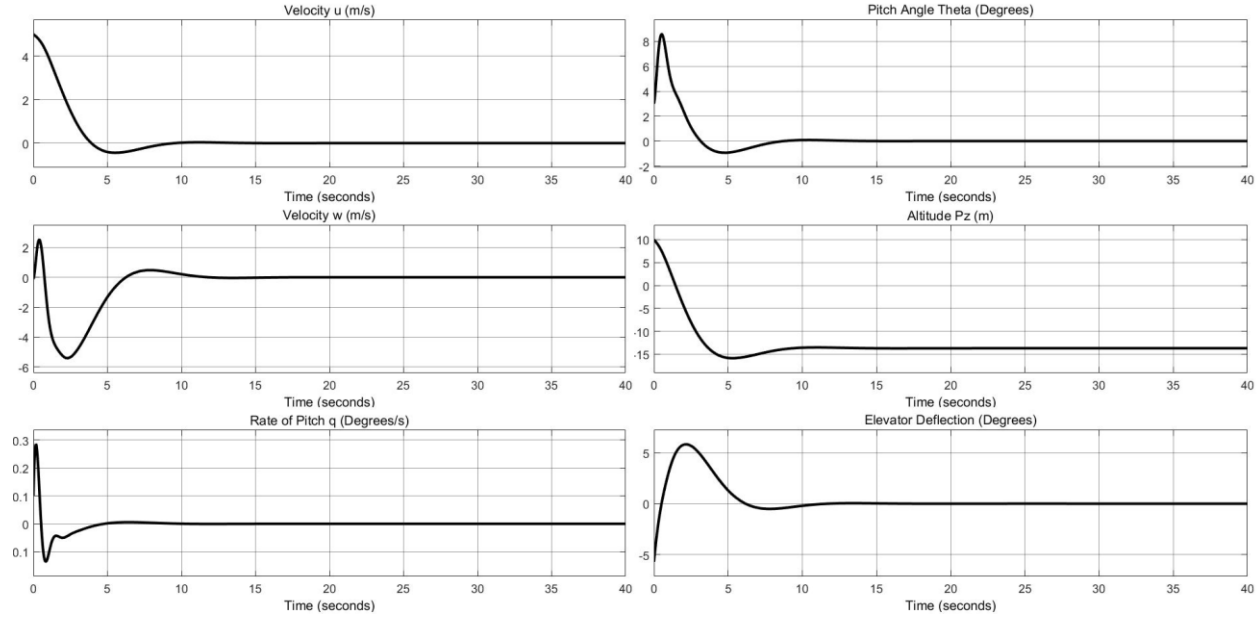

7.10 Simulink Small Disturbance Response: Fixed Wing – Helix (Lateral)

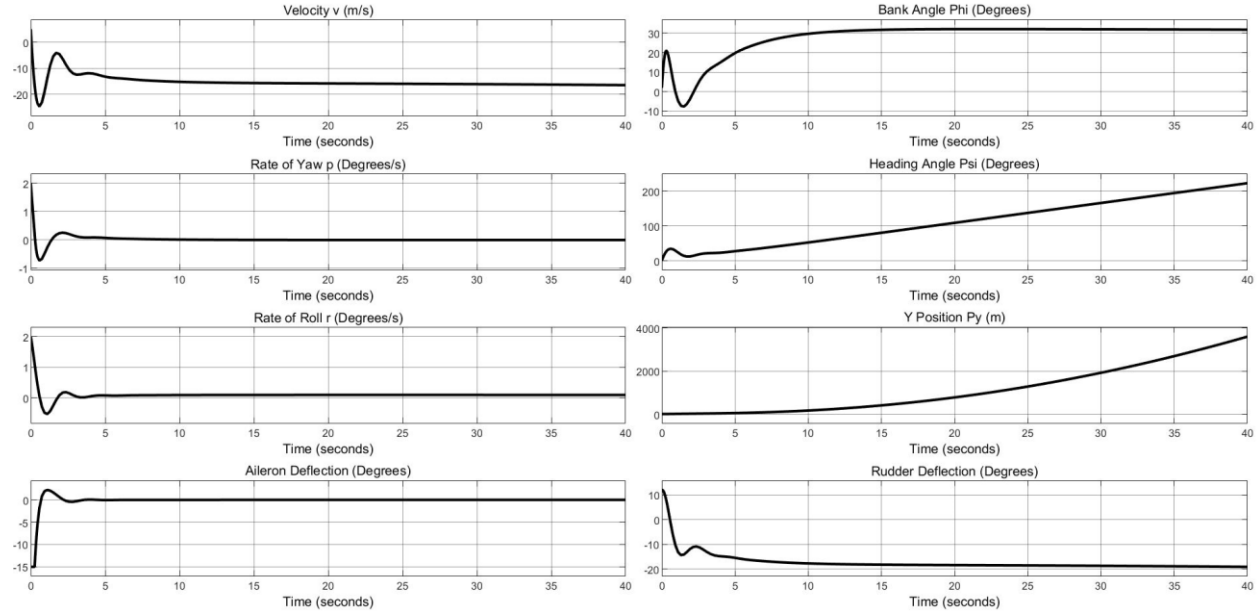

7.11 Simulink Small Disturbance Response: Fixed Wing – Climb 2 (Longitudinal)

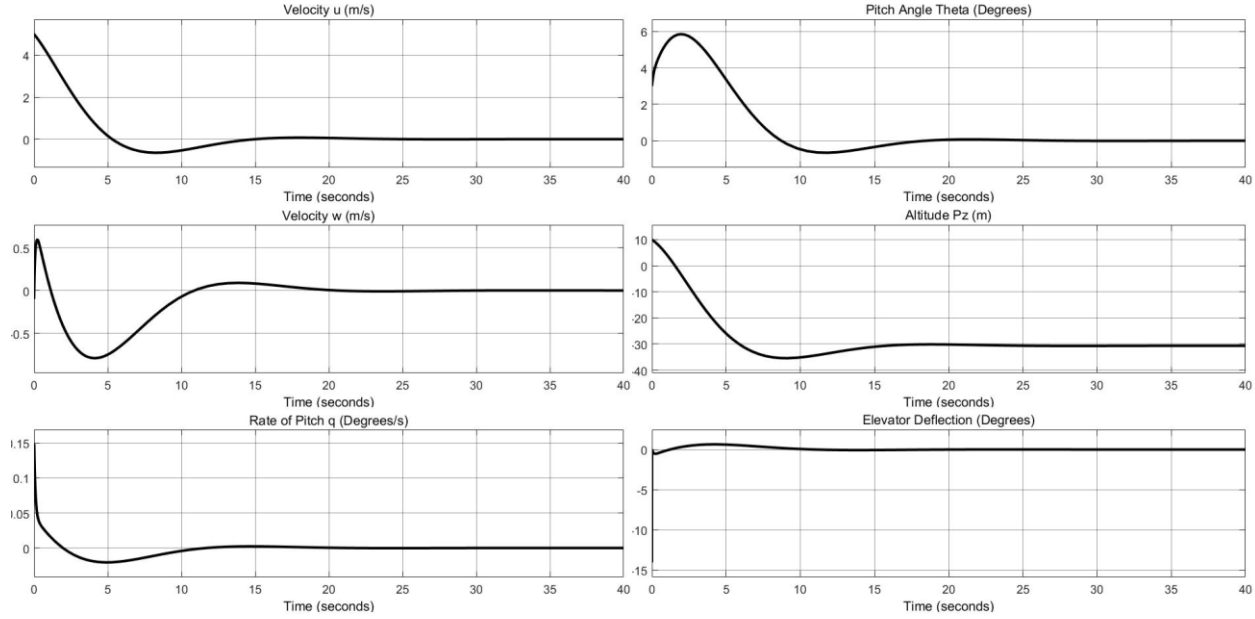

7.12 Simulink Small Disturbance Response: Fixed Wing – Climb 2 (Lateral)

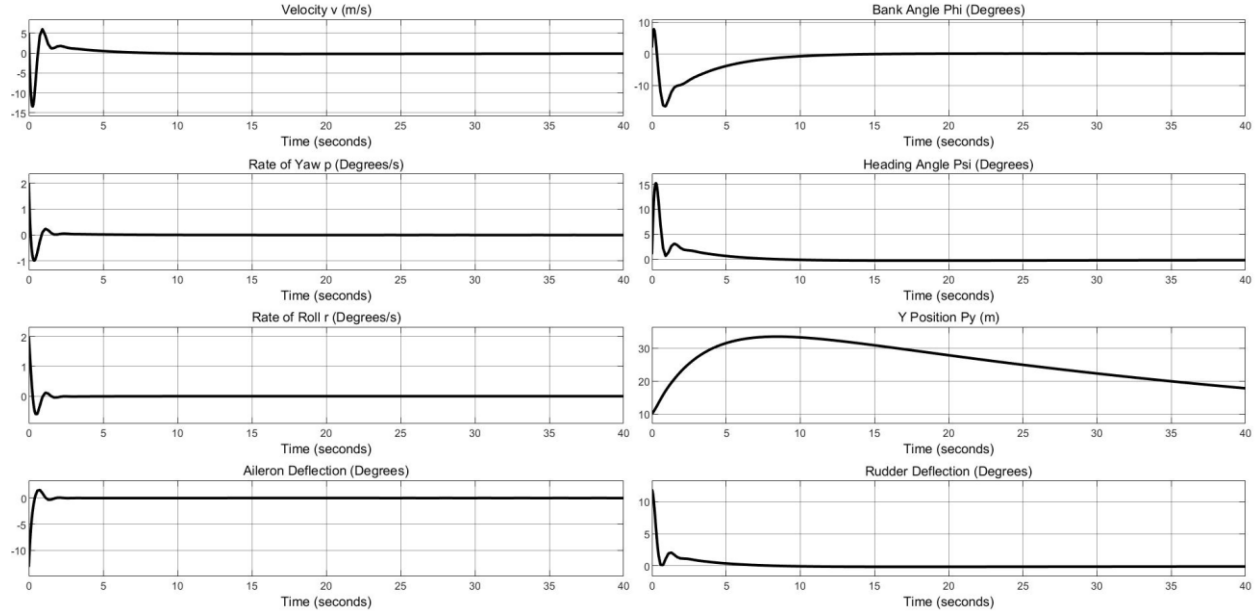

7.13 Simulink Small Disturbance Response: Fixed Wing – Cruise 2 (Longitudinal)

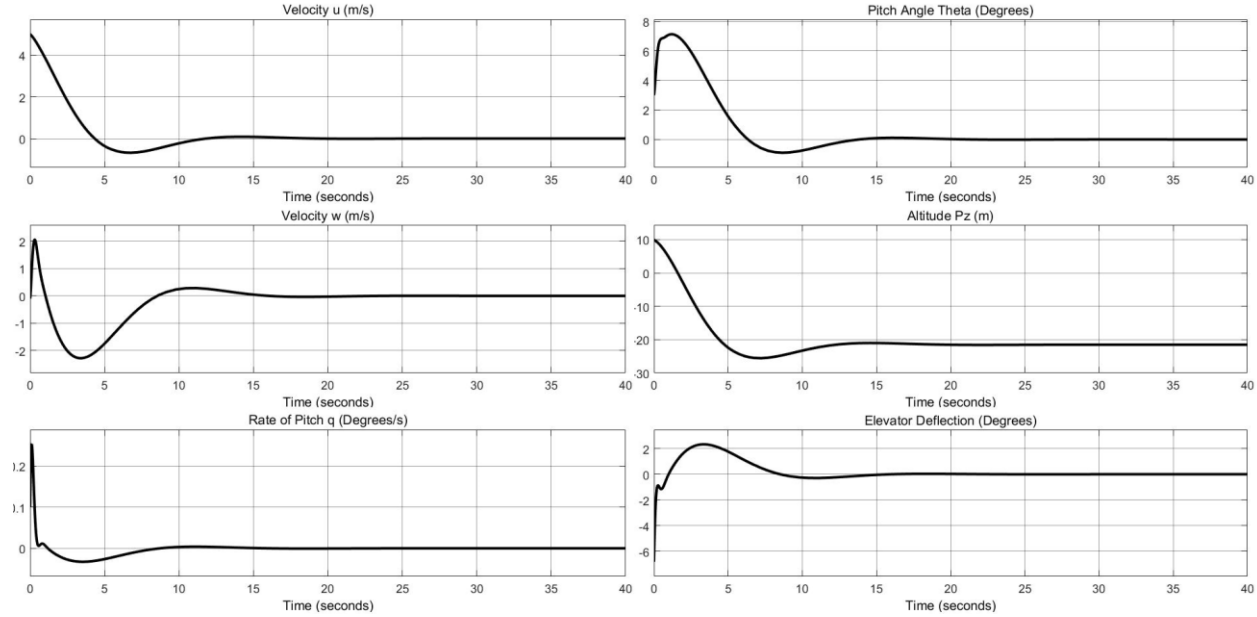

7.14 Simulink Small Disturbance Response: Fixed Wing – Cruise 2 (Lateral)

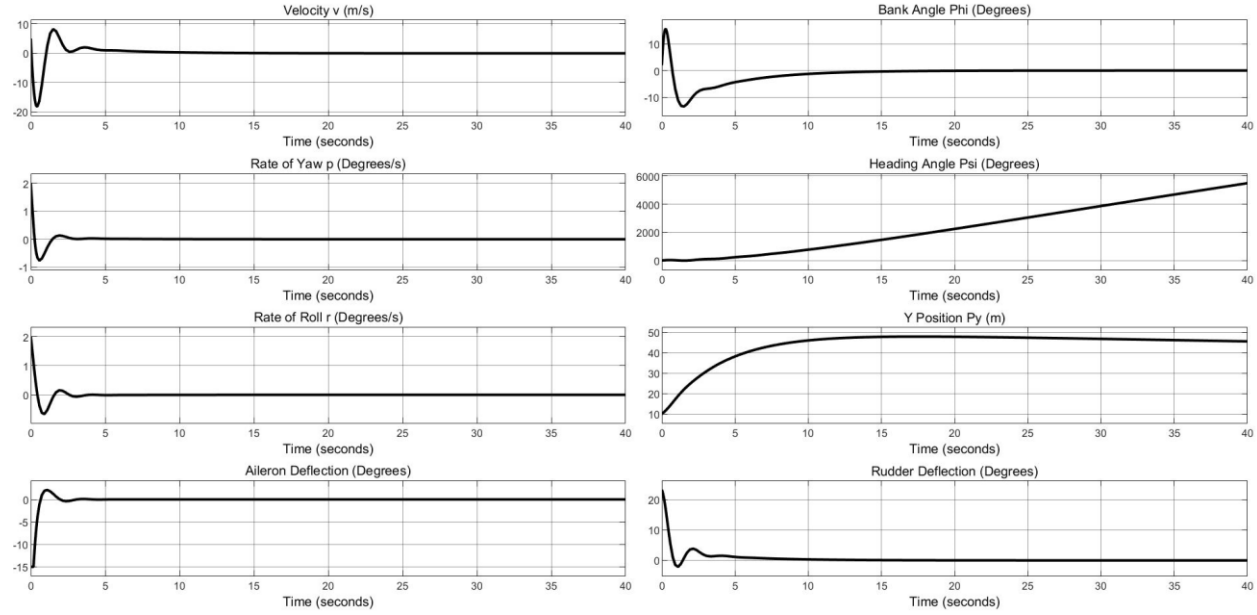

7.15 Simulink Small Disturbance Response: Fixed Wing – Descent (Longitudinal)

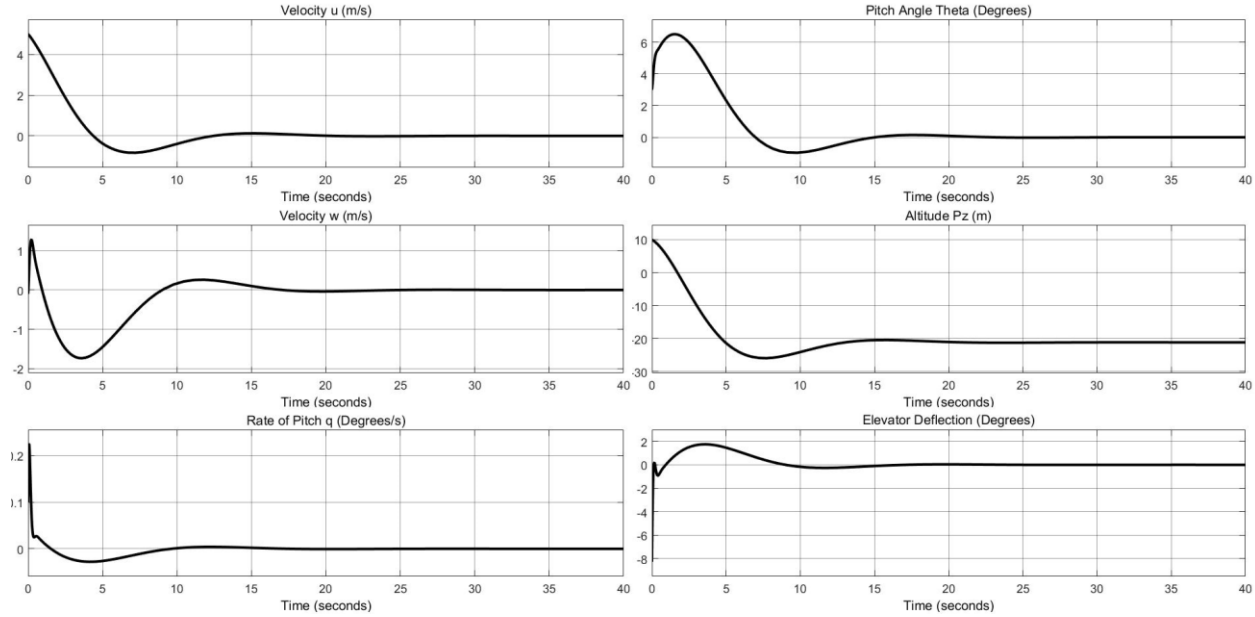

7.16 Simulink Small Disturbance Response: Fixed Wing – Descent (Lateral)

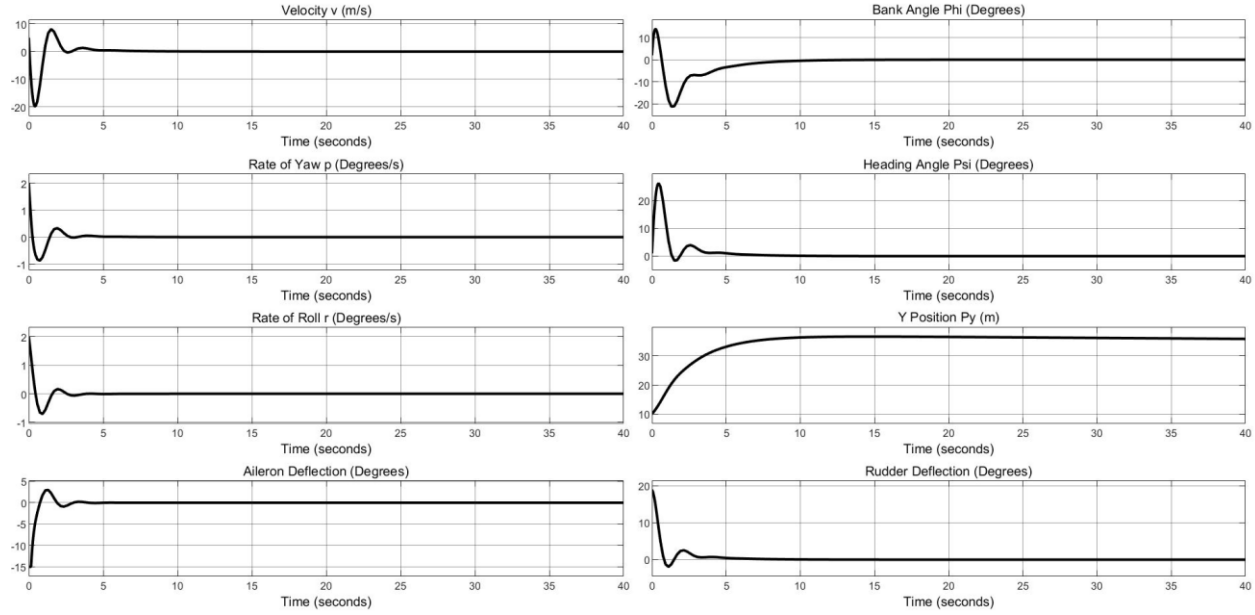

7.17 Wind Disturbance Matlab Model: Fixed Wing

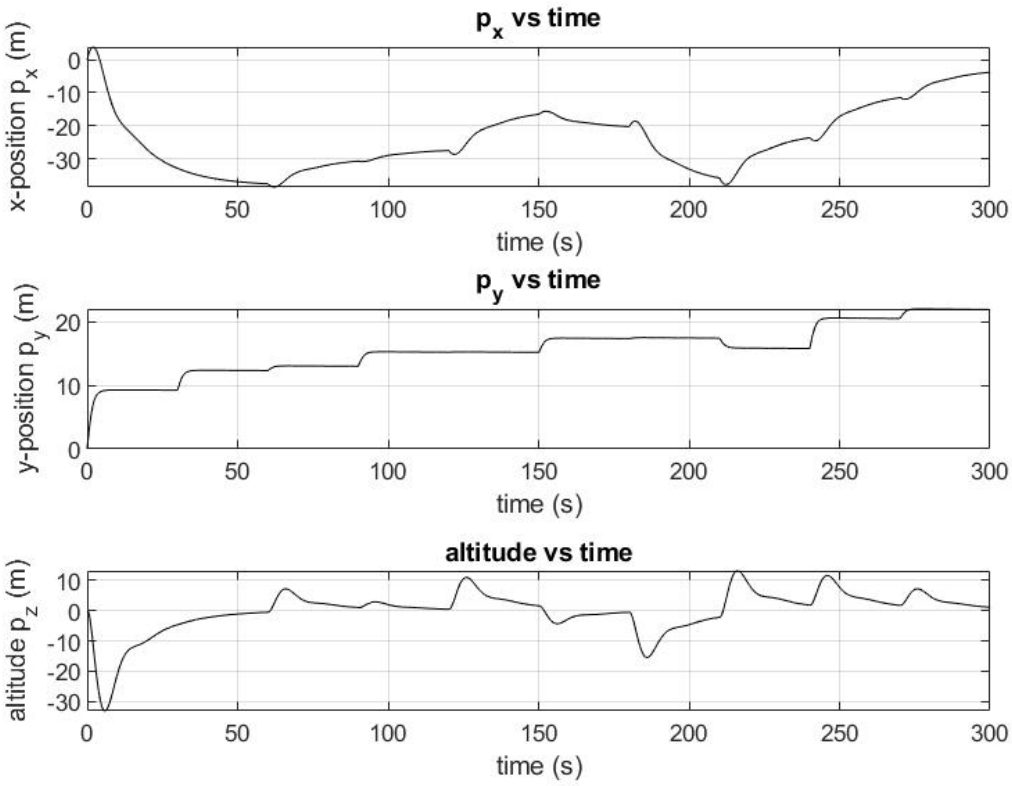

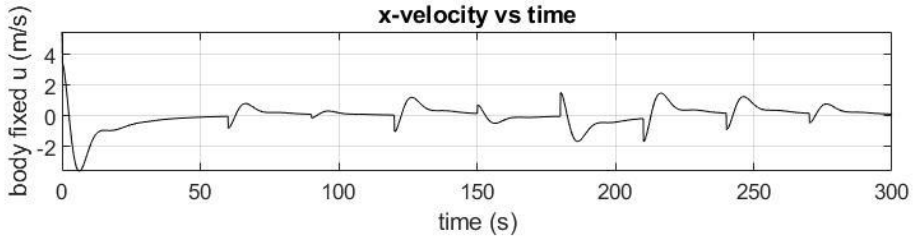
x-velocity vs time
body fixed u (m/s)
time (s)

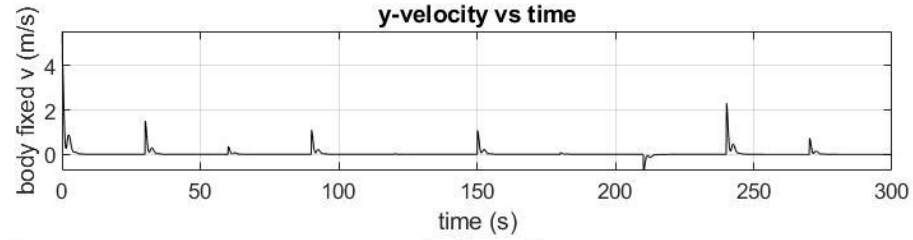
y-velocity vs time
body fixed v (m/s)
time (s)

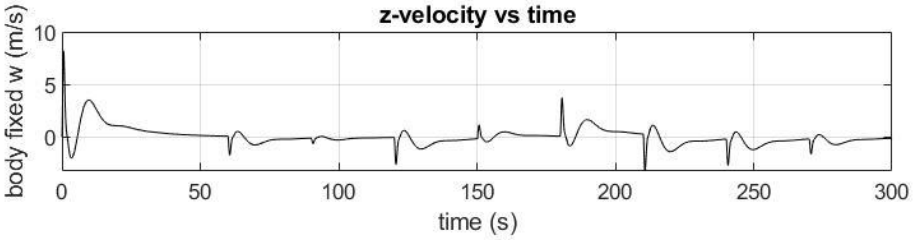
z-velocity vs time
body fixed w (m/s)
time (s)

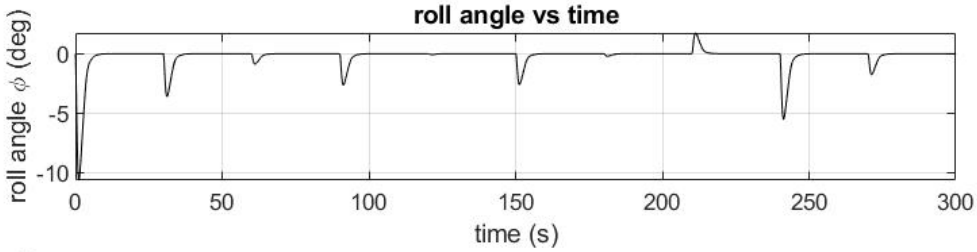
roll angle vs time
roll angle ϕ (deg)
time (s)

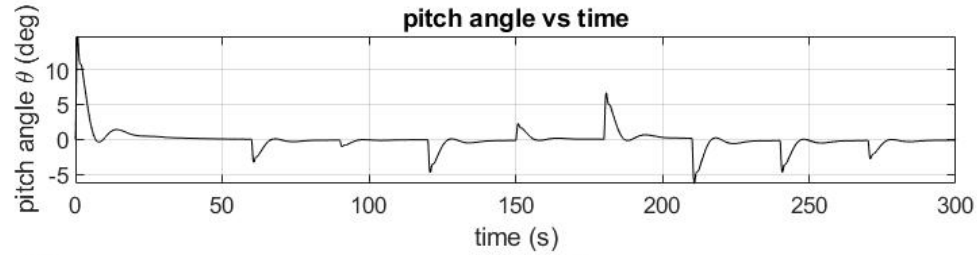
pitch angle vs time
pitch angle θ (deg)
time (s)

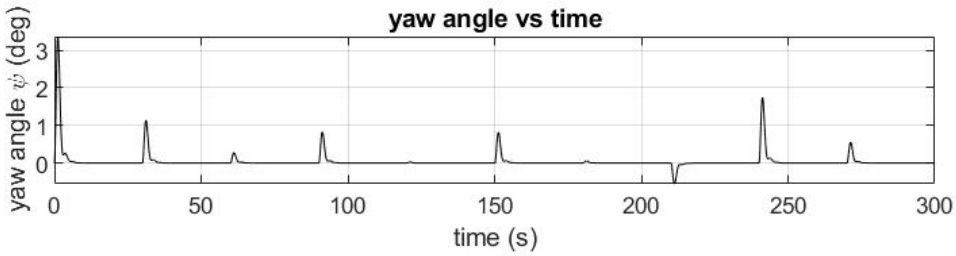
yaw angle vs time
yaw angle ψ (deg)
time (s)

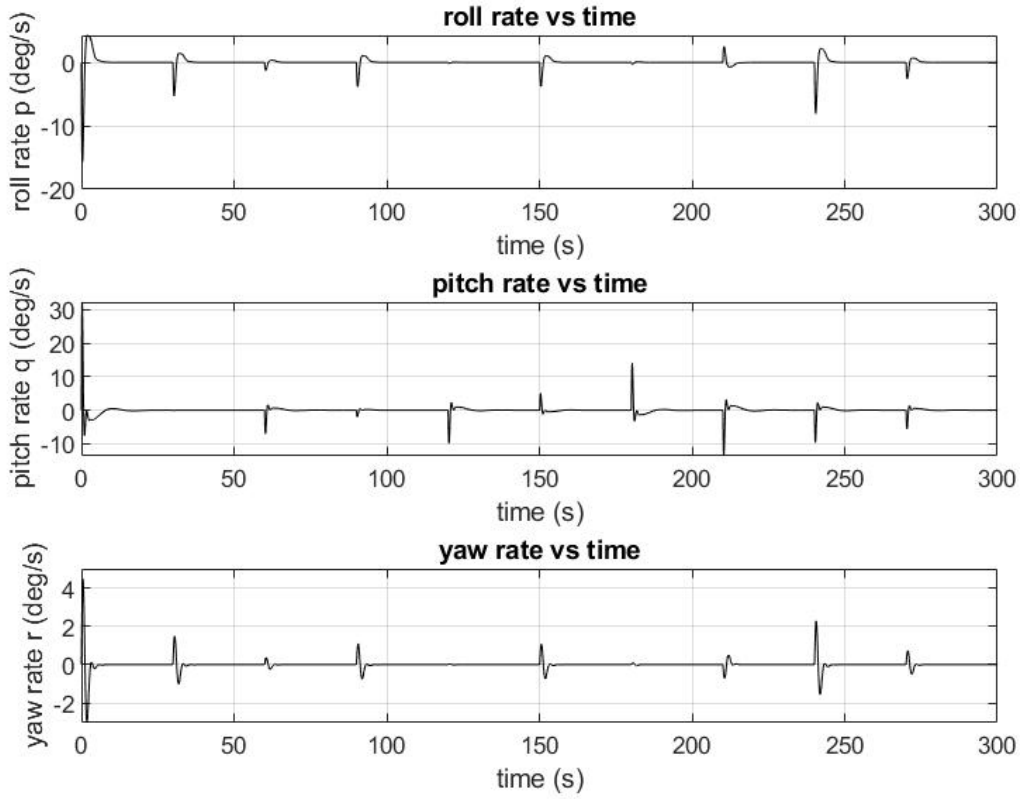

7.18 Gains Matrices: Parawing (Longitudinal)

Climb1				
0.130425	-0.03927	-0.40998	-1.99723	-3.16E-06
Cruise1				
0.0685019	-0.00777	-0.25964	-0.83308	-0.01
Helix				
0.0637757	-0.00405	-0.3438	-1.30572	-7.07E-06
Climb2				
0.2032865	-0.23648	-3.40521	-4.93378	1.83E-05

Cruise2				
0.0588032	-0.01096	-0.336	-1.24039	1.41E-05
Descent				
0.0897067	-0.02548	-0.46148	-1.63175	1.00E-05

7.19 Simulink Small Disturbance Response: Parawing – Climb 1 (Longitudinal)

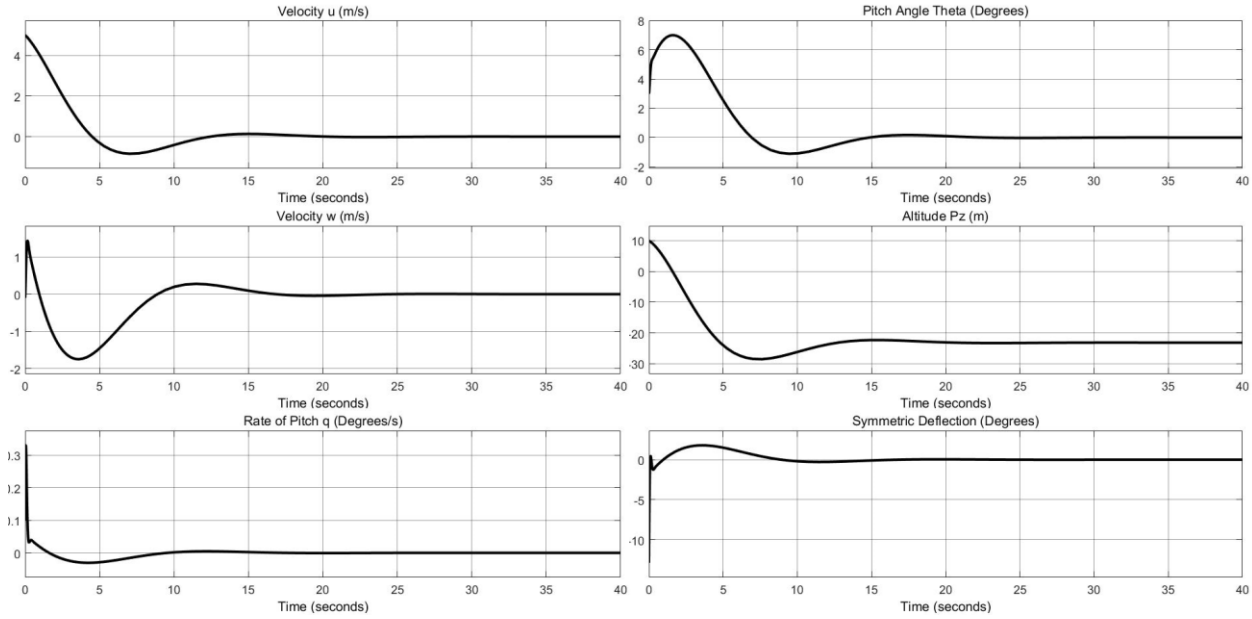

7.20 Simulink Small Disturbance Response: Parawing – Cruise 1 (Longitudinal)

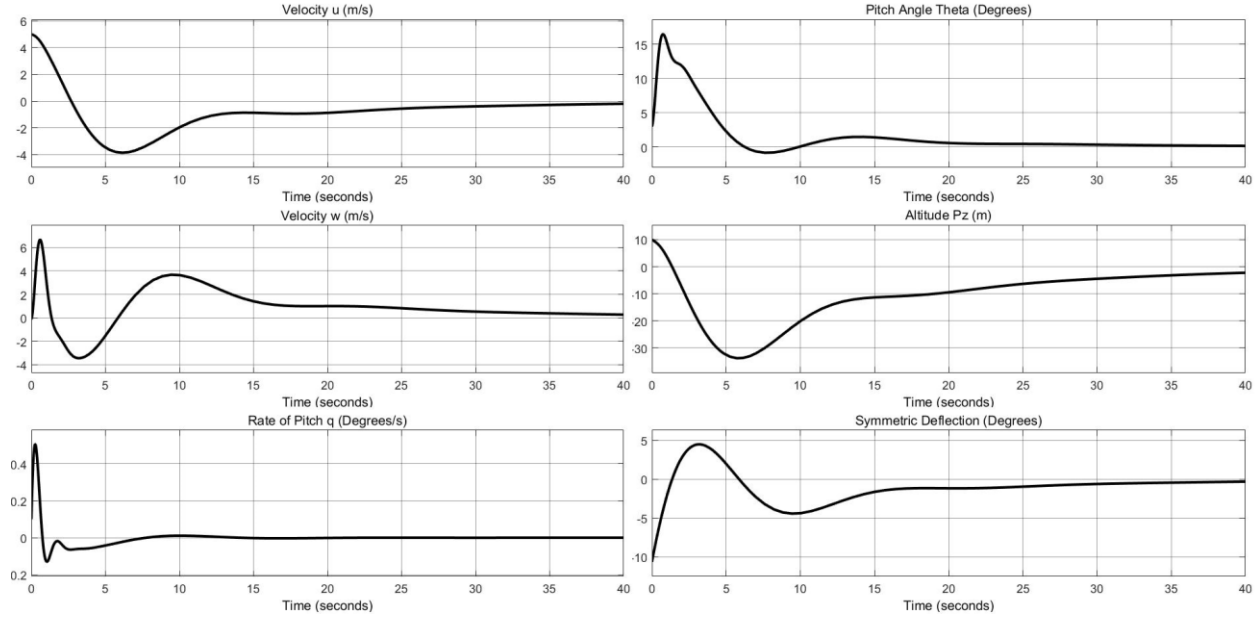

7.21 Simulink Small Disturbance Response: Parawing – Helix (Longitudinal)

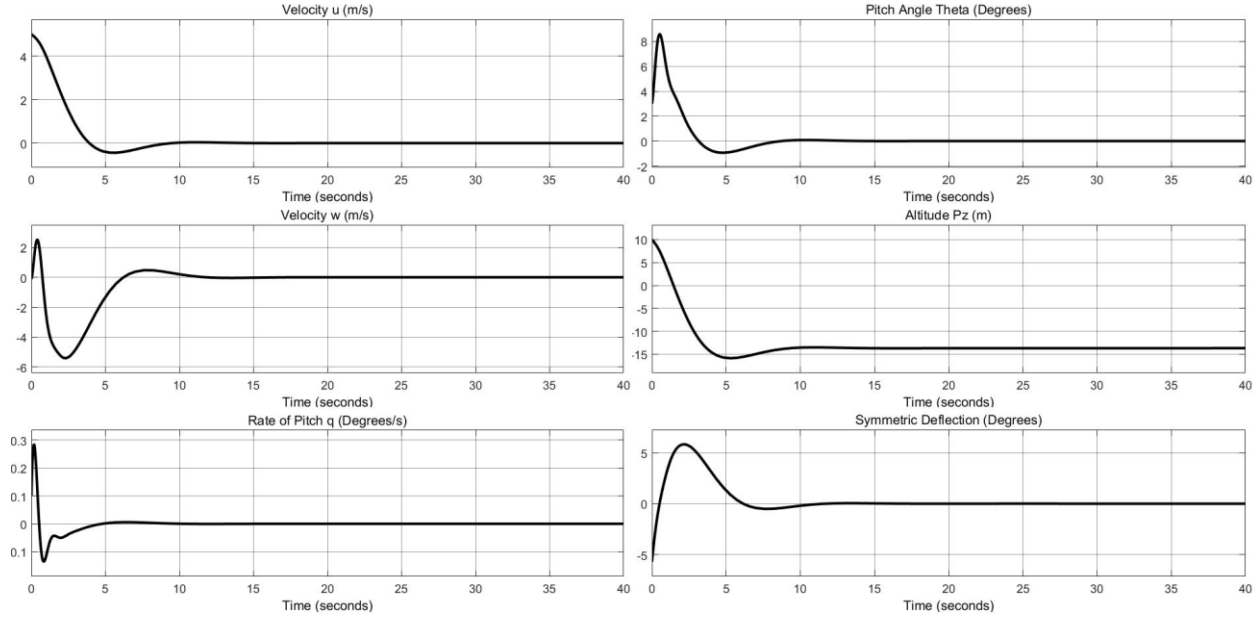

7.22 Simulink Small Disturbance Response: Parawing – Climb 2 (Longitudinal)

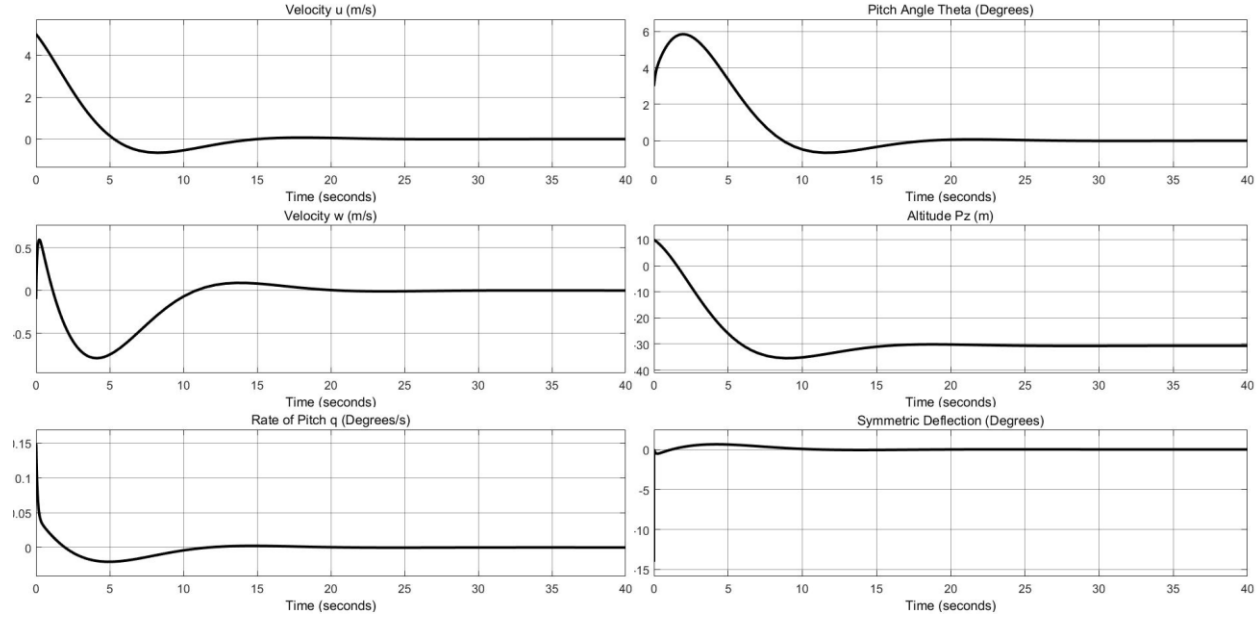

7.23 Simulink Small Disturbance Response: Parawing – Cruise 2 (Longitudinal)

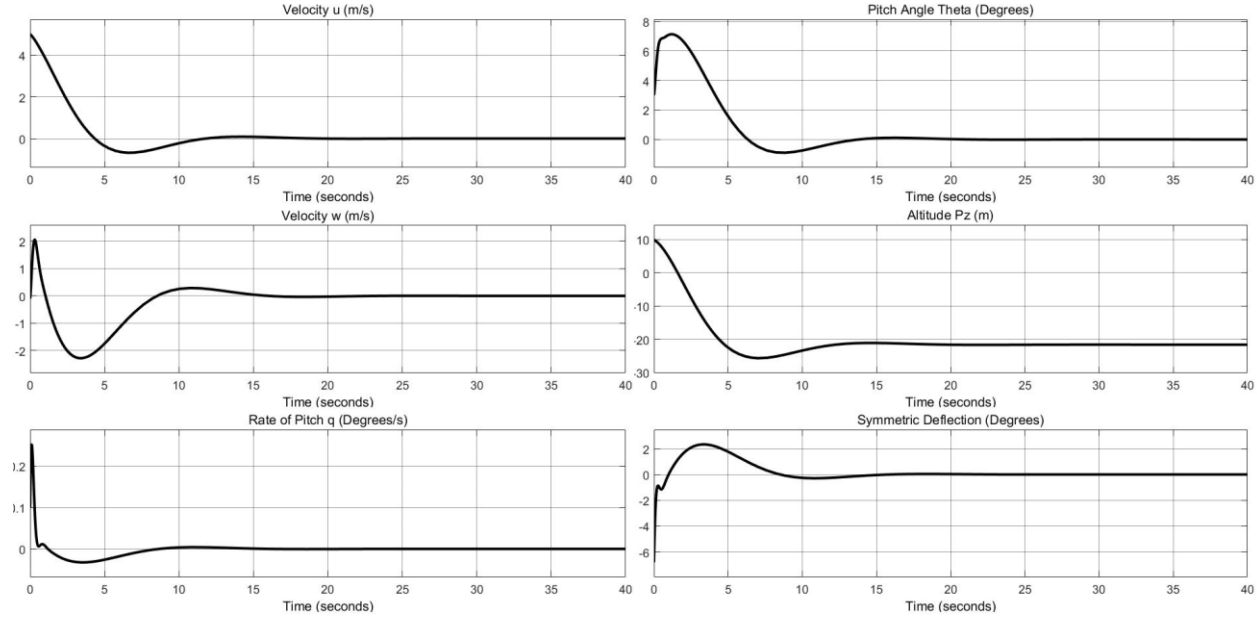

7.24 Simulink Small Disturbance Response: Parawing – Descent (Longitudinal)